ATOMISTIC MODELING OF DISLOCATION MOTION AT EXPERIMENTAL TIME-SCALES

A Dissertation

Presented to the Faculty of the Graduate School

of Cornell University

in Partial Fulfillment of the Requirements for the Degree of

Doctor of Philosophy

by

Sepehr Saroukhani

January 2017

ATOMISTIC MODELING OF DISLOCATION MOTION AT EXPERIMENTAL TIME-SCALES

Sepehr Saroukhani, Ph.D.

Cornell University 2017

An accurate prediction of the rate of dislocation motion is key to the fidelity of multi-scale plasticity models of metals and alloys. In this dissertation, atomistic simulations and rate theories based on statistical mechanics are used to accurately predict the rate of three main dislocation motion mechanisms:

1. Dislocation motion across precipitates
2. Dislocation motion through a field of obstacles
3. Dislocation motion via kink-pair nucleation

For these mechanisms, the accuracy of both conventional and modern rate theories is examined by comparing their predictions to benchmarks obtained from MD simulations.

Different variants of the Harmonic Transition State Theory, as the most common rate theory in the literature, are found to provide grossly inaccurate predictions for all three problems. It is shown that the inaccuracy of these approaches stems from their assumptions about the entropy barrier. The original version of HTST estimates the entropy barrier by the harmonic vibrational entropy, which is found to be inaccurate for all three problems due to thermal softening. Other versions of HTST based on simple estimates of the attempt frequency consider smaller values for the vibrational entropy, and hence provide even more inaccurate predictions. Furthermore, all variants of HTST neglect the configurational entropy, which turns out to be significant for the kink-pair nucleation problem.

The utility of the Finite Temperature string method for computing a reaction coordinate and a free energy profile was examined for the three problems. The method provides an accurate reaction channel for dislocation-obstacle interactions but fails to provide a reasonable free energy profile. The reasons are investigated and discussed in the first paper presented in this dissertation. The original version of the method fails to provide a reaction channel for the kink-pair nucleation problem because it has not been designed for problems with multiple reaction channels. To address this issue, a modification to the approach based on physical intuitions about the problem is proposed and is shown to be effective.

Different variants of the Transition Interface Sampling approach, as a modern rate theory, are found to be capable of accurately predicting the rate for all three problems. TIS and its Path Swapping version are found to be effective for dislocation-precipitate interactions. The method is also accurate in the jerky motion regime of dislocation motion through a field of solutes. For the smooth motion regime, however, the Partial Path version of TIS — designed for diffusive barriers — had to be used. In order to provide accurate predictions for the kink-pair nucleation problem, TIS had to be modified based on physical intuitions about the problem because the method has not been designed for problems with multiple reaction channels such as the glide of screw dislocations in BCC transition metals.

The performance of the Meyer-Neldel (MN) rule, as the most common entropy estimation approach in material mechanics, is examined for the three problems. It is shown that the method accurately predicts the entropy barrier for dislocation-precipitate interactions but fails to fully explain the entropy barrier for the other two problems. The assumptions and theoretical justification of

the method for dislocation processes, which are often neglected in the literature, are revisited and simple alternative models are proposed.

BIOGRAPHICAL SKETCH

Sepehr Saroukhani grew up in Tehran, Iran. He finished high school in May 2004, and started his undergraduate studies in Civil and Structural Engineering at the Azad University of Central Tehran in September, the same year. He received his bachelor's degree in May 2008, and began his graduate studies in the same field at Chalmers University of Technology in Sweden. His master's thesis was a joint project between Chalmers University and TU Delft, in the Netherlands, and he spent time and published in both institutes. After graduating in July 2010, he joined the Ph.D. program in the School of Civil and Environmental Engineering at Cornell University. In January 2013, he joined Professor Warner's research group to complete his Ph.D. under his supervision. He then graduated with his second master's degree in September 2014 and later defended his Ph.D. thesis in December 2016. Back in high school, Sepehr was an award winning athlete in soccer, wrestling and table tennis and continues to enjoy competing to date. In his spare time, he enjoys reading about history, markets, professional athletes and competitors and is a fan of F.C. Barcelona.

To my brother, Armin, my first aunt, Khaleh Azi, and my uncle, Amoo Joon, who passed away in a car crash a few weeks before my A exam and did not live to celebrate this moment with me.

ACKNOWLEDGEMENTS

I would like to thank Dr. Derek Warner for giving me the opportunity to work with him, for being encouraging when I was discouraged, for being patient with my impatience, and for giving me vision when I was blind about the big picture. Derek's optimism and positive energy are unparalleled and a powerful driving force for research. His empowering management style along with his hands-on advising style foster a positive work environment in the group and nurtured my interest in research. Overall, I learned from Derek both academically and personally and thank him for giving me that opportunity.

I would like to thank those who supported my graduate studies at Cornell. In particular, I am indebted to Dr. Bernard Ross for supporting the last year of my research. I am also very grateful to Dr. Maria Terrell for giving me the opportunity to TA in the Department of Mathematics. Last but not least, I had the opportunity to work as a lecturer in the Department of Civil and Environmental Engineering for which I thank Ms. Nadine Porter.

I was very fortunate to have Dr. David Bindel and Dr. Richard Hennig in my graduate committee. Dr. Bindel's comments during my A exam encouraged me to study the statistical errors of Transition Interface Sampling and include them in my third paper, presented in the last chapter. He is also one of the best teachers I had at Cornell in his unparalleled parallel computing course. Dr. Hennig's comments spurred me to examine the reasons behind the inaccuracy of the harmonic approximation and later led to the deep discussions on this topic throughout this dissertation.

My parents put up with my absence for more than six years. I was not there in some of the hardest years of their lives. They went through adversities while I was completing my education. I am out of words to thank them and will always

be indebted to them. I was an athlete in high school and an unruly student, in a country where playing sports did not properly pay the bills back then. My mom was instrumental in my transformation to a college kid who would go on to win national awards for his academic success. My daily conversations with my dad about world politics, history and philosophy expanded my horizons and planted the seed of immigrating to the U.S. in my long term goals.

Speaking of character building, I was fortunate to have three of my best friends, Sina Shahbazmohammadi, Aidin Gharehdaghi and Nima Samadzadegan. It is rare to have a group of friends that gathers people with natural leadership, intellect, work ethics, resilience and athletic competitiveness all at once. Sina and I grew up together, with about 20 years of friendship. He is a natural born academic who started teaching at 15 and was always ahead of his time. No wonder that he is an assistant professor at the University of Connecticut now. Aidin is a charismatic leader who taught us unconditional support for friends and family. He was also a national team level soccer player who turned out to become a great researcher back home. Nima embodies work ethics and resilience, whom everyone predicted to become a big name in his field. He is now one of the most venerated structural engineers back home. I would like to think that their friendship left a fraction of their qualities in my character as we were growing up together.

My grandparents, Maman and Baba Khalilkhani, and my senior aunt, Khaleh Eli, comforted my mom when she missed me all these years, when she was going through health problems, and when she tragically lost her sister. Baba Khalilkhani is the greatest man I have ever seen and I aspire to live my life like him. Maman Khalilkhani and Eli were among the few people who got me as a weird, yet gifted, kid. Their voice on the phone always motivated me

during these years.

I am eternally indebted to the love of my life, Mahsa, for her constant care and support. I cannot thank her enough for her frequent visits to Ithaca. I still vividly remember her surprise visit on a day during the first year after she realized I was very down. She has turned many such days around and created way more happy days since. Mahsa and I met eight years ago when I was a 22 year old whose ambitions were all he had. Mahsa is still that beautiful girl with silky black hair and endearing eyes who believes in me and my aspirations. Her smile reminded me of my vision every single day and I am out of words to appreciate that.

I would like to thank my uncle, Daee Joon, and his wife, Mahsa Khanoom, for always being there for me during these years in the U.S. Mahsa always made me feel at home during my numerous visits and cooked particular Persian dishes a few times just because I was craving them. I still vividly remember Daee Joon's present for my first birthday in the U.S. It was a few days after I moved to the U.S.; I was alone in my room and his present reminded me that there was someone in this country that knew about my birthday. There is no words that can do justice to how grateful I am to everything he has done since I moved to the U.S.

The type of kid that I was, I needed a wise big sister to look after me when our parents were at work. Sepideh, a.k.a. Sipid Jan, was always there for me. Sepideh and Pooya, my brother-in-law, had me over quite a few times and she cooked my favorite Persian dishes the way our mom did as well as her own originals. You will know what that means if you cannot visit home. Traveling all the way from Texas to Ithaca during the graduation week was another great memory that Sepideh and Pooya created for me and I will always be grateful

for that.

I would like to thank my best friend, Haj Nezam, and his wonderful wife, Bahar, for visiting me and bringing me authentic Persian cuisine every year during my graduate studies. Nezam, a.k.a. Gatte Sibil, and Bahar created some of the best days that I have had since leaving home and I would not have had a chance to enjoy revisiting some of my best memories from old times without Nezam visiting me every year.

Last but not least, a group of smart, fun and supportive friends helped me get through graduate school life in a small, remote and cold city. Alin Radu is a close friend and was the best office mate that I could ask for. He encouraged me to try Sushi for the first time, and have loved it since. Sina Lashgari is a friend that I can have a conversation with forever. Yazdan and Hamideh's stay at Cornell was short but they had a positive touch on everyone in the community around me. Agha Beheshtian, Mahyar, Agha Rouhani, Hadi, Navid, Vahnood, Meraj, Negin, Nima (Peyman), Agha Aghasi, Ehsan, Rad, Naser, Mehrzad and many good friends that I might have forgotten to name are on top of the list of things that will remain part of my life after my experience in Ithaca.

TABLE OF CONTENTS

Biographical Sketch . . . iii
Dedication . . . iv
Acknowledgements . . . v
Table of Contents . . . ix

1 Introduction **1**

2 Harnessing atomistic simulations to predict the rate at which dislocations overcome obstacles **5**
2.1 Abstract . . . 5
2.2 Introduction . . . 6
2.3 Methods . . . 9
2.3.1 Transition State Theory . . . 9
2.3.2 Finite Temperature String Method . . . 13
2.3.3 Transition Interface Sampling . . . 14
2.4 Simulation Details . . . 17
2.5 Results and discussion . . . 20
2.5.1 Comparison of the methods . . . 20
2.5.2 Temperature Effect . . . 23
2.5.3 Load Effect . . . 26
2.6 Summary and Conclusions . . . 28

3 Parallel Path Swapping in Transition Interface Sampling **30**
3.1 Abstract . . . 30
3.2 Transition Interface Sampling . . . 31
3.2.1 Shooting Move Algorithm . . . 32
3.3 Parallel Path Swapping . . . 34
3.3.1 Motivation . . . 34
3.3.2 Algorithm . . . 36
3.4 Benchmark Problem . . . 38
3.5 Implementation and Efficiency Analysis . . . 41
3.5.1 Parallelizing TIS . . . 41
3.5.2 Pre-Alpha Version: Implementation . . . 42
3.5.3 Pre-Alpha Version: Analysis . . . 44
3.5.4 Alpha Version: Implementation . . . 45
3.5.5 Alpha Version: Analysis . . . 48
3.5.6 Beta Version: Implementation . . . 49
3.5.7 Beta Version: Analysis . . . 51
3.5.8 Beta Version: Comparison with TIS . . . 53
3.6 Future Work . . . 54
3.6.1 Implementation . . . 54
3.6.2 Timing Analyses . . . 55

4 Investigating dislocation motion through a field of solutes with atomistic simulations and reaction rate theory **56**
4.1 Abstract . . . 56
4.2 Introduction . . . 57
4.3 Methods . . . 60
4.3.1 Transition State Theory . . . 60
4.3.2 Finite Temperature String Method . . . 62
4.3.3 Transition Interface Sampling . . . 63
4.3.4 Partial Path TIS . . . 65
4.4 Simulation Details . . . 67
4.5 Results and discussion . . . 69
4.5.1 Comparison of the methods . . . 71
4.5.2 Temperature Effect . . . 73
4.5.3 Load Effect . . . 78
4.6 Summary and Conclusions . . . 81

5 Atomistic prediction of dislocation motion through kink-pair nucleation in BCC metals **87**
5.1 Abstract . . . 87
5.2 Introduction . . . 88
5.3 Methods . . . 92
5.3.1 Transition State Theory . . . 92
5.3.2 Transition Interface Sampling . . . 98
5.3.3 Finite Temperature String Method . . . 102
5.4 Simulation Details . . . 105
5.4.1 Cell Dimensions . . . 108
5.4.2 Empirical Potential . . . 110
5.5 Results and discussion . . . 111
5.5.1 Finite Temperature String Method . . . 111
5.5.2 Comparison of the methods . . . 114
5.5.3 The entropy barrier . . . 118
5.6 Summary and Conclusions . . . 126

Bibliography **129**

CHAPTER 1
INTRODUCTION

Plastic deformation in metals and alloys stems from dislocation motion. That is why building dislocation mobility laws is the first step in multi-scale plasticity models such as Crystal Plasticity, Dislocation Dynamics and Kinetic Monte Carlo Simulations. The vast majority of dislocation mobility models in the literature are based on different variants of the Harmonic Transition State Theory (HTST), continuum elasticity models and empirical models. The validity of these models has rarely been tested using high fidelity atomistic simulations at experimental time-scales. In this dissertation, modern and traditional atomistically informed rate theories are utilized to study the rate and thermodynamics of three main dislocation motion mechanisms:

1. Dislocation motion through precipitates
2. Dislocation motion through a field of solutes
3. Dislocation motion through kink-pair nucleation

The performance of some of the most common approaches for predicting the rate of these problems is examined by comparing their predictions to benchmarks obtained from direct MD simulations. The assumptions behind the conventional models are revisited and simple and accurate alternative models are proposed.

Chapter 2 is a published paper in the Journal of Mechanics and Physics of Solids on atomistic prediction of the rate of dislocation motion through precipitates. First, predictions of different variants of HTST, as the most common rate

theory in the literature, are compared to benchmark predictions obtained from MD simulations. It is shown that HTST-based models provide grossly inaccurate predictions due to the anhramonic effect of thermal softening. Given the importance of the thermal effects, the utility of the Finite Temperature String method for computing a free energy profile is examined next. FTS is found to be successful in computing a reaction coordinate but fails to predict a reliable free energy profile as some of its key assumptions are not satisfied in this problem. Motivated by the restrictive assumptions of TST-based methods and FTS, the utility of the Transition Interface Sampling approach is examined next, because the method is known to be less reliant on the choice of the reaction coordinate and does not involve free energy calculations. TIS is found to provide accurate predictions of the rate relative to the MD benchmarks. The method is therefore used to study the load and temperature dependence of the rate at experimental time-scales. The temperature study shows that the Meyer-Neldel (MN) rule, as the most common entropy prediction approach in material mechanics, provides accurate estimates of the entropy barrier. Given that the MN rule is known to be an empirical model, atomistic validation of this approach for dislocation-precipitate interactions can be of significant interest to the community. Moreover, the MN rule can be used in the TST rate formula to provide a very simple, yet accurate, rate prediction approach.

In Chapter 3, the utility of the Parallel Path Swapping approach in improving the efficiency of TIS is studied. TIS utilizes a Markov Chain Monte Carlo (MCMC) sampling technique, called the shooting move, for generating trajectories of the system in different regions of the phase space. Like all MCMC techniques, the shooting move can suffer from correlated samples and hence slow convergence. Parallel Path Swapping helps increase the efficiency of the

shooting move by allowing MCMC simulations that are run in parallel exchange samples with each other, and therefore accelerates the random walk involved in MCMC algorithms. In addition to accelerating TIS, PSTIS allows for sampling multiple reaction channels, a property that regular TIS does not enjoy. A parallel implementation of the algorithm is explained and its efficiency is tested in this chapter.

Chapter 4 is a paper about atomistic prediction of the rate of dislocation motion through a field of solutes, which is under the final round of reviews with Acta Materialia. Dislocation motion through a field of solutes is known to have two dominant regimes:

1. Smooth motion: The dislocation overcomes one or a few obstacles at a time and therefore the energy barrier is of diffusive nature. This mechanism is dominant at low loads and high temperatures.
2. Jerky motion: The dislocation overcomes an array of obstacles and therefore the process has a single barrier energy landscape. This mechanism is dominant at high loads and low temperatures.

It is shown that HTST underestimates the rate by up to three orders of magnitude and cannot distinguish between the two mechanisms. TIS is found to be capable of accurately predicting the rate in the jerky motion regime, but fails to do so in the smooth motion regime. To address this issue, the Partial Path TIS approach — which is a variant of TIS designed for diffusive barriers — is utilized and its predictions are found to be accurate in the smooth motion regime. The two methods are then used to conduct a study on the entropy barrier that reveals that the MN rule provides fairly accurate predictions but it is not as ac-

curate as it was found to be for dislocation-precipitate interactions. Potential culprits are discussed and a simple alternative model for predicting the entropy barrier is proposed.

The final chapter is a manuscript on atomistic prediction of kink-pair nucleation in tungsten, as an example of BCC transition metals. An interesting observation in this chapter is that not only HTST fails to predict the rate but also TIS and FTS need to be modified based on physical intuitions about the problem in order to provide accurate predictions. This shows that there is no silver bullet approach and therefore a rate theory should be closely tested against direct MD predictions before being applied for an application of interest. It is also shown in this chapter that the MN rule significantly underestimates the entropy barrier. This, combined with the inaccuracy of HTST, shows that the vast majority of dislocation mobility laws for screw dislocations are inaccurate. The theoretical justification of the MN rule for dislocation processes, which is often neglected in the literature, is revisited and the conditions under which the method is expected to be accurate are discussed. It is also revealed that the problem has a large configurational entropy barrier that is often neglected but can be estimated from a very simple model.

CHAPTER 2

HARNESSING ATOMISTIC SIMULATIONS TO PREDICT THE RATE AT WHICH DISLOCATIONS OVERCOME OBSTACLES

By S. Saroukhani, L.D. Nguyen, K.W.K Leung, C.V. Singh, D. Warner

As published in Journal of the Mechanics and Physics of Solids 90 (2016) 203-214

2.1 Abstract

Predicting the rate at which dislocations overcome obstacles is key to understanding the microscopic features that govern the plastic flow of modern alloys. In this spirit, the current manuscript examines the rate at which an edge dislocation overcomes an obstacle in aluminum. Predictions were made using different popular variants of Harmonic Transition State Theory (HTST) and compared to those of direct Molecular Dynamics (MD) simulations. The HTST predictions were found to be grossly inaccurate due to the large entropy barrier associated with the dislocation-obstacle interaction. Considering the importance of finite temperature effects, the utility of the Finite Temperature String (FTS) method was then explored. While this approach was found capable of identifying a prominent reaction tube, it was not capable of computing the free energy profile along the tube. Lastly, the utility of the Transition Interface Sampling (TIS) approach was explored, which does not need a free energy profile and is known to be less reliant on the choice of reaction coordinate. The TIS approach was found capable of accurately predicting the rate, relative to direct MD simulations. This finding was utilized to examine the temperature and load dependence of the dislocation-obstacle interaction in a simple periodic cell configuration. An attractive rate prediction approach combining TST and simple continuum mod-

els is identified, and the strain rate sensitivity of individual dislocation obstacle interactions is predicted.

2.2 Introduction

The outcome of dislocation-obstacle interactions can be highly sensitive to the nanoscale details of the interaction [109, 108]. This motivates the use of atomistic modeling techniques to study these interactions. A key challenge for the atomistic modeling approach is that dislocation motion across obstacles is a thermally activated event, and hence rare in the time-scale accessible to direct atomistic modeling. This motivates the development and application of indirect atomistic modeling techniques, aimed at computing the rate at which dislocations overcome obstacles.

One of the most common indirect atomistic modeling approaches to compute the rates of thermally activated events is Harmonic Transition State Theory (HTST). HTST assumes that the reaction rate is governed by a single energy barrier that separates the initial (unreacted) and final (reacted) states of the system. Further, HTST assumes that the potential energy surface is quadratic at the initial and saddle configurations. This equates to approximating the activation entropy by the vibrational entropy and neglecting anharmonic effects such as thermal expansion [127], an approximation often believed to be accurate for solids [130, 36]. This approach produces a rate expression similar to that of the Arrhenius equation involving a pre-exponential factor and an activation potential energy. The latter can be accurately calculated using minimum energy path techniques such as the Nudged Elastic Band (NEB) method [61] and the

0K String method [133]. Calculating the pre-exponential factor requires solving two eigenvalue problems for the normal frequencies of the system near the initial and saddle configurations.

The eigenvalue problems are formidable for large systems and hence are often avoided in practice [56, 50, 99, 140, 54]. A common approach for avoiding the large eigenvalue problem is to approximate the pre-exponential factor by the normal frequency along the reaction coordinate at the initial state [54]. This is equivalent to assuming that the entropy barrier is zero. Other approximations for the pre-exponential factor such as the imaginary frequency of the saddle configuration [99], continuum estimates [140], and the Debye frequency have also been used in the literature. Henceforth, we will refer to these approaches as Simplified HTST (SHTST).

Due to the approximations mentioned above, the HTST and SHTST approaches are not universally able to accurately predict reaction rates in solids. A recent example is the prediction of dislocation nucleation rates, which has been shown to have large entropic barriers due to anharmonic effects [86, 87, 131, 54, 102, 64]. In these cases, other approaches such as Parallel Replica Dynamics (PRD) [129, 131], Hyperdynamics [130, 128, 54, 5] and Transition State Theory (TST) combined with different free energy calculation techniques such as the Finite Temperature String (FTS) method [96, 97] and Umbrella Sampling [46] have been successfully used to predict rates from atomistic simulations. However, each of these methods is known to have certain restrictions, which limit their accuracy and applications in a consistent manner. For instance, PRD provides a speedup that at most scales with the number of replicas used and hence can only handle problems with high rates and small activation volumes. The Hy-

perdynamics approach, on the other hand, needs an artificial potential that is application specific and non-trivial to design. Finally, TST strongly relies on the choice of reaction coordinate and a dividing surface, i.e. a transition bottleneck, which can be challenging to define.

To overcome the challenges involved in the above methods, path sampling techniques have drawn significant attention in the biophysics and chemistry communities [44, 62, 10, 12, 18, 106, 7]. A major advantage is that these methods do not need a carefully defined reaction coordinate and prior knowledge on the transition path and mechanism. They are based on the fact that a transition is fully characterized by the transition path ensemble (TPE). In other words, the TPE contains the information needed to predict all transition features such as reaction coordinate(s), rate(s), free energy profile(s) and mechanism(s) [90, 119, 15, 33, 1, 34, 35]. Comprehensive reviews of such methods can be found in [44, 80, 15, 9, 14, 32]. Nevertheless, these techniques have not so far been utilized for understanding phenomena underlying plasticity and fracture in metallic systems. In this manuscript, the TPE approach known as Transition Interface Sampling [119] will be utilized to predict the rate at which an edge dislocation overcomes an obstacle.

This chapter examines the application of HTST, TST, and TIS to predict the rate at which an edge dislocation overcomes an obstacle. The manuscript begins with a brief description of the theoretical background of each method in Section 2.3. Atomistic simulation details are given in Section 2.4. In Section 2.5.1, HTST, TST, and TIS predictions are compared to that of direct molecular dynamics (MD) simulations for a benchmark problem. The entropy barrier of the problem and the validity of the harmonic approximation are examined in Sec-

tion 2.5.2. In Section 2.5.3, the rate calculation is applied to predict the strain rate sensitivity (SRS) factor for an Al-Cu alloy, which can be compared to experimental measurements. The final section draws some conclusions from the analyses and points out potential future directions.

2.3 Methods

2.3.1 Transition State Theory

Transition State Theory (TST) provides an exact expression for the rate at which an ergodic system crosses a dividing surface, S_D, partitioning the configuration space into two sets a and b:

$$k_{ab}[S_D] = \sqrt{\frac{k_B T}{2m\pi}} \frac{Z_{S_D}}{Z_a} \tag{2.1}$$

with k_B being the Boltzmann constant, T the temperature, m the effective mass, $Z_{S_D} = \int_{S_D} e^{-\frac{V(\mathbf{x})}{k_B T}} d\sigma(\mathbf{x})$ and $Z_a = \int_a e^{-\frac{V(\mathbf{x})}{k_B T}} d\mathbf{x}$ are the constrained partition functions associated with S_D and a respectively. The term $\sqrt{\frac{k_B T}{2m\pi}}$ is the flux through the dividing surface and $\frac{Z_{S_D}}{Z_a}$ represents the probability of the system being on S_D relative to a [49, 45, 137, 58, 80, 15]. Often, a surface, S_0, which does not intersect S_D and contains an initial configuration in a, is defined to express Eq. 2.1 in terms of a free energy barrier [80, 127]:

$$k_{ab}[S_D] = \tilde{\nu} e^{-\frac{\Delta F}{k_B T}} \tag{2.2}$$

where

$$\tilde{\nu} = \sqrt{\frac{k_B T}{2m\pi}} Z_a^{-1} \int_{S_0} e^{-\frac{V(\mathbf{x})}{k_B T}} d\sigma(\mathbf{x}) \tag{2.3}$$

and the free energy barrier is

$$\Delta F = F_{S_D} - F_{S_0} = -k_B T \ln \left(\frac{\int_{S_D} e^{-\frac{V(\mathbf{x})}{k_B T}} d\sigma(\mathbf{x})}{\int_{S_0} e^{-\frac{V(\mathbf{x})}{k_B T}} d\sigma(\mathbf{x})} \right) \tag{2.4}$$

which can also be written as

$$\Delta F(\sigma, T) = \Delta U(\sigma, T) - T\Delta S(\sigma, T) \tag{2.5}$$

with $\Delta U(\sigma, T)$ being the activation internal energy and $\Delta S(\sigma, T)$ the activation entropy. It should be noted that $\tilde{\nu}$, ΔF, ΔU and ΔS are not intrinsic properties of the system with respect to S_D as they depend on S_0. In practice, however, these quantities are often not appreciably dependent on the choice of S_0 so long as it is physically reasonable, e.g. passing through the minimum energy state in a and normal to an appropriate reaction coordinate.

One challenge in computing the rate from Eq. 2.2 is that one is often interested in the transition rate between two metastable regions $A \subset a$ and $B \subset b$ that do not necessarily partition the phase space and hence a transition cannot be exactly characterized by crossing a hypersurface. In such cases, the flux through the dividing surface is an upper bound to the flux from one metastable state to another because trajectories might recross S_D multiple times before committing to B or may not commit to B at all. Therefore, the TST rate formula, Eq. 2.2, can overestimate the actual rate of interest, i.e.

$$k_{AB} \leq k_{ab}[S_D] \tag{2.6}$$

A standard approach for dealing with the above challenge is the Bennett-Chandler (BC) TST method [8, 27, 80] whereby the flux through S_D is modified

such that only trajectories that reach the final state are counted and multiple recrossings are counted only once. The latter is done by weighting forward and backward crossings with different signs such that they cancel out. In practice, this amounts to scaling $k_{ab}[S_D]$ by the probability, κ, that each crossing towards B leads to a transition, meaning

$$k_{AB} \approx \kappa k_{ab}[S_D] \tag{2.7}$$

where $\kappa = \lim_{N\to\infty} \frac{2N_B}{N}$, a.k.a. the transmission coefficient, is computed by starting a large number, N, of trajectories from an equilibrium distribution on S_D and counting the number, N_B, that commit to B in a time $t^* << 1/(k_{AB} + k_{BA})$. For the BC-TST approach to be effective, the dividing surface, S_D, must be chosen such that κ is close to one. In other words, S_D must be a bottleneck for the transition such that trajectories crossing it have a high probability of committing to B. Otherwise, an infeasible number of trajectories are needed to compute κ accurately. It is worth noting that there are more efficient approaches for defining κ based on the *effective positive flux* formalism [121], which avoids counting positive and negative crossings by only counting the first *positive* crossing for *effective* trajectories [15].

A less demanding approach is the Variational TST (VTST) that assumes $\kappa = 1$ and chooses S_D as the surface, $S_D^{\min}$, that minimizes the transition frequency, $\nu = k_{ab}[S_D]Z_a$ [122, 117]. Considering the TST rate formula, Eq. 2.2, $S_D^{\min}$ is the surface that minimizes $\int_{S_D} e^{-\frac{V(\mathbf{x})}{k_B T}} d\sigma(\mathbf{x})$ and hence has the highest free energy. In other words, VTST assumes that the bottleneck characterized by S_D that needs to be overcome for the transition to happen is the activation free energy. In order to find this surface, one needs to compute a free energy profile along a properly chosen reaction coordinate, λ, whereby $S_D^{\min}$ can be taken as the level set, $\lambda = \lambda^*$, with the highest free energy. The Finite Temperature String (FTS)

method described in the next subsection can be used for this purpose.

The demanding task of computing a free energy profile for the above methods motivates the Harmonic TST (HTST) approach, which avoids this task by assuming that the potential energy surface is quadratic at the initial and saddle configurations. This assumption amounts to temperature independent material properties and is widely used for problems involving solids. The method further assumes that the dividing surface corresponds to a potential energy ridge, S_D^V, between A and B to express the transition rate as

$$k_{AB} \approx \left(\frac{\prod_{i=1}^{3N} \nu_i^{\text{initial}}}{\prod_{i=1}^{3N-1} \nu_i^{\text{saddle}}} \right) e^{-\frac{\Delta V}{k_B T}} = \nu_0 e^{-\frac{\Delta V}{k_B T}} \tag{2.8}$$

where ν_i^{initial} and ν_i^{saddle} are respectively the normal frequencies of the system in the initial configuration and the minimum potential energy configuration within S_D^V, i.e. the saddle configuration. The product over the saddle point frequencies excludes the imaginary frequency in the direction of the reaction coordinate, i.e. normal to S_D^V, and hence all frequencies are real. N is the number of atoms in the system and ΔV is the difference in the potential energy between the saddle and initial configurations.

Solving the two eigenvalue problems required for Eq. 2.8 becomes prohibitively expensive for large systems. That is why Eq.2.8 is sometimes further simplified by assuming that the prefactor is equal to the normal frequency, ν_*^{initial}, in the direction of the reaction coordinate in the initial state:

$$k_{AB} \approx \nu_*^{\text{initial}} e^{-\frac{\Delta V}{k_B T}} \tag{2.9}$$

We will refer to this approach as the Simplified HTST (SHTST). Other choices for the pre-factor such a continuum estimate, the imaginary frequency of the

saddle point, or the Debye frequency have also been used in the literature [54, 99, 140, 50].

2.3.2 Finite Temperature String Method

FTS is an algorithm for finding a reaction coordinate and computing the free energy profile along the coordinate. It has been extensively used with TST to predict reaction rates [87, 86, 98, 95]. The method utilizes the idea of reaction tubes, a relatively high probability region in configuration space that links A and B. Assuming that reaction tubes are thin and isolated, the method offers an algorithm for finding iso-committer surfaces, i.e. surfaces where the probability that a trajectory reaches B before A is uniform, and the expected configuration on each of them. A reaction coordinate is then defined as a curve (string) connecting the expected configurations. We refer the interested reader to Refs. [96, 97, 98, 124, 134] for further details on the theoretical background of the method.

The algorithm starts with an initial string connecting the initial and final states through a set of equally spaced intermediate configurations (images) and a set of Voronoi cells centered at the images. Constrained sampling at constant temperature is performed within each cell and the time averaged position associated with each cell is computed. Then, the time averaged positions are used to update the string and Voronoi cells, while satisfying a smoothing condition and enforcing equal distance between images. Iterating over this process leads to a converged string and its associated Voronoi cells. The Voronoi cells approximate the iso-committer surfaces and the images approximate the expected

configuration within them. The quality of the approximation depends on the discretization error and the sampling error. Further details of the algorithm can be found in [124, 98].

FTS also offers an algorithm for calculating the free energy profile. The algorithm uses the global balance equation,

$$\sum_{\substack{\alpha'=0 \\ \alpha' \neq \alpha}}^{N} \pi_{\alpha'} k_{\alpha'\alpha} = \sum_{\substack{\alpha'=0 \\ \alpha' \neq \alpha}}^{N} \pi_{\alpha} k_{\alpha\alpha'} \tag{2.10}$$

together with

$$\sum_{\alpha=0}^{N} \pi_{\alpha} = 1 \tag{2.11}$$

to find the equilibrium probabilities, π_α, of the cells $\alpha = 0, ..., N$. The transition matrix, $k_{\alpha\alpha'}$, can be computed from the formula

$$k_{\alpha\alpha'} = \frac{N^n_{\alpha\alpha'}}{n\Delta t} \tag{2.12}$$

by initiating a trajectory inside cell α and counting the number of times, $N^n_{\alpha\alpha'}$, the trajectory enters cell α' over n timesteps of Δt. When the trajectory leaves the cell where it was initiated, which is α in this case, it is brought back to the last configuration it had before leaving the cell. The estimate in Eq.2.12 converges as the length of the trajectory goes to infinity, i.e. $n \to \infty$. Further details can be found in [124].

2.3.3 Transition Interface Sampling

Like TST based approaches, TIS aims to calculate a flux, but it does not require a transition state to be identified a priori nor does it require a carefully chosen reaction coordinate and the computation of the free energy profile along the coordinate [119]. These advantages stem from the fact that the method directly

calculates the rate using actual trajectories of the system, i.e. samples of the Transition Path Ensemble (TPE). TIS measures the flux through a set of hypersurfaces partitioning phase space rather than a single dividing surface, which can be hard to define. The TIS method is based on the *effective positive flux* formalism [15, 121] which makes it less sensitive to recrossings.

The first step in TIS is to partition phase space using a set of $n + 1$ non-intersecting interfaces, defined as level sets, λ_i, of an order parameter, $\lambda(\mathbf{x})$, i.e. $\{\mathbf{x}|\lambda(\mathbf{x}) = \lambda_i\}$, $i = 0, ..n$. The order parameter, $\lambda(\mathbf{x})$, does not have to be associated with a properly chosen reaction coordinate; it is sufficient that $\lambda(\mathbf{x})$ characterizes the basins of attraction of A and B [80, 119, 121]. As schematically shown in Fig. 2.2, each interface, λ_i, is closer to A than the next interface, λ_{i+1}, such that $\lambda_0 = \lambda_A$ defines the boundary of the basin of attraction of A and $\lambda_n = \lambda_B$ defines that of B.

TIS makes use of the *effective positive flux* formalism to express the transition rate as

$$k_{AB} = \frac{\langle \phi_{\lambda_0,\lambda_n} \rangle}{\langle h_{\mathcal{A}} \rangle} \tag{2.13}$$

where $h_{\mathcal{A}}$ is the indicator function and $\phi_{\lambda_0,\lambda_n}$ is the *effective positive flux* from state A through interface λ_n [119]. $\mathcal{A}$ is the set of all phase points where the corresponding trajectories come from A without having visited B. A transition happens when the system leaves $\mathcal{A}$, i.e. when the system enters B for the first time. The denominator, $\langle h_{\mathcal{A}} \rangle$, is the fraction of time the system spends in $\mathcal{A}$. Therefore, Eq. 2.13 is the exact definition of rate, which is the number of *effective* transitions from A to B divided by the total time the system spends in $\mathcal{A}$, in the limit of time going to infinity. It is also worth noting that the equation is equivalent to the TST rate formula when $S_D = \lambda_A = \lambda_B$, i.e. when the transition is character-

ized by crossing a single dividing surface.

Calculating the rate from Eq. 2.13 is not feasible as it requires simulations that are long enough to capture a rare transition. To overcome this challenge, TIS relates the flux through an interface, λ_i, to that of the previous interface, λ_{i-1}, using the recursive formula

$$\langle \phi_{\lambda_0,\lambda_i} \rangle = \langle \phi_{\lambda_0,\lambda_{i-1}} \rangle P(\lambda_i|\lambda_{i-1}) \tag{2.14}$$

where $P(\lambda_i|\lambda_{i-1})$ is the probability that a trajectory, coming from A, crosses λ_i provided that it has already crossed λ_{i-1} [119, 82, 20]. For instance in Fig. 2.2, $p(\lambda_4|\lambda_3)$ is the fraction of blue trajectories to the red and blue trajectories. In simpler words, this equation relates the flux through two neighbor interfaces by using the fact that only a fraction of trajectories that cross λ_{i-1} make it to λ_i before going back to A. That fraction is the probability $P(\lambda_i|\lambda_{i-1})$. Using the recursive formula in Eq. 2.14, we can express $\langle \phi_{\lambda_0,\lambda_n} \rangle$ as

$$\langle \phi_{\lambda_0,\lambda_n} \rangle = \langle \phi_{\lambda_0,\lambda_1} \rangle \prod_{i=1}^{n-1} P(\lambda_{i+1}|\lambda_i) \tag{2.15}$$

and hence rewrite Eq. 2.13 as

$$k_{AB} = \frac{\langle \phi_{\lambda_0,\lambda_1} \rangle}{\langle h_{\mathcal{A}} \rangle} \prod_{i=1}^{n-1} P(\lambda_{i+1}|\lambda_i) \tag{2.16}$$

where the term $\frac{\langle \phi_{\lambda_0,\lambda_1} \rangle}{\langle h_{\mathcal{A}} \rangle}$ is the rate of transition from λ_0 to λ_1, which can be computed using direct MD simulations.

The trajectories needed for calculating the probabilities $P(\lambda_{i+1}|\lambda_i)$ cannot be generated using direct simulations for interfaces that are far from A. A method commonly used for this purpose in the TIS literature is the so-called 'shooting move', which is a Metropolis Markov Chain Monte Carlo (MCMC) algorithm. The theoretical and algorithmic details of the method can be found in [119] and

[13]. The algorithm ensures generating samples from the Boltzmann distribution by satisfying the detailed balance equation and using the Boltzmann distribution for deriving the acceptance rule. Like other MCMC algorithms, the shooting move suffers from correlated samples, which slow down convergence and impede exploring multiple reaction channels.

Path Swapping TIS (PSTIS) is one approach to attempt to overcome the correlation problem. It is based on the idea that trajectories that have crossed an interface, λ_i, might also cross the neighboring interfaces, λ_{i-1} and λ_{i+1}. In other words, trajectories in an ensemble, $P(\lambda_{i+1}|\lambda_i)$, might also be in the neighboring ensembles, $P(\lambda_i|\lambda_{i-1})$ and $P(\lambda_{i+2}|\lambda_{i+1})$. This means an ensemble can exchange samples, i.e. trajectories, with its neighbors. In that case, a new sample is added to each of the ensembles without performing the most expensive step of the shooting move, i.e. the integration. This also alleviates the correlation problem and increases the chance of exploring multiple reaction tubes. Further details on the algorithm can be found in [118].

2.4 Simulation Details

The atomistic simulations were conducted using a modified version of the LAMMPS package and an angular dependent embedded atom method (EAM) empirical potential developed by Apostle and Mishin [2].The simulation cell consisted of an edge dislocation in an FCC Al lattice and a mono-layer Cu obstacle representing a GP-zone. The simulation box, Fig. 2.1, contained approximately 13,000 atoms in total, with 13 Cu atoms in the obstacle. The box was bounded by $(1\bar{1}0)$, (111), and $(\bar{1}\bar{1}2)$ faces in the X, Y, and Z directions, respec-

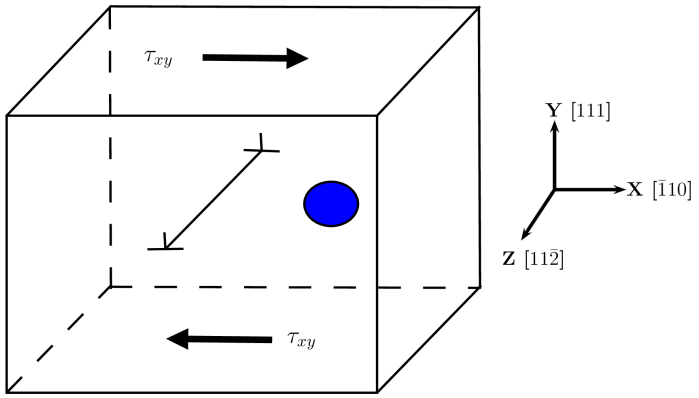

Figure 2.1: Simulation cell with an edge dislocation and a precipitate.

tively. The GP-zone lied on the (100) plane. An edge dislocation was created with a line direction parallel to the Z-axis and $b = 1/2[\bar{1}10]$. Periodic boundary conditions were applied in the X and Z directions. The system was loaded by applying the shear forces

$$f_{top} = \frac{\tau_{xy} A_{xz}}{N_{top}}, \qquad f_{bottom} = -\frac{\tau_{xy} A_{xz}}{N_{bottom}} \tag{2.17}$$

on the atoms near the top and bottom Y surfaces, while the displacements of the atoms in those layers are determined by the dynamics of the system.

Direct MD simulations were performed with NVT dynamics where a Langevin thermostat with a damping parameter of 1 ps was used. The NVT ensemble was chosen because of implementation convenience. As proved in [103], the choice of the ensemble does not affect the activation free energy and hence the rate, but the entropy barriers are different. Our analysis showed that the choice does not affect the conclusions drawn about temperature effects in Section 2.5.2. Further, convergence studies with respect to the loading rate were conducted to ensure the fidelity of the rate predictions.

As mentioned in Section 2.3, HTST and TST rate expressions involve the po-

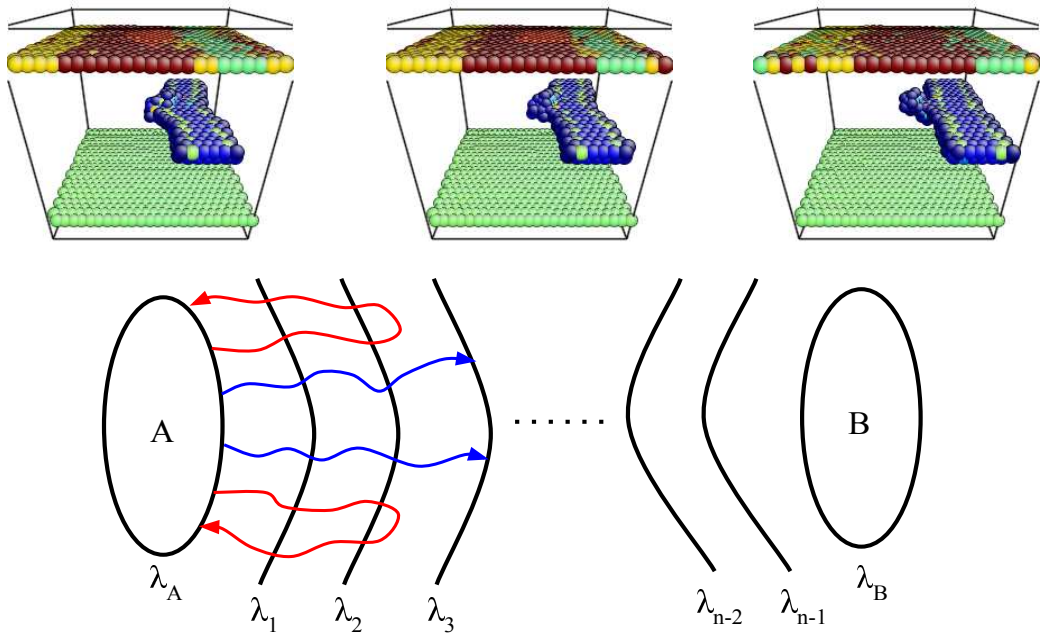

Figure 2.2: Bottom: A schematic picture of the interfaces and trajectories involved in TIS calculations. The interfaces are the boundaries of the cells defined by the FTS method. The blue and red trajectories have been described in Sec. 2.3. Top: Snapshots of the system as the dislocation overcomes the obstacle at τ_{xy} = 200 MPa and T = 300K. The left image is the initial configuration where the first partial dislocation has overcome the obstacle and the second partial has not. The right image is the final configuration where the second partial has overcome the obstacle. The middle image is the center of one of the intermediate cells. The images have been plotted by AtomEye [70]. Only atoms not in a perfect FCC stacking, i.e. having a large centro-symmetry parameter, are shown.

tential and free energy barriers respectively. The potential energy barrier ΔV is computed using the 0K string method [133], which is equivalent to the Nudged Elastic Band (NEB) approach [61]. The FTS method is used to obtain a reaction coordinate and compute the free energy profile, as discussed in Section 2.3.2. Both versions of the string method require an initial string connecting the initial and final configurations through a set of intermediate ones. This string has been

generated by interpolation using the Euclidean norm.

The set of interfaces for TIS was simply defined as the boundaries between Voronoi cells of the convergent string given by the FTS method. The string was also used as the initial trajectory needed to start the shooting move. The simulations to compute $P_A(\lambda_{i+1}|\lambda_i)$ for each λ_i were performed in parallel. For each λ_i , five to ten 1 ns simulations, started at different seeds, were performed. The transition flux through the first interface, $\frac{\langle \phi_{\lambda_0,\lambda_1} \rangle}{\langle h_{\mathcal{A}} \rangle}$, was calculated using 50 independent direct MD simulations started at different seeds.

2.5 Results and discussion

2.5.1 Comparison of the methods

The performance of the methods described in Sec. 2.3 was examined by comparing their predictions of the average time for a dislocation to overcome an obstacle, $\bar{t} = k_{AB}^{-1}$, to a benchmark obtained by direct MD simulations at τ_{xy} = 200MPa and T = 300K (Table. 2.1). The choice of the load was based on the limited time-scale accessible to MD simulations and the athermal critical shear stress, $\hat{\tau}$ = 300MPa. In this case, the rate controlling event was observed to be the second partial dislocation overcoming the obstacle through Orowan looping [107]. Therefore, the results may be generalized to other strong obstacles lying on other planes. Fig. 2.2 shows the initial, final and an intermediate configuration of the system, plotted using AtomEye [70]. The benchmark was obtained by running 50 statistically independent direct MD simulations and averaging the transition time, i.e. the time for the second partial to overcome the obstacle.

Method	$\bar{t}$ (ns)
Direct MD	8.99
PSTIS	3.8
TIS	2.27
HTST	1.48×10^{14}
SHTST	1.26×10^{11}
FTS	N/A

Table 2.1: The predictions of the methods described in Sec. 2.3 for the average time, $\bar{t}$, for an edge dislocation to overcome an obstacle at τ_{xy} = 200 MPa and T = 300K.

As shown in Table. 2.1, HTST overestimated $\bar{t}$ by about 13 orders of magnitude relative to the direct MD prediction. The activation energy obtained by the 0K string method was ΔV = 0.91 eV. The pre-exponential factor ν_0 obtained by solving for ν_i^{initial} and ν_i^{saddle} in Eq. 2.8 was 1.3×10^{10} s^{-1}. A SHTST prediction based on the Debye frequency of aluminum, 1.54×10^{13} s^{-1}, is also shown in the table, which overestimates $\bar{t}$ by 11 orders of magnitude. As discussed in the next subsection, the inaccuracy of the HTST predictions is due to the large entropic barrier due to thermal softening, which is neglected by the harmonic approximation.

Our efforts to compute a free energy profile using FTS were frustrated. Although the method results in a converged reaction coordinate (string) in the first stage of the algorithm, the constrained sampling of the second stage fails to obtain a converged transition matrix. We believe that this problem stems from the failure of key FTS assumptions. First, reaction tubes are assumed to be separated by energy barriers significantly larger than the thermal energy so that trajectories do not leave the tube where they were initiated. Second, reaction tubes are assumed to be thin so that iso-committor surfaces can be approximated by hyperplanes. A consequence of these assumptions is that the sampling trajecto-

ries must spend most of their time near their respective cell centers. This means that the time averaged positions of the sampling trajectories will form a smooth curve along the cells. A feature that was not observed in the simulations performed here.

It should be noted that failure in obtaining a converged transition matrix does not contradict a convergent string in the first stage for two reasons. First, there is a smoothing term in the first stage that ensures the time averaged positions of neighbor cells are smoothly connected; whereas, there is no such constraint when calculating the transition matrix. Further, in the first stage, trajectories making a transition to a new tube do not remain there long enough to change their respective cell centers. This is because trajectories are brought back to their cell centers as soon as they leave the cells. When calculating the transition matrix, on the other hand, trajectories are brought back to the last configuration they had before leaving their cells, which could be far from the cell centers.

TIS performs better than the other methods and provides a fairly accurate prediction of the average time, $\bar{t}$. This is because TIS does not rely on prior knowledge about the transition such as the reaction coordinate, free energy profile, transition state and the nature of the entropy barrier. Instead, it directly computes the flux characterizing the rate using real trajectories of the system, i.e. samples of the Transition Path Ensemble (TPE). The success of the TIS approach and the failure of the TST-FTS approach shows the importance of this level of generality.

We believe that a considerable amount of the error in the TIS prediction is due to the correlated nature of the trajectories used to estimate $P(\lambda_{i+1}|\lambda_i)$. As

mentioned in Sec. 2.3, TIS makes use of an MCMC algorithm for generating trajectories of the system and hence the convergence is slowed down by the correlated nature of successive samples. Moreover, the correlation issue leads to most TIS trajectories lying in one reaction tube and not exploring others. As mentioned in Sec. 2.3, the Path Swapping version of TIS, which we call PSTIS, has been proposed to alleviate the correlation problem and facilitate exploring multiple reaction tubes. As shown in Table. 2.1, the method proves to be effective at improving the time average prediction in this problem.

2.5.2 Temperature Effect

To gain insight into the energetics associated with a dislocation overcoming an obstacle and the performance of the various rate prediction methods, the temperature dependence of the rate was examined. To this end, TIS rate predictions were carried out at four temperatures and placed on an Arrhenius plot with HTST predictions, i.e. $\ln(\bar{t})$ versus $\beta = 1/k_B T$ (Fig. 2.3). The simulations were performed at a constant shear stress of $\tau_{xy} = 120$MPa, with the potential energy barrier being $\Delta V = 1.0$ eV. The shear stress is about 3/4 of the yield strength in shear of underaged Al-4wt.%Cu, which is the closest Al-Cu alloy to the cell considered here.

Interestingly, the TIS predictions follow a linear trend on the Arrhenius plot, with the same slope as the HTST prediction, i.e. 1.0 eV. This implies that $\Delta U(\sigma, T)$, $\tilde{\nu}(\sigma, T)$ and $\Delta S(\sigma, T)$ are likely to be temperature independent over the range examined, considering that

$$\ln(\bar{t}) = -\ln[\tilde{\nu}(\sigma, T)] - \frac{\Delta S(\sigma, T)}{k_B} + \beta \Delta U(\sigma, T) \tag{2.18}$$

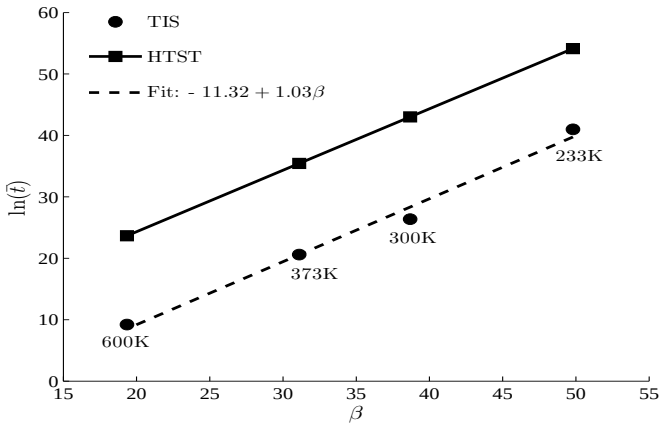

Figure 2.3: HTST (solid line) and TIS (dashed line) Arrhenius plots. HTST (squares) and TIS (circles) predictions have been computed at four temperatures: 233K, 300K, 373K and 600K. The average time, $\bar{t}$, is in picoseconds.

from Eq. 2.5, $\bar{t} = 1/k^{\mathrm{TST}}$, and Eq. 2.2. Accordingly, the y-intercept then represents the quantity $-(\ln[\tilde{\nu}(\sigma,T)] + \frac{\Delta S(\sigma,T)}{k_B})$, which can also be interpreted as the natural log of the prefactor in the Arrhenius equation for a process with a temperature independent energy barrier. The linear fit of the TIS data on the Arrhenius plot has a y-intercept of -11.3. This value is considerably below HTST intercept of 4.3 ($-\ln(\nu_0)$), and represents the main source of error in the HTST rate predictions.

Considering that $\tilde{\nu}(\sigma,T)$ can be easily computed from direct MD simulation, $\Delta S(\sigma,T)$ can be obtained. At T=300K, we found $\tilde{\nu} \approx 1.5 \times 10^{11}\ s^{-1}$. Therefore, the entropy barrier is $\Delta S = 13.2 k_B$, a value significantly beyond the 1-2 k_B range associated with the typical vibrational entropy of solids [101, 54].

The large entropy barrier likely results from the nature of the dislocation-obstacle interaction and the temperature dependence of the shear modulus and stacking fault energies [139]. Specifically, the activated state involves an increased dislocation length relative to the initial state. This makes the free energy

of the activated state more temperature dependent than the free energy of the initial state, which is described by a large entropy difference between the two states.

This idea is consistent with traditional continuum thermoelastic models, e.g. [38, 115, 105]. These models express the activation free energy as a function of the shear modulus, $\mu(T)$, as $\Delta F(\sigma, T) = \Delta V(\sigma)\frac{\mu(T)}{\mu(0)}$ [3, 101]. Based on this expression for ΔF and the assumption that μ linearly decreases with temperature and vanishes at the melting point T_m [3, 139, 84], the activation entropy is modeled as

$$\Delta S(\sigma) = \frac{\Delta V(\sigma)}{T_m} \tag{2.19}$$

This expression is equivalent to the 'thermodynamic compensation law' or the Meyer-Neldel rule, which is an empirical relation that has proved valid for many thermally activated processes.

Based on the melting point of Al-4wt.%Cu, T_m = 933K [79], the entropy barrier estimated by Eq. 2.19 is $12.4k_B$. This value is very similar to that obtained with Eq. 2.18 using the TIS approach. Furthermore, the model describes a temperature independent activation entropy, consistent with the TIS predictions.

These results not only illuminate the powerful utility of the Meyer-Neldel rule for predicting the rate at which dislocations overcome obstacles, but they show that the large entropy barrier associated with the phenomenon can be explained by the anharmonic effect of thermal softening.

2.5.3 Load Effect

The applied load is an important factor that controls the rate at which dislocations overcome obstacles. Macroscopically, this effect manifests itself in the dependence of the plastic strain rate, $\dot{\epsilon}_p$, on the applied stress, τ, and is characterized by a strain rate sensitivity (SRS) factor, $m = \frac{\partial \ln \tau}{\partial \ln \dot{\epsilon}_p}$, an experimentally measured quantity. $\dot{\epsilon}_p$ is proportional to the average velocity of dislocations, v. In alloys that are governed by dislocation-obstacle interactions, such as underaged Al-4wt.%Cu, a first order approximation of v under ordinary loading conditions is $v \approx d/\bar{t}$, with d being the average obstacle spacing in the glide direction of the mobile dislocations. Thus, m can be estimated directly from the TIS results that provide the stress dependence of $\bar{t}$.

Alternatively, m is commonly predicted from TST [138]. Often, $\tilde{\nu}$ is assumed to be stress independent and the form of ΔF is chosen based upon specific features of the system [65]. This allows m to be written as $m = -k_B T \frac{\partial \ln \tau}{\partial \Delta F}$. For a periodic array of weak obstacles, a widely used form for the stress dependence of ΔF is Friedel's model,

$$\Delta F = \Delta F_0 \left(1 - \frac{\tau}{\hat{\tau}}\right)^{\frac{3}{2}} \tag{2.20}$$

where the activation energy at zero stress, ΔF_0, is a fitting parameter and $\hat{\tau}$ is the athermal critical shear stress.

TIS rate predictions across six different stress levels at T=300K were examined within the context of the above assumptions (Fig. 2.4). Specifically, the $\bar{t}$ preditions were plugged into the TST rate formula, Eq. 2.2, and ΔF was solved for at the different stress levels. The ΔF versus τ data is also shown in Fig. 2.4. Using ΔF_0 = 1.7 eV, the data is described well by Friedel's model across a wide range of stresses.

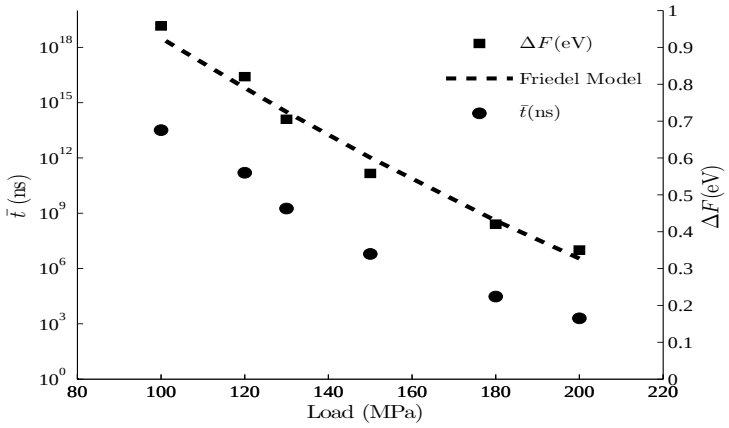

Figure 2.4: Activation energy and average time vs load at 300K.

The SRS factor, m, associated with the TIS predictions is between 0.03 and 0.05 depending upon the applied load, noting that similar results are obtained whether computing m directly from the TIS data or using the TST approach with Friedels model. Our predictions of m are almost an order of magnitude higher than those observed in room temperature experiments on traditional aluminum alloys hardened by dislocation precipitate interactions, $m \approx 0.005$ [84, 21]. This disconnect suggests that the experimentally measured strain rate sensitivity of such materials is not governed by the strain rate sensitivity of individual dislocation-obstacle interactions. This finding supports the hypothesis proposed by [91, 138, 136], that the strain rate sensitivity of many engineering alloys may instead by governed by the correlated motion of dislocations through a random field of obstacles. With that said, the reader is reminded that artificial boundary effects associated with the small periodic simulation cell utilized here might also be important [116].

2.6 Summary and Conclusions

This chapter documents our attempt to use atomistic simulation to predict the rate at which dislocations overcome obstacles. We began by considering the most common rate prediction approach for solids, HTST. For a small example problem that could be solved with direct MD, we found HTST incapable of predicting the rate. Hypothesizing that the harmonic approximation was the source of the error, the TST approach was then attempted. We were unable to predict the rate with the TST approach due to our inability to calculate a free energy profile along a reaction coordinate identified with the FTS method. We believe that the FTS approach was impeded by the failure of its key assumptions for this application. This motivated us to explore the TIS approach, which utilizes actual reactive trajectories to predict the rate. The TIS approach was found capable of accurately predicting the rate that dislocations overcome obstacles, relative to direct MD simulation. To better explore the energy landscape and improve the rate predictions, a path swapping algorithm was ultimately utilized within the TIS framework.

Having established the accuracy of TIS predictions for the application, the TIS approach was used to examine the temperature dependence of the dislocation-obstacle interaction and the validity of the harmonic approximation. To that end, TIS was used to generate an Arrhenius plot, which was compared to HTST predictions. The TIS plot was linear with the same slope as the HTST prediction, but with a different intercept. This suggests that the phenomenon of a dislocation overcoming an obstacle consists of a large entropy barrier that is temperature independent. The temperature dependence of the associated free energy barrier was found to be accurately described by standard continuum

models that include a thermal softening effect.

The TIS approach was also used to examine the stress dependence of the rate. The results were found to be well described by TST and Friedel's model for the stress dependence of the free energy barrier. The strain rate sensitivity for a dislocation to overcome a row of periodic obstacles in aluminum is predicted to be between $m = 0.03$ and $m = 0.05$ at room temperature, a finding that can aid the quest to better understand the processes that control the strength of real-world engineering alloys.

In closing, we have shown that the TIS approach is capable of accurately predicting the rate at which dislocations overcome obstacles and that simple continuum models are capable of describing the temperature and stress dependence of the rate. The latter finding establishes an attractive approximate approach for predicting the rate, i.e. using TST in careful combination with the simple continuum models examined here. For other problems where this is not the case or known, path sampling techniques such as TIS are attractive alternatives to TST-based approaches as they offer a much higher degree of generality for the same amount of implementation efforts.

Acknowledgements

The authors acknowledge Paul Hess at ONR (Grant No. N000141010323) for financially supporting this research.

CHAPTER 3

PARALLEL PATH SWAPPING IN TRANSITION INTERFACE SAMPLING

3.1 Abstract

Molecular dynamics simulations are limited to at most a few microseconds. This is much smaller than expected waiting times of many interesting phenomena such as protein folding, dislocation nucleation and etc. That is why the occurrence rate of such phenomena cannot be calculated using direct MD simulations. Transition Interface Sampling (TIS) is a method based on statistical physics and Monte Carlo path sampling techniques that aims to address this time-scale challenge. However, the method suffers from slow convergence and also fails to solve problems involving multiple reaction channels. Parallel Path Swapping is an algorithm developed to alleviate these problems in TIS simulations.

In this work, the algorithm has been implemented in an existing TIS code using MPI. In the original form of the TIS algorithm, the MCMC simulations for different interfaces are independent from one another. In the existing TIS code, the simulations are conducted on a separate processor for each interface. The Path Swapping TIS algorithm involves exchanging samples between simultaneous MCMC simulations associated with two neighboring interfaces. Given that the main purpose of the algorithm is not accelerating the existing TIS code, the concept of speedup does not directly apply here. Therefore, the performance of the PSTIS implementations in this work is examined in terms of the fraction of the communication and synchronization time to the simulation time.

The algorithm was implemented in three steps. In each step, a thorough analysis of the above-mentioned performance measure was conducted and the necessary changes for the next version were identified. The performance of the final version was compared to that of the original TIS for a benchmark problem and it was found that the algorithm provides more accurate predictions.

3.2 Transition Interface Sampling

Consider a thermodynamic event

$$A \rightarrow B \tag{3.1}$$

The first step in TIS in order to calculate the rate of this event is to partition the energy landscape between A and B using some hypersurfaces $\lambda_0 = \lambda_A, \lambda_1, .., \lambda_n = \lambda_B$, like the ones schematically shown in Fig. 3.1. Then, the rate constant k^{AB} can be calculated using

$$k^{AB} = f_A \prod_{i=0}^{n-1} p(\lambda_{i+1}|\lambda_i) \tag{3.2}$$

where f_A is the rate at which the system makes a transition from A to λ_A and $p(\lambda_{i+1}|\lambda_i)$ is the probability that a trajectory coming from A and crossing λ_i moves forward and crosses λ_{i+1} before going back to A [119]. For instance in Fig. 3.1, $p(\lambda_4|\lambda_3)$ is the fraction of the number of blue trajectories to the number of trajectories of both kinds, red and blue.

Since λ_A is chosen to be close to A, f_A can computed via direct MD simulations whereby sample trajectories are started in A and the average time $\bar{t}_A$ taken to reach λ_A is calculated which is then used to calculate $f_A = \frac{1}{\bar{t}_A}$. $p(\lambda_{i+1}|\lambda_i)$ cannot be calculated via direct simulations though, because MD trajectories are very

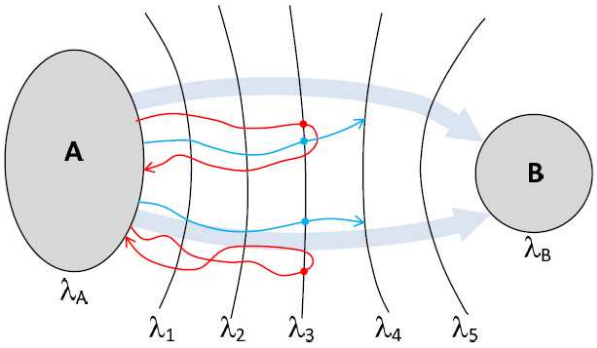

Figure 3.1: A schematic picture of the interfaces and trajectories involved in TIS calculations.

unlikely to visit regions of higher energy in the phase space, which is necessary in order to observe a transition. In order to generate samples of such trajectories, more advanced statistical techniques are required. The shooting move algorithm is the most well-known algorithm of this kind because of being simple, though effective [13].

3.2.1 Shooting Move Algorithm

The shooting move algorithm used to generate an ensemble for $p(\lambda_{i+1}|\lambda_i)$ has been shown in the flowchart in Fig. 3.2. Like most path sampling techniques, the shooting move relies on a Metropolis type algorithm whereby an existing sample is modified to generate a new one which is then accepted or rejected according to a probability function that makes sure the ensemble follows the desired distribution. The details of the algorithm can be found in [119] and [13].

The shooting move picks a random time-slice $\boldsymbol{x}_0 = (\boldsymbol{u}, \boldsymbol{v})$ from the previous trajectory and perturbs its velocity, or shoots the system, as follows

$$\boldsymbol{v} = \boldsymbol{v} + \boldsymbol{\delta v} \tag{3.3}$$

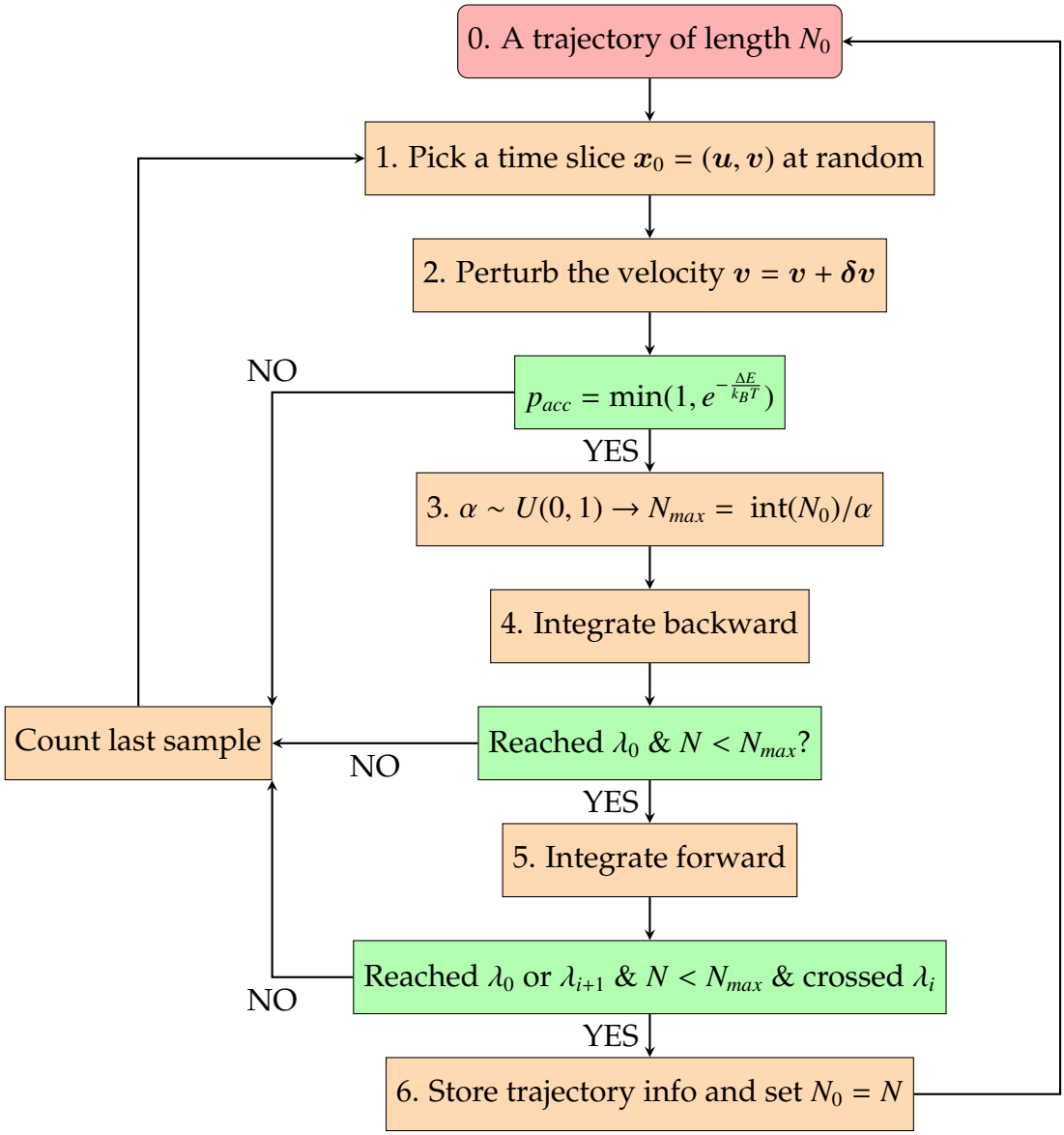

Figure 3.2: The shooting move algorithm. The green boxes are the decisions, the orange boxes are tasks and the red box is the beginning of the algorithm.

This change in velocity changes the (kinetic) energy of the system by ΔE. If the system of interest is at constant temperature, then it can be shown that the acceptance probability

$$p_{acc} = \min\left(1, e^{-\frac{\Delta E}{k_B T}}\right) \tag{3.4}$$

leads the algorithm to generate an ensemble that follows the canonical distribution

$$p(E) = Ce^{-\frac{\Delta E}{k_B T}} \tag{3.5}$$

where E is the energy of the system, T is the temperature, k_B is the Boltzmann constant and C is the normalizing constant [13]. If the change in velocity is accepted, then the equations of motion are integrated backward and forward to generate a trajectory that starts in A and ends in either A or λ_{i+1}, i.e. it belongs to the path ensemble of $p(\lambda_{i+1}|\lambda_i)$. For practical purposes, a maximum trajectory length N_{max} is chosen and backward and forward integrations are stopped in case the trajectory length N exceeds this number. If a trajectory is rejected at any point along the algorithm, the previous trajectory is counted again and another time-slice is picked at random. This gives the appropriate weights to the sample trajectories in the ensemble.

3.3 Parallel Path Swapping

3.3.1 Motivation

Trajectories generated by the shooting move are highly correlated and similar, particularly if they are short . The first, and obvious, consequence of this is slow convergence [118, 11]. If $\delta \boldsymbol{v}$ in Eq 3.3 is too small, then the new trajectories

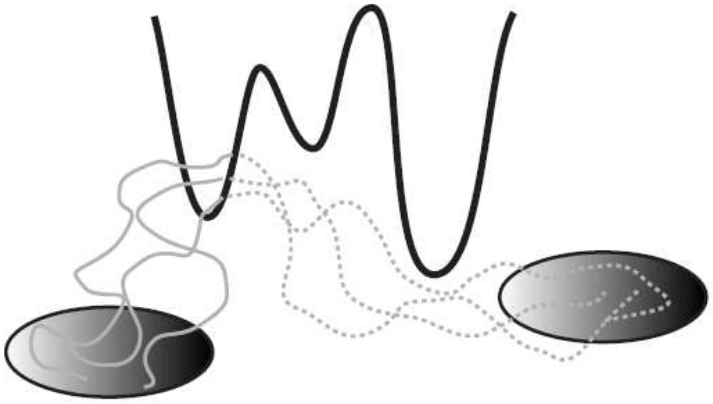

Figure 3.3: A schematic picture of multiple reaction channels. The picture is from [80].

will be very similar. On the other hand, if δv is too large, then the change in energy will be large and the shooting point will be rejected by the acceptance rule Eq. 3.4 [13].

Another issue with the shooting move concerns problems involving more than one reaction channel, i.e. when there are multiple energy barriers separated by higher energy barriers. This has been schematically shown in Fig. 3.3. If the initial trajectory used in the shooting move passes through one of the reaction channels, then the correlation and similarity between trajectories generated by the shooting move might impede generating samples that pass through other reaction channels [118, 11].

These issues spurred the use of path swapping between neighbor interfaces. The idea is schematically shown in Fig. 3.4. The two pictures on the left show two paths belonging to the ensembles of λ_i and λ_j. The path belonging to λ_i also crosses λ_j and the path belonging to λ_j also crosses λ_i, which means the path of each ensemble belongs to the other too and hence the two paths can be swapped like shown in the two pictures on the right. This alleviates the correlation prob-

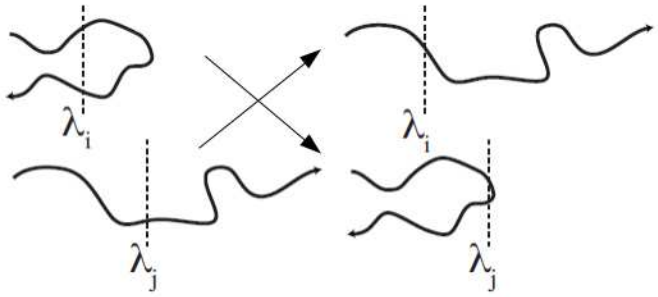

Figure 3.4: Path swapping between two neighbor interfaces. The picture is from [121].

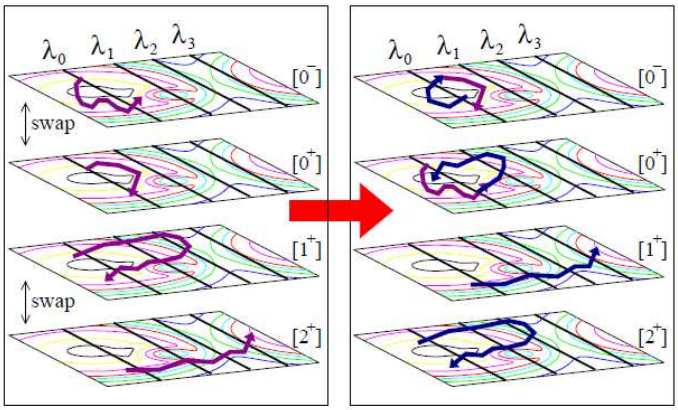

Figure 3.5: The swapped paths between λ_1 and λ_2 have moved to new reaction channels. The picture is from [118].

lem and helps with both convergence and solving problems with multiple reaction channels. The latter has been schematically shown in Fig. 3.5. The lower four pictures show path swapping between λ_1 and λ_2 and the swapped paths have moved to another reaction channels.

3.3.2 Algorithm

Path swapping involves communication between ensembles of two neighbor interfaces. In the existing TIS code, the simulations for computing the terms

in the product of Eq. 3.2 are conducted in parallel such that each term is computed by one processor. In the PSTIS algorithm, a processor in charge of a term exchanges samples with those in charge of the neighboring interfaces [118, 11]. The algorithm followed by each processor is shown in the flowchart in Fig. 3.6.

Whether two neighbors will try to swap trajectories or continue generating new trajectories using the shooting move algorithm is decided at random with equal probability for either case. Moreover, swapped trajectories should not be swapped again. Therefore, two neighbor interfaces can swap only when each of them has generated a new trajectory that belongs to the ensemble of the other one. If any of the trajectories does not belong to the other interface, then the swapping move is rejected and the previous trajectory of each ensemble is counted again [118, 11].

In summary, two neighbors should communicate as follows whenever they both have generated a new trajectory and are ready to swap:

1. The two processors decide whether they want to swap or continue with the shooting point. This is usually decided by one of them and is communicated to the other.
2. Exchange some variables that let each processor decide whether the incoming trajectory belongs to it.
3. Once each processor decided to accept or reject the trajectory offered by the other, one of them sends a flag to the other that reveals its decision.
4. The receiving process communicates the final decision about swapping to the other. Swapping move happens only if it yields a valid path for both ensembles.

5. They swap their trajectories and all the associated information.

3.4 Benchmark Problem

In order to evaluate the accuracy of the parallel implementation of the TIS and the PSTIS algorithms, we consider a benchmark problem for which the average time, i.e. the reciprocal of the rate constant, has been calculated using direct MD simulations. The problem entails the motion of dislocations across obstacles, which is a thermally activated process at moderate loads and temperatures, i.e. a rare event in the atomistic time-scale. The problem is of practical importance in determining and improving the yield strength of alloys. In fact, adding layers of atoms of an alloying metal to the crystalline lattice of a base metal acts like obstacles against the motion of dislocations and hence increases the yield strength of alloys. This strengthening technique is called Precipitation Hardening and is widely used in modern alloys [138].

The benchmark problem is the same as that in Sec. 2.5.1, i.e. the interaction of an edge dislocation in an FCC Al lattice with a monolayer precipitate. The precipitate consists of 13 copper atoms. As shown in Fig.3.7, the simulation box is 6.4 nm ×6 nm ×6 nm. The shear stress is τ_{xy} = 200 MPa and the temperature is T = 300 K.

Table 3.1 shows the average time obtained by TIS and direct MD simulations. TIS slightly underestimates the average transition time. This is a well known fact for such methods that has been proven in the literature [68]. Nevertheless, this level of discrepancy is acceptable for calculating macroscopic strain rate and strain rate sensitivity.

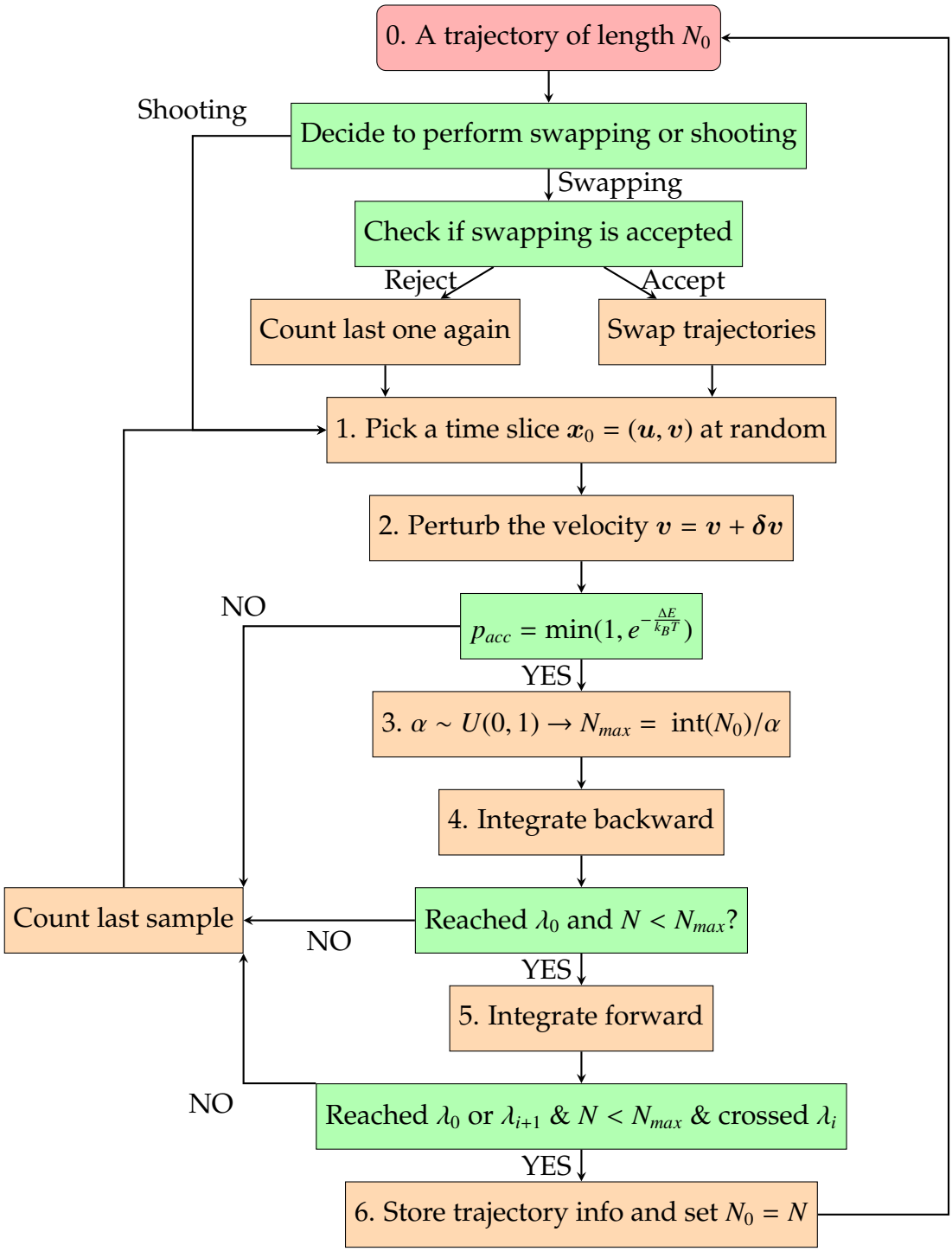

Figure 3.6: The path swapping algorithm. The green boxes are the decisions, the orange boxes are tasks and the red box is the beginning of the algorithm.

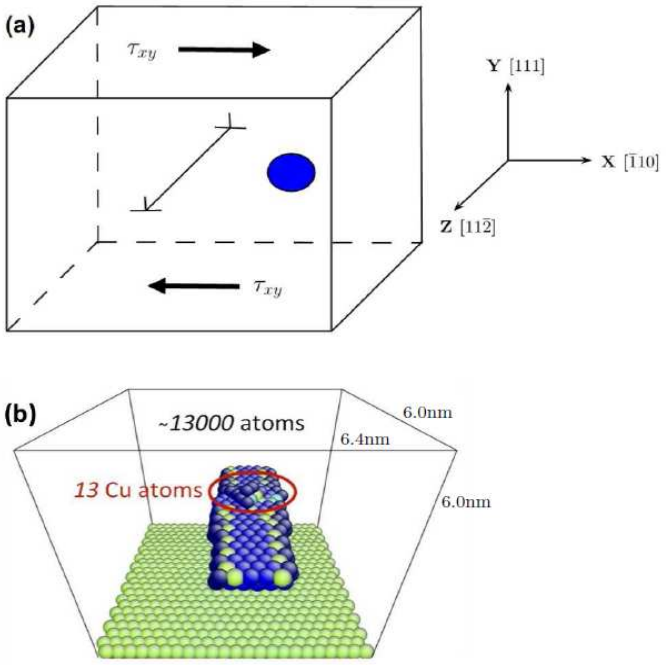

Figure 3.7: Simulation cell with an edge dislocation and a precipitate. (a) Lattice orientation and direction of shear load; (b) The simulation cell configuration at 0K under zero load.

The Finite Temperature String Method, described in [120], is used to find the interfaces for the TIS simulations. The results reported here are based on 21 interfaces. Fig. 3.8 illustrates the initial, final and the center of an intermediate interface. 10 samples with different random seeds were run to calculate each probability $p(\lambda_{i+1}|\lambda_i)$, $i = 0, ..., 20$. $f_A = 1/\bar{t}_A$ has been calculated by starting 50 MD trajectories at A with different initial velocities and measuring the average time $\bar{t}_A$ they take to cross λ_A.

As for direct simulations, 50 samples with different initial velocities were run to compute the average time. Some of the simulations took up to 10 ns until a transition happened, which took approximately a week to run. The TIS simulations, however, took only 3 days. This significant difference in computational cost is an incentive for further research to improve the accuracy of the method.

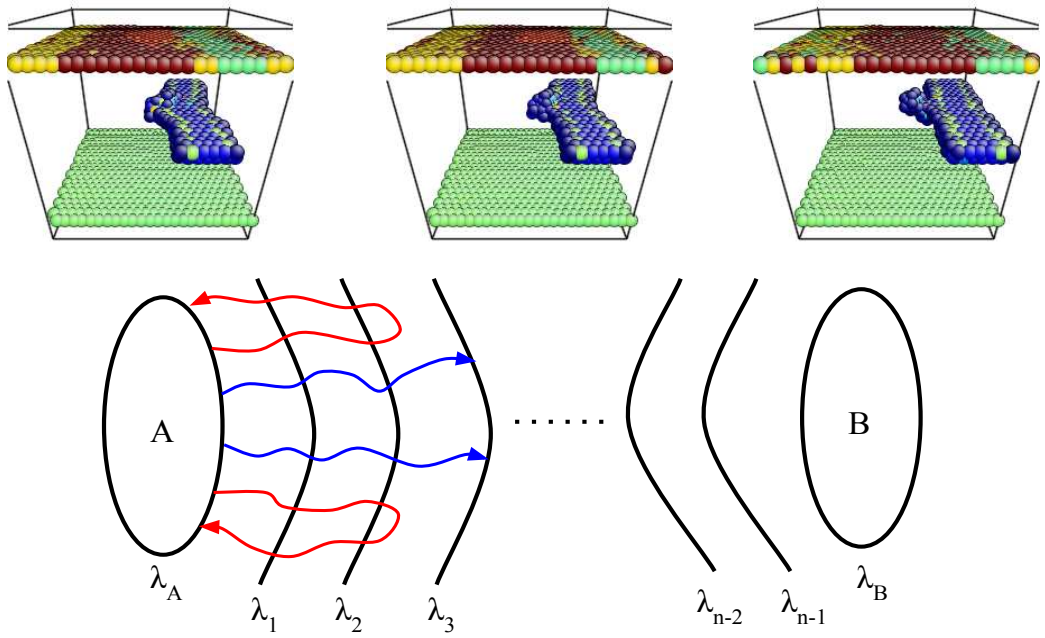

Figure 3.8: The left image is the initial configuration. The right picture is the final configuration and the middle picture is the center of one of the intermediate interfaces.

	Direct MD	TIS
$\bar{t}$	8.99 ns	2.27 ns

Table 3.1: Average transition time $\bar{t}$ computed by TIS and direct simulations.

3.5 Implementation and Efficiency Analysis

3.5.1 Parallelizing TIS

As mentioned before, the first step in implementing the path swapping algorithm is to compute the terms $p(\lambda_{i+1}|\lambda_i)$ in Eq. 3.2 in parallel. This was done using MPI. The rank of each processor is used to determine which ensemble it is responsible for. Once a processor, say rank i, is done, it sends $p(\lambda_{i+1}|\lambda_i)$ to the

processor with rank zero, which computes the product in Eq. 3.2 as it receives the terms from other processors. The implementation was tested by solving the benchmark problem in the previous section using the same interfaces and the same number of samples and time-steps. The outcome was identical to that of the serial code and the average was the same as that in Table 3.1.

All simulations are run for the same number of time steps, although this results in different numbers of samples for different ensembles as they have different average trajectory lengths. Moreover, the computation of each term $p(\lambda_{i+1}|\lambda_i)$ is independent from the others. Therefore, the communication overhead is more or less close to zero.

3.5.2 Pre-Alpha Version: Implementation

The goal of the first version was to implement the algorithm in the most simple, intuitive fashion without optimizing the load balancing and synchronization overhead. In other words, the pre-alpha version is just a working code that solves the problem correctly, following the algorithm shown in Fig 3.6.

The five communication steps mentioned in Section 3.3.2 were implemented using synchronous blocking couples of sends and receives, i.e. MPI_Send and MPI_Recv. This was mostly due to the fact that this communication mode is the easiest to debug and appropriate for developing the first version. The implementation details and their potential impacts on the performance are going to be explained below:

1. Once a processor is done with a shooting cycle, it waits until its neighbor

is also done with its cycle. A synchronous communication occurs at this point entailing the odd rank sending a flag informing the even rank if it has a new trajectory or not.

- This happens even if the waiting processor does not have a new trajectory to swap.
- If either of the two is not ready to swap or if they are ready but the swap is rejected in the 3rd step, the waiting processor has gained/done nothing during this time.

2. Based on the received flag in the previous step, the even processor decides whether the two are ready to swap or not and communicates this decision with the other processor.
3. If the two processors are ready to swap, then the even processor decides whether swapping should be done or not and communicates this decision to the other processor. This is done by generating a uniform random variable in $(0, 1)$ and comparing it with 0.5.
4. If swapping is to be done, then certain variables are exchanged between the two processors so that each processor decides whether the incoming trajectory belongs to its ensemble or not.
5. The odd processor lets the even one know whether it accepts the incoming trajectory or not.
6. The even processor determines whether both processors have accepted their incoming trajectories or not and communicates this with the odd processor.
7. All information about the trajectories is exchanged and the two processors continue to their next round of the shooting move.

	$p(\lambda_1\|\lambda_0)$			$p(\lambda_2\|\lambda_1)$		
Sample	t_{tot}	t_{synch}	t_{com}	t_{tot}	t_{synch}	t_{com}
1	34088.9	4245.3	4246.2	34089.02	26418.1	26418.9
2	34478.7	12011.2	12024.6	34478.7	10880.2	11995.9
3	34992.8	5185.3	5190.4	34992.8	23063.8	23068.9
4	34523.7	9537.6	9541.9	34523.7	17657.9	17662.2
5	34859.8	15348.1	15363.6	34859.8	7615.0	7630.5
6	34954.9	15330.4	15339.6	34954.9	9660.9	9670.1
7	9749.0	755.3	755.3	9749.0	3960.8	3960.8
8	34685.1	11750.8	11757.2	34685.1	16357.4	16363.8
9	34881.5	6248.0	6250.3	34881.5	19088.7	19091.0
10	34906.7	6955.6	6956.4	34906.7	22794.8	22795.7
Sum	322121.1	87367.6	87425.5	322121.2	157497.6	158657.8
t_{com}/t_{tot}	0.27140			0.49254		
t_{synch}/t_{tot}	0.27122			0.48893		
t_{synch}/t_{com}	0.99933			0.99268		

Table 3.2: The total simulation time t_{tot} vs the synchronization time t_{synch} and the communication time t_{com} are shown for 10 samples of the first two interfaces run by the pre-alpha version. The fraction of time spent for communication and synchronization and the fraction of the communication time spent for synchronization are also shown.

3.5.3 Pre-Alpha Version: Analysis

The major fraction of the communication time is the synchronization overhead in the first two steps where any processor that reaches there sooner has to wait for the other one, even if the waiting processor is not ready to swap. Once the two processors are synchronized in the first pair of MPI_Send and MPI_Recv involved in the above first two steps, they incur little synchronization overhead in the remaining steps. That is why it is reasonable to define the time spent in the first pair of MPI_Send and MPI_Recv as the synchronization time t_{synch}. The reason behind this choice will be verified in the analysis below.

Table 3.2 shows the t_{tot} vs the synchronization time t_{synch} and the communication time t_{com} for 10 sample simulations of the $p(\lambda_1|\lambda_0)$ and $p(\lambda_2|\lambda_1)$ ensembles with different seeds. The communication time takes about 30% of the total simulation time and about 100% of the communication time is spent for synchronization. The fact that the fraction of the communication time is large is expected because this version does not allow for any overlap between communication and computation. There are also some unnecessary communications and synchronizations. For instance, a processor has to wait for finding out the status of the other even if it is not ready to swap. The fact that almost the entire communication time goes for synchronization is also aligned with the arguments in the previous paragraph and justifies out definition of t_{synch}.

3.5.4 Alpha Version: Implementation

Having a working code from the previous version, the next step was to improve the efficiency by decreasing the synchronization overhead. The first step is to allow for overlapping communications and computations such that a processor that is ready to swap continues to generate new samples until the other one is ready too. In other words, two interacting processors have to synchronize only if they are both ready to swap trajectories. The key is that the first step in the previous version whereby the two processors inform each other about their status does not have to be done at the end of each shooting move cycle; it could be done in the integration part which is performed way faster by each processor such that this communication step will not suffer from significant synchronization overhead.

	$p(\lambda_1\|\lambda_0)$			$p(\lambda_2\|\lambda_1)$		
Sample	t_{tot}	t_{synch}	t_{com}	t_{tot}	t_{synch}	t_{com}
1	22759.7	1956.9	2197.9	22688.9	5565.7	5734.1
2	22786.7	569.0	995.0	22722.1	1983.9	2286.7
3	22759.6	1808.5	2204.4	22813.0	1202.2	1638.3
4	22671.7	2114.7	2527.9	22492.0	1606.8	2019.7
5	22762.9	2825.2	3181.7	22736.2	1818.0	2051.1
6	22481.3	3253.4	3606.0	22708.3	2511.3	2715.2
7	18979.5	3042.9	3234.4	18911.4	3042.9	3234.4
8	19166.3	497.7	773.8	19271.0	4568.7	4829.5
9	19197.4	365.9	522.8	19179.0	6313.9	6541.4
10	18520.5	2001.8	2399.3	18911.8	2143.7	2408.3
Sum	212085.6	18436	21643.2	212433.7	30757.1	33458.7
t_{com}/t_{tot}	0.10204			0.15750		
t_{synch}/t_{tot}	0.08692			0.14478		
t_{synch}/t_{com}	0.85181			0.91925		

Table 3.3: The total simulation time t_{tot} vs the synchronization time t_{synch} and the communication time t_{com} are shown for 10 samples of the first two interfaces run by the alpha version. The fraction of time spent for communication and synchronization and the fraction of the communication time spent for synchronization are also shown.

The parallelization process can be described as follows:

1. The two processors communicate every time the integration function is called. The odd processor sends its status to the even processor and receives a flag from it indicating whether they are both ready to swap or not. This is done using MPI_Send and MPI_Recv until both processors are ready.

    - Note that the two processors are in a shooting move cycle while getting to know about one another's status.

2. Once both processors are ready, they should decide if a shooting move or a swapping move will be performed. The even processor makes the decision and lets the other one know using MPI_Send and MPI_Recv. This is also done in the integration function.

    - Note that the two processors should not wait for each other unless they know a swapping move should happen. That is why this communication step is also done in the integration routine where there is little synchronization overhead.
    - Note also that this step is only done once every time that the two processors are ready. Therefore, it has little contribution to the total communication time.

3. If swapping is to be done, then certain variables are exchanged between the two processors so that each processor decides whether the incoming trajectory belong to its ensemble or not. This is done using MPI_Send and MPI_Recv.

    - Processors come to know that swapping is to be done while they are in a shooting cycle. The processor that finishes its cycle first has to wait for the other one to be done too so that they can exchange trajectories.

4. The odd processor lets the even one know whether it accepts the incoming trajectory or not.

5. The even processor determines whether both processors have accepted their incoming trajectories or not and communicates this with the odd processor.

- One might wonder why this step is not done in the integration routine too so that no synchronization overhead is incurred unless we are sure swapping moves will be accepted. This idea will be theoretically wrong as there should be no bias as to whether swapping moves are accepted or rejected.

6. All information about the trajectories is exchanged and the two processors continue to their next round of the shooting move.

3.5.5 Alpha Version: Analysis

Table 3.3 shows the t_{tot} vs the synchronization time t_{synch} and the communication time t_{com} for 10 sample simulations of the $p(\lambda_1|\lambda_0)$ and $p(\lambda_2|\lambda_1)$. The samples have the same seeds as those in the previous sections to make the results comparable. As expected, the fraction of the communication time to the total simulation time is smaller compared to the previous version because the Alpha version allows for overlapping communication and computation by allowing a processor to generate more and more samples while waiting for the other processor to generate one.

The fraction of the synchronization time to the communication time has also decreased compared to the previous version. This means data transfer has had a few percents more contribution to the communication time. This initially seems to be a positive fact as it seems processors have spent a few percents more time on doing useful work rather than synchronization. However, this is in fact pointing us to a potential problem which will be explained below.

The increase in the data transfer time is in fact due to having many unneces-

sary communications. Two neighbor processors communicate every time the integration routine is called within a shooting cycle in order to find out if they are ready for swapping trajectories. However, the status of a processor can change only at the end of a cycle when it generates a new trajectory. Therefore, the Alpha version frequently encounters the situation where two neighbors communicate over and over, without the status of either or one of them changes, until they both get ready to swap.

The issue will be more noticeable when the simulation is run for a longer time or when we have more samples because these simply mean more calls to the integration routine. The remedy is going to be described in the next subsection.

3.5.6 Beta Version: Implementation

The Beta version focuses on eliminating the unnecessary communications described in the previous subsection by having two processors communicate their status only when needed, as opposed to in every integration step. The task is done as described in the following. The odd processor sends a message only when it is ready to swap and the even processor uses MPI_Iprobe to post an MPI_Recv only when the message has been sent. Once the two processors are ready, the even processor sends a message and the odd processor uses MPI_Iprobe to post an MPI_Recv only when the message has been sent. This significantly reduces the number of communication occasions compared to having two pairs of sends and receives in each integration step. The details of the parallelization process is as follows:

	$p(\lambda_1\|\lambda_0)$			$p(\lambda_2\|\lambda_1)$		
Sample	t_{tot}	t_{synch}	t_{com}	t_{tot}	t_{synch}	t_{com}
1	22673.5	2597.4	2607.1	22478.4	4249.3	4258.9
2	22373.5	2165.9	2177.7	23125.1	3867.4	3879.1
3	3071.3	1429.1	1451.0	23022.7	4278.5	4300.4
4	23100.9	1880.7	1905.4	22879.8	2119.7	2144.4
5	23107.6	1175.5	1179.2	23083.2	3956.0	3959.6
6	19355.3	1010.2	1021.6	19422.3	3624.0	3635.3
7	19240.4	1227.7	1231.2	19313.2	5282.5	5285.9
8	19490.5	2547.8	2566.2	19489.0	1503.6	1522.0
9	18939.7	393.5	395.6	18930.6	6201.2	6203.4
10	18880.1	1110.2	1124.4	19472.7	2702.4	2716.6
Sum	190232.8	15538	15659.4	211217	37784.6	37905.6
t_{com}/t_{tot}	0.08231			0.17946		
t_{synch}/t_{tot}	0.08167			0.17888		
t_{synch}/t_{com}	0.99224			0.99680		

Table 3.4: The total simulation time t_{tot} vs the synchronization time t_{synch} and the communication time t_{com} are shown for 10 samples of the first two interfaces run by the beta version. The fraction of time spent for communication and synchronization and the fraction of the communication time spent for synchronization are also shown.

1. The odd processor sends a message at the end of the shooting cycle when it has a new trajectory to swap. This is done using MPI_Send which acts like MPI_Bsend as the message is just an integer flag.

2. The even processor always checks if the above message is coming using MPI_Iprobe that is called in the integration routine. If MPI_Iprobe shows that the message has been sent, then even processor receives it using MPI_Recv.

    - The received message sets a flag to 1 indicating that the odd processor is ready. If no message is received the flag has a default value of 0.

- The even processor has also a flag of its own indicating its status.

3. As soon as the two flags on the even processor are set to 1, it sends a message to the odd processor indicating they are both ready to swap.
4. The odd processor always checks if the above message is coming using MPI_Iprobe. If MPI_Iprobe shows that the message has been sent, then an MPI_Recv is called to receive it.
5. Once the two processors realize that they are both ready to swap, the remaining steps will be identical to those in 2 through 7 of the alpha version.

3.5.7 Beta Version: Analysis

The Beta version is expected to have smaller communication time compared to the previous version. This is because the communication step where two processors find out about each other's status is done only when necessary, i.e. when the odd processor has a new trajectory to swap or when both processors are ready to swap trajectories. Hence, the two pairs of MPI_Send and MPI_Recv used for this communication step are called at most a few times in every shooting cycle. This should impose less communication overhead compared to the previous version where the two pairs are called in every integration step, specially when the code is run for long times, e.g. more than 10^6 time steps.

Table 3.4 shows the t_{tot} vs the synchronization time t_{synch} and the communication time t_{com} for 10 sample simulations of the $p(\lambda_1|\lambda_0)$ and $p(\lambda_2|\lambda_1)$. In order for the results to be comparable with those in the previous two sections, the samples used the same random number seeds. As expected, synchronization

comprises almost 100% of the communication time, which shows the unnecessary communications have been eliminated.

The total communication time for the first ensemble has decreased almost 50%, but it has not changed much for the second ensemble. Both of these are due to the statistical error stemming from having few samples and a short simulation time. As mentioned in Section 3.5.5, the overhead associated with the excessive communications is small at the considered simulation time (about 2%). Hence, we expect a slight decrease in the mean communication time at short simulation times like in this case. This small change in the mean can easily be hidden by the statistical error.

In response to the above arguments, one might argue the statistical error should not hide the decrease in the overhead because the Alpha and Beta versions have essentially the same algorithm and hence generate the same trajectories if started with the same seed; If the same trajectories are generated and swapping happens at the same times, then the Beta version has fewer number of communications and hence should have a smaller communication time. This argument is not right though as will be explained below.

The samples run by the two versions do not necessarily result in the same trajectories, even though they are started with the same random seed and they follow the same. This is because of the fact that samples are run on different processors and nodes with different work loads. Remember that swapping happens only when both processors are ready and a processor might generate a few new trajectories while the other one is working on one. The number of new trajectories on the first processor depends on how much time the second processor takes to generate one. Given a seed, this time is constant in terms of process-

	Direct MD	Parallel TIS	Path Swapping TIS
$\bar{t}$	8.99 ns	2.27 ns	3.8 ns

Table 3.5: Comparison between the average transition time $\bar{t}$ computed by TIS, path swapping TIS and direct simulations.

ing cycles but the clock time varies depending on the work load of the node and other architecture variables. That is why two runs of the same code or the two versions of the code on different nodes and processors might lead to different trajectories being swapped which results in the simulations continuing differently. Thereby, we can only compare the performance of the two versions statistically and not sample by sample.

3.5.8 Beta Version: Comparison with TIS

In order to make sure that the implementation is right and also show the merit of the path swapping technique in reducing the correlation between samples, the Beta version was used to solve the benchmark problem in Section 3.4. The same interfaces as those used to solve the problem with TIS are utilized. 5 samples with different seeds were run for 10^6 time steps to calculate the probabilities, which is 50% less than the number of samples used for TIS. Table 3.5 shows the obtained average time in comparison to those of TIS and direct MD simulations. The average time obtained by path swapping is more than 1ns closer to the actual value compared to that of TIS, which verifies the theory behind the method.

3.6 Future Work

3.6.1 Implementation

The Beta version still has a fairly large synchronization overhead, which it inherits from the Alpha version. The two versions mainly focused on eliminating the communication and synchronization overhead associated with the decision process about a swapping move. The remaining overhead is entirely due to the fact that the trajectory exchange process, steps 2-7 of the Alpha version, is done in a synchronous manner in the beginning of the shooting cycle. Processors come to know that they are both ready to swap while they are in their shooting cycles and the processor that finishes its cycle first has to wait for the other one to be done too so they can swap their trajectories.

This restriction can be released by moving the trajectory exchange process inside the shooting cycle where there is little synchronization overhead thanks to the fast nature of the tasks. Hence, processors will exchange their trajectories immediately when they are both ready. Then, each processor will start using the incoming trajectory in its next cycle without having to wait for the other one to be done with its cycle.

Another restriction of the Beta version is that only interactions of the kind $\lambda_0 \leftrightarrow \lambda_1$, $\lambda_2 \leftrightarrow \lambda_3$, $\lambda_4 \leftrightarrow \lambda_5, ...$ are considered, i.e. even numbered interfaces interact with their next odd numbered interface. The code eventually should be able to handle interactions of the kind $\lambda_1 \leftrightarrow \lambda_2, \lambda_3 \leftrightarrow \lambda_4, \lambda_5 \leftrightarrow \lambda_6, ...$ and it should be able to switch between the two cases randomly.

3.6.2 Timing Analyses

The following are some of the limitations of the above timing analysis and some possible tasks to be done in the future:

1. The timing analyses, specially for the Beta version, should be done with more samples and longer simulations times. As explained in Section 3.5.7, performance comparison between two versions has to be done statistically. Ideally, distributions of different elements of the simulation time should be compared across different versions. For this project, only comparison between the expected values would probably suffice though as performance changes from a version to another are somehow predictable.
2. Timing analysis was done only for the interaction of the first two interfaces. The synchronization overhead involved in the Beta version depends on the average trajectory length, i.e. the number of time steps spent in a shooting cycle. Hence, the overhead would vary for interfaces farther from the stable state A. Ideally, the overhead distribution of all trajectories should be studied in order to find possible bottlenecks.

CHAPTER 4

INVESTIGATING DISLOCATION MOTION THROUGH A FIELD OF SOLUTES WITH ATOMISTIC SIMULATIONS AND REACTION RATE THEORY

By S. Saroukhani, D. Warner

As submitted to Acta Materiala

4.1 Abstract

The rate of thermally activated dislocation motion across a field of solutes is studied using traditional and modern atomistically informed rate theories. First, the accuracy of popular variants of the Harmonic Transition State Theory, as the most common approach, is examined by comparing predictions to direct MD simulations. It is shown that HTST predictions are grossly inaccurate due to the anharmonic effect of thermal softening. Next, the utility of the Transition Interface Sampling was examined as the method was recently shown to be effective for predicting the rate of dislocation-precipitate interactions. For dislocation-solute interactions studied here, TIS is found to be accurate only when the dislocation overcomes multiple obstacles at a time, i.e. jerky motion, and it is inaccurate in the unpinning regime where the energy barrier is of diffusive nature. It is then shown that the Partial Path TIS method - designed for diffusive barriers - provides accurate predictions in the unpinning regime. The two methods are then used to study the temperature and load dependence of the rate. It is shown that Meyer-Neldel (MN) rule prediction of the entropy barrier is not as accurate as it is in the case of dislocation-precipitate interactions. In response, an alternative model is proposed that provides an accurate pre-

diction of the entropy barrier. This model can be combined with TST to offer an attractively simple rate prediction approach. Lastly, (PP)TIS is used to predict the Strain Rate Sensitivity (SRS) factor at experimental strain rates and the predictions are compared to experimental values.

4.2 Introduction

Dislocation-obstacle interactions have been studied extensively using continuum and atomistic models. Recent studies reveal that predicting quantities of interest, such as the rate at which dislocations overcome obstacles, can be highly dependent on the nanoscale details of dislocation-obstacle interactions [109, 108]. Thus, using atomistic simulations to study these interactions is ideal. A key challenge is that dislocation motion across obstacles is thermally activated under ordinary laboratory conditions and hence can be rare in the time-scale accessible to atomistic models. That is why atomistic studies are often conducted at high loads and temperatures, which can lead to both qualitative and quantitative differences compared to ordinary experiments [87]. Therefore, there is considerable motivation to develop and apply atomisitc modeling techniques capable of studying dislocation-obstacle interactions at experimental time-scales.

Harmonic Transition State Theory (HTST) is a common approach to compute the rate of thermally activated events. The method has been used extensively to study dislocations in metals. The method is based on the assumption that the potential energy surface is quadratic near the initial and saddle states of the system. This assumption amounts to assuming temperature indepen-

dent material properties and approximating the activation entropy with the vibrational entropy [127], two approximations often believed to be accurate for solids [128, 36]. HTST provides a rate expression of the Arrhenius form that involves the activation potential energy and a pre-exponential factor. The activation potential energy can be computed using minimum energy path techniques such as the 0K string method [133]. The pre-exponential factor involves natural frequencies of the system at the initial and saddle configurations and hence requires solving two eigenvalue problems.

The eigenvalue problems are often avoided as they are intractable for all but the smallest model sizes. A common approach is to assume that the entropy barrier is zero by setting the pre-exponential factor equal to the normal frequency along the reaction coordinate at the initial configuration [54]. Other approximations commonly used include the imaginary frequency of the saddle configuration [99] and the Debye frequency. We will refer to these approaches as Simplified HTST.

Recent studies have revealed that the assumptions behind HTST and SHTST are not universally applicable for predicting reaction rates in solids. An example is [104] which shows that HTST based approaches fail to predict the rate of dislocation-precipitate interactions in Al-Cu alloys as they neglect the anharmonic effect of thermal softening. Another example is the dislocation nucleation rate, which has been shown to have a large entropy barrier as a result of anharmonic effects. In the latter example, other methods such as Parallel Replica Dynamics (PRD) [131], Hyperdynamics [54], and Transition State Theory [86, 103] have been applied successfully. These methods, however, are known to have certain restrictions. For instance, TST requires the free energy

profile along a well-defined reaction coordinate, which can be difficult to obtain for dislocation-obstacle interactions even using powerful techniques such as the Finite Temperature String Method [124, 104]. PRD is suitable for problems with high rates and small activation volumes as it provides a speedup that scales with the number of available replicas. Finally, Hyperdynamics makes use of an artificial potential that is hard to design and application specific.

To address the lack of generality in the above methods, the biophysics and chemistry communities have developed and applied Path Sampling techniques [44]. These methods are more general in the sense that they do not assume prior knowledge about the transition such as a carefully defined reaction coordinate or transition state. Path Sampling techniques are based on the idea that a transition is fully characterized by the Transition Path Ensemble (TPE) and hence the information needed to predict all transition features such as reaction coordinate(s), rate(s), free energy profie(s) and mechanism(s) can be gathered by sampling the TPE [90, 34]. Comprehensive reviews of such methods can be found in [44, 32]. However, these methods have not attracted much attention in the mechanics of materials community, despite their numerous potential applications. The first application in this field was [104] where a TPE method known as Transition Interface Sampling (TIS) [119] was shown to accurately predict the rate at which dislocations overcome precipitates.

In this chapter, we study the rate at which dislocations overcome a field of solutes using HTST, TIS and Partial Path TIS — a variant of TIS designed for diffusive barriers [81]. The chapter begins with a brief description of the theoretical background of each method in Section 4.3. In Section 4.4, the details of the atomistic simulations are explained. In Section 4.5.1, HTST, TIS and PPTIS pre-

dictions are compared to those of direct MD simulations for a few benchmark problems. The validity of the harmonic approximation and several models for predicting the entropy barrier are discussed in Section 4.5.2. The strain rate sensitivity factor is computed and compared to experimental values and other models in the literature in Section 4.5.3. In the final section, the conclusions are summarized and potential future directions are discussed.

4.3 Methods

4.3.1 Transition State Theory

Transition State Theory (TST) provides an exact expression for the rate at which an ergodic system crosses a dividing surface, S_D, partitioning the configuration space into two sets a and b:

$$k_{ab}[S_D] = \sqrt{\frac{k_B T}{2m\pi}} \frac{Z_{S_D}}{Z_a} \tag{4.1}$$

with k_B being the Boltzmann constant, T the temperature, m the effective mass, $Z_{S_D} = \int_{S_D} e^{-\frac{V(\mathbf{x})}{k_B T}} d\sigma(\mathbf{x})$ and $Z_a = \int_a e^{-\frac{V(\mathbf{x})}{k_B T}} d\mathbf{x}$ the constrained partition functions associated with S_D and a respectively. The term $\sqrt{\frac{k_B T}{2m\pi}}$ is the flux through the dividing surface and $\frac{Z_{S_D}}{Z_a}$ represents the probability of the system being on S_D relative to a [15]. Often, a surface, S_0, which does not intersect S_D and contains an initial configuration in a, is defined to express Eq. 4.1 in terms of a free energy barrier [127]:

$$k_{ab}[S_D] = \tilde{\nu} e^{-\frac{\Delta F}{k_B T}} \tag{4.2}$$

where

$$\tilde{\nu} = \sqrt{\frac{k_B T}{2m\pi}} Z_a^{-1} \int_{S_0} e^{-\frac{V(\mathbf{x})}{k_B T}} d\sigma(\mathbf{x}) \tag{4.3}$$

and the free energy barrier is

$$\Delta F = F_{S_D} - F_{S_0} = -k_B T \ln \left(\frac{\int_{S_D} e^{-\frac{V(\mathbf{x})}{k_B T}} d\sigma(\mathbf{x})}{\int_{S_0} e^{-\frac{V(\mathbf{x})}{k_B T}} d\sigma(\mathbf{x})} \right) \tag{4.4}$$

which can also be written as

$$\Delta F(\sigma, T) = \Delta U(\sigma, T) - T\Delta S(\sigma, T) \tag{4.5}$$

with $\Delta U(\sigma, T)$ being the activation internal energy and $\Delta S(\sigma, T)$ the activation entropy.

One challenge in computing the rate from Eq. 4.2 is that one is often interested in the transition rate between two metastable regions $A \subset a$ and $B \subset b$ that do not necessarily partition the phase space and hence a transition cannot be exactly characterized by crossing a hypersurface. In such cases, the TST rate formula, Eq. 4.2, can overestimate the actual rate of interest, i.e.

$$k_{AB} \leq k_{ab}[S_D] \tag{4.6}$$

The demanding task of computing a free energy profile in Eq. 4.2 motivates the Harmonic TST (HTST) approach, which assumes that the potential energy surface is quadratic at the initial and saddle configurations. This assumption equates to temperature independent material properties and is widely used for problems involving solids. The method further assumes that the dividing surface corresponds to a potential energy ridge, S_D^V, between A and B to express the transition rate as

$$k_{AB} \approx \left(\frac{\prod_{i=1}^{3N} \nu_i^{\text{initial}}}{\prod_{i=1}^{3N-1} \nu_i^{\text{saddle}}} \right) e^{-\frac{\Delta V}{k_B T}} = \nu_0 e^{-\frac{\Delta V}{k_B T}} \tag{4.7}$$

where ν_i^{initial} and ν_i^{saddle} are respectively the normal frequencies of the system in the initial and saddle configurations. The product over the saddle point frequencies excludes the imaginary frequency in the direction of the reaction coordinate, i.e. normal to S_D^V, and hence all frequencies are real. N is the number of atoms in the system and ΔV is the difference in the potential energy between the saddle and initial configurations.

Solving the two eigenvalue problems required for Eq. 4.7 becomes prohibitively expensive for large systems. That is why Eq. 4.7 is sometimes further simplified by assuming that the prefactor is equal to the normal frequency, ν_*^{initial}, in the direction of the reaction coordinate in the initial state: $k_{AB} \approx \nu_*^{\text{initial}} e^{-\frac{\Delta V}{k_B T}}$. We will refer to this approach as the Simplified HTST (SHTST). Other choices for the pre-factor such as the imaginary frequency of the saddle point and the Debye frequency have also been used in the literature [54, 99].

4.3.2 Finite Temperature String Method

FTS is an algorithm for finding a reaction coordinate and computing the free energy profile along the coordinate. It has been extensively used with TST to predict reaction rates [87, 86, 98]. The method utilizes the idea of reaction tubes, a relatively high probability region in configuration space that links A and B. Assuming that reaction tubes are thin and isolated, the method offers an algorithm for finding iso-committer surfaces, i.e. surfaces where the probability that a trajectory reaches B before A is uniform, and the expected configuration on each of them. A reaction coordinate is then defined as a curve (string) connecting the expected configurations.

The algorithm starts with an initial string connecting the initial and final states through a set of equally spaced intermediate configurations (images) and a set of Voronoi cells centered at the images. Constrained sampling at constant temperature is performed within each cell and the time averaged position associated with each cell is computed. Then, the time averaged positions are used to update the string and Voronoi cells, while satisfying a smoothing condition and enforcing equal distance between images. Iterating over this process leads to a converged string and its associated Voronoi cells. The Voronoi cells approximate the iso-committer surfaces and the images approximate the expected configuration within them. The quality of the approximation depends on the discretization error and the sampling error. We refer the interested reader to Refs. [98, 124] for further details on the theoretical background of the method.

4.3.3 Transition Interface Sampling

Like TST based approaches, TIS aims to calculate a flux, but it does not require a transition state to be identified *a-priori*, nor does it require a carefully chosen reaction coordinate and the computation of the free energy profile along the coordinate [119]. These advantages stem from the method directly calculating the rate using actual trajectories of the system, i.e. samples of the Transition Path Ensemble (TPE). TIS measures the flux through a set of hypersurfaces partitioning phase space rather than a single dividing surface, which can be hard to define. The TIS method is based on the *effective positive flux* formalism [15] which makes it less sensitive to recrossings.

The first step in TIS is to partition phase space using a set of $n + 1$ non-

intersecting interfaces, defined as level sets, λ_i, of an order parameter, $\lambda(\mathbf{x})$, i.e. $\{\mathbf{x}|\lambda(\mathbf{x}) = \lambda_i\}$, $i = 0, ..n$. The order parameter, $\lambda(\mathbf{x})$, does not have to be associated with a properly chosen reaction coordinate; it is sufficient that $\lambda(\mathbf{x})$ characterizes the basins of attraction of A and B [119]. As schematically shown in Fig. 4.1, each interface, λ_i, is closer to A than the next interface, λ_{i+1}, such that $\lambda_0 = \lambda_A$ defines the boundary of the basin of attraction of A and $\lambda_n = \lambda_B$ defines that of B.

TIS makes use of the *effective positive flux* formalism to express the transition rate as

$$k_{AB} = \frac{\langle \phi_{\lambda_0,\lambda_n} \rangle}{\langle h_{\mathcal{A}} \rangle} \tag{4.8}$$

where $h_{\mathcal{A}}$ is the indicator function and $\phi_{\lambda_0,\lambda_n}$ is the *effective positive flux* from state A through interface λ_n [119]. $\mathcal{A}$ is the set of all phase points where the corresponding trajectories come from A without having visited B. A transition happens when the system leaves $\mathcal{A}$, i.e. when the system enters B for the first time. The denominator, $\langle h_{\mathcal{A}} \rangle$, is the fraction of time the system spends in $\mathcal{A}$. Therefore, Eq. 4.8 is the exact definition of rate, which is the number of *effective* transitions from A to B divided by the total time the system spends in $\mathcal{A}$, in the limit of time going to infinity. It is also worth noting that the equation is equivalent to the TST rate formula when $S_D = \lambda_A = \lambda_B$, i.e. when the transition is characterized by crossing a single dividing surface.

Calculating the rate from Eq. 4.8 is not feasible as it requires simulations that are long enough to capture a rare transition. To overcome this challenge, TIS relates the flux through an interface, λ_i, to that of the previous interface, λ_{i-1}, using the recursive formula

$$\langle \phi_{\lambda_0,\lambda_i} \rangle = \langle \phi_{\lambda_0,\lambda_{i-1}} \rangle P(\lambda_i|\lambda_{i-1}) \tag{4.9}$$

where $P(\lambda_i|\lambda_{i-1})$ is the probability that a trajectory, coming from A, crosses λ_i

provided that it has already crossed λ_{i-1} [119]. For instance in Fig. 4.1, $P(\lambda_2|\lambda_1)$ is the fraction of blue trajectories to the red and blue trajectories. In simpler words, this equation relates the flux through two neighboring interfaces by using the fact that only a fraction of trajectories that cross λ_{i-1} make it to λ_i before going back to A. That fraction is the probability $P(\lambda_i|\lambda_{i-1})$. The recursive formula in Eq. 4.9 is used to express $\langle \phi_{\lambda_0,\lambda_n} \rangle$ as

$$\langle \phi_{\lambda_0,\lambda_n} \rangle = \langle \phi_{\lambda_0,\lambda_1} \rangle \prod_{i=1}^{n-1} P(\lambda_{i+1}|\lambda_i) \tag{4.10}$$

and hence rewrite Eq. 4.8 as

$$k_{AB} = \frac{\langle \phi_{\lambda_0,\lambda_1} \rangle}{\langle h_{\mathcal{A}} \rangle} \prod_{i=1}^{n-1} P(\lambda_{i+1}|\lambda_i) \tag{4.11}$$

where the term $\frac{\langle \phi_{\lambda_0,\lambda_1} \rangle}{\langle h_{\mathcal{A}} \rangle}$ is the rate of transition from λ_0 to λ_1, which can be computed using direct MD simulations.

The trajectories needed for calculating the probabilities $P(\lambda_{i+1}|\lambda_i)$ cannot be generated using direct simulations for interfaces that are far from A. A method commonly used for this purpose in the TIS literature is the so-called 'shooting move', which is a Metropolis Markov Chain Monte Carlo (MCMC) algorithm. The theoretical and algorithmic details of the method can be found in [119] and the references therein. The algorithm ensures generating samples from the Boltzmann distribution by satisfying the detailed balance equation and using the Boltzmann distribution for deriving the acceptance rule.

4.3.4 Partial Path TIS

PPTIS is based on the assumption that, for diffusive barriers, trajectories lose their memory over a distance shorter than the interface separations. Consider

the schematic diffusive barrier shown in Fig. 4.1. One can assume that the system spends enough time in each metastable state to lose its memory before hopping to a neighboring metastable state. This means that the probability of transition to a neighboring state is independent of the history of the path. In other words, the system behaves like a Markov Chain whose state space consists of the metastable states. As will be explained, these assumptions allow the TIS rate formula, Eq. 4.11, to be rewritten such that substantially shorter trajectories are needed to compute the rate. We refer the interested reader to [81] for further details on the theoretical background and derivations of the method.

Let us define the long distance crossing probability, P_j^+, as the probability that, once the system crossed λ_1, it moves forward to cross interface λ_j before going back to the initial state. Based on the TIS rate formula, Eq. 4.11, P_j^+ is equal to $\prod_{i=1}^{j-1} P(\lambda_{i+1}|\lambda_i)$, which means trajectories connecting the initial state to λ_{i+1} are needed for each $i = 0...j-1$. Based on this definition, the TIS formula, Eq. 4.11, can be written as

$$k_{AB} = \frac{\langle \phi_{\lambda_0,\lambda_1} \rangle}{\langle h_{\mathcal{A}} \rangle} P_n^+ \tag{4.12}$$

The Markovian assumption in PPTIS allows P_j^+ to be rewritten as

$$P_j^+ = \frac{p_{j-1}^{\pm} P_{j-1}^+}{p_{j-1}^{\pm} + p_{j-1}^{=} P_{j-1}^-} \tag{4.13}$$

where

$$P_j^- = \frac{p_{j-1}^{\mp} P_{j-1}^-}{p_{j-1}^{\pm} + p_{j-1}^{=} P_{j-1}^-} \tag{4.14}$$

As seen in the following, $p_i^{\pm}$ and $p_i^{\mp}$, $p_i^{=}$ can be computed by generating trajectories that connect three neighboring interfaces of λ_{i-1}, λ_i and λ_{i+1}.

Let us define $P\left(\begin{matrix} l \\ m \end{matrix} \middle| \begin{matrix} i \\ j \end{matrix}\right)$ as the probability that a trajectory reaches interface λ_l before λ_m under the condition that it crossed λ_i at t = 0, while coming directly

from interface j in the past. A schematic trajectory fitting this description has been shown in Fig. 4.1. Based on this definition, $p_i^{\pm}$, $p_i^{\mp}$, $p_i^{=}$ and $p_i^{\ddagger}$ are expressed as

$$p_i^{\pm} \equiv P\left(i \overset{i+1}{-} 1 \middle| i \overset{i}{-} 1\right) \qquad p_i^{\mp} \equiv P\left(i \overset{i-1}{+} 1 \middle| i \overset{i}{+} 1\right) \tag{4.15}$$

$$p_i^{=} \equiv P\left(i \overset{i-1}{+} 1 \middle| i \overset{i}{-} 1\right) \qquad p_i^{\ddagger} \equiv P\left(i \overset{i+1}{-} 1 \middle| i \overset{i}{+} 1\right) \tag{4.16}$$

These are the hopping probabilities of the Markov Chain which fulfill the following relation:

$$p_i^{\pm} + p_i^{=} = p_i^{\mp} + p_i^{\ddagger} = 1 \tag{4.17}$$

Therefore, it is enough to compute $p_i^{\pm}$ and $p_i^{\mp}$ by generating trajectories that start at λ_{i-1} or λ_{i+1} and end by crossing either λ_{i-1} or λ_{i+1} and cross λ_i at least once. Such trajectories can be generated using the shooting move explained in the previous subsection.

4.4 Simulation Details

The atomistic simulations were conducted using a modified version of the LAMMPS package. The EAM Al-Mg potential of [74] was used, which is based on the aluminum potential of [42] and the magnesium potential of [73]. This potential has been used extensively to study Al-Mg alloys in the literature [31, 88]. The simulation cell was bounded by $(1\bar{1}0)$, (111), and $(\bar{1}\bar{1}2)$ faces in the X, Y, and Z directions, respectively (Fig. 4.1). The cell dimensions are $72 \times 55 \times 60$ nm. Starting with a perfect FCC Al lattice, an edge dislocation was created with a line direction parallel to the Z-axis and $\boldsymbol{b} = 1/2[\bar{1}10]$. Then, 5% of the Al atoms were randomly selected and replaced by Mg atoms. Periodic boundary

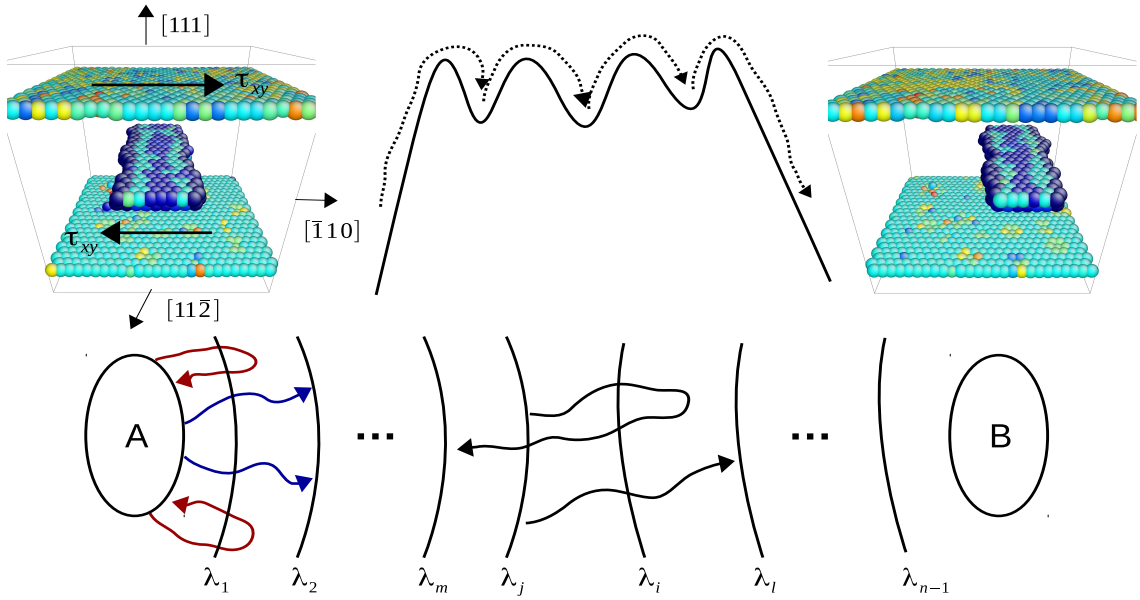

Figure 4.1: Bottom: A schematic picture of the interfaces and trajectories involved in (PP)TIS calculations. The blue and red trajectories are TIS trajectories and the black trajectories are in the $P\left(\begin{matrix} l \\ m \end{matrix}\middle|\begin{matrix} i \\ j \end{matrix}\right)$ ensemble (Sec. 4.3). Top left: The initial configuration at $\tau_{xy} = 20$ MPa and T = 300K. Only atoms not in a perfect FCC stacking, i.e. having a large centro-symmetry parameter, are shown [70]. Top right: the final configuration. Top center: a schematic diffusive barrier.

conditions were applied in the X and Z directions. The system was loaded by applying the shear forces

$$f_{top} = \frac{\tau_{xy} A_{xz}}{N_{top}}, \qquad f_{bottom} = -\frac{\tau_{xy} A_{xz}}{N_{bottom}} \tag{4.18}$$

on the atoms near the top and bottom Y surfaces.

The dislocation length and the initial and final configurations were chosen based on arguments presented in [88] and [31]. In those works, Labusch's model [67] and atomistic simulations were used to determine the length at which the dislocation remains straight at moderate loads and temperatures, avoiding complex dislocation geometries and energy landscapes at extremely

low loads/high temperatures. Based on the given dimensions, our predictions of critical parameters for this analysis were close to those obtained in the literature, e.g. the Peierls stress, the critical resolved shear stress (CRSS), the activation potential energy and activation free energy under zero stress [88, 110, 111]. The procedure for choosing the initial and final configurations has been described in the supplementary material.

The HTST rate expression, Eq.4.7, involves the potential energy barrier that is computed using the 0K string method [133]. The FTS method is used to obtain the interfaces used in (PP)TIS. Both versions of the string method require an initial string connecting the initial and final configurations through a set of intermediate ones. This string has been generated by interpolation between the initial and final configurations using the Euclidean norm.

The set of interfaces for (PP)TIS was simply defined as the boundaries between Voronoi cells of the convergent string given by the first step in the FTS method. The string was also used as the initial trajectory needed to start the shooting move for the (PP)TIS approach.The simulations to compute $P_A(\lambda_{i+1}|\lambda_i)$, $p_i^{\pm}$ and $p_i^{\mp}$ for each λ_i were performed in parallel. For each λ_i, five to twelve 1 ns simulations, started with different seeds, were performed. The transition flux through the first interface, $\frac{\langle \phi_{\lambda_0,\lambda_1} \rangle}{\langle h_{\mathcal{A}} \rangle}$, was calculated using 50 independent direct MD simulations started with different seeds.

4.5 Results and discussion

Before discussing the simulations results, it is helpful to mention some items associated with the motion of dislocation through solutes fields. At high

loads/low temperatures, dislocation motion is expected to be in the jerky regime, where the dislocation overcomes multiple obstacles at a time in a correlated manner. In this regime, the free energy profile is expected to have a single barrier, similar to the potential energy profile [91]. At low loads/high temperatures, on the other hand, the dislocation motion is expected to be in the (smooth) unpinning regime where the dislocation overcomes one obstacle at a time. In this case, the free energy profile is of diffusive nature similar to the schematic profile shown in Figure 4.1 [91]. The two regimes have been discussed in other computational and experimental studies [138, 91, 135, 136, 69].

While a free energy profile along the reaction coordinate is required to clearly demonstrate these concepts, computing the free energy profile is a daunting task for problems such as this, and to the best of our knowledge has not been done before. Even a powerful a tool such as FTS will typically fail to provide an accurate free energy profile for problems with simpler energy landscapes such as dislocation-precipitate interactions because some of the method's assumptions are not fulfilled. We refer the interested reader to [104] for more detail. Avoiding such complexities in free energy calculations is one of the key features of direct rate theories, such as (PP)TIS, because they can compute the rate using actual trajectories of the system, without requiring a free energy profile or an accurate reaction coordinate.

Therefore, we first show in Section. 4.5.1 that TIS provides accurate predictions relative to MD simulations when the motion is expected to be in the jerky regime and PPTIS does so when the motion is expected to be in the smooth regime. Once the accuracy of (PP)TIS is established, the two methods and direct MD simulations are used to study the temperature and load dependence of the

Method	T = 300K	T = 333K	T = 353K	T = 373K
Direct MD	66	9.5	6.0	1.1
PPTIS	11	1.7	4.2	1.0
TIS	59	8.9	84.6	132
HTST	1×10^4	1.6×10^3	593	250
SHTST	7.3×10^5	1.1×10^5	4.2×10^4	1.8×10^4

Table 4.1: The predictions of the methods described in Sec. 4.3 for the average time, $\bar{t}$, in nanoseconds, for an edge dislocation to overcome an a field of solutes. All the predictions are in nanoseconds and have been obtained at τ = 20MPa.

rate in Section. 4.5.2 and 4.5.3, respectively.

4.5.1 Comparison of the methods

As mentioned before, the quantity of interest in this paper is the average time for a dislocation to move across a field of solutes from one equilibrium configuration to the next, i.e. $\bar{t} = k_{AB}^{-1}$. We examine the performance of the methods described in Sec. 4.3 by comparing their predictions to benchmarks obtained by direct MD simulations at τ_{xy} = 20MPa and four different temperatures, i.e. T = 300K, 333K, 353K and 373K (Table. 4.1). Four temperatures are considered because, as discussed earlier, the mechanism of dislocation motion across a field of solutes depends on the load and temperature, which can affect the performance of TIS and PPTIS. The MD predictions were obtained by running 50 statistically independent simulations and averaging the transition time. Assuming $\bar{t}$ follows an exponential distribution [129], the 95% confidence intervals for the MD predictions are shown in Figure. 4.2, along with the (PP)TIS predictions.

HTST overestimates the average time by two orders of magnitude relative to

the direct MD predictions. The activation potential energy obtained from the 0K string method is $\Delta V = 0.49$ eV (The potential energy profile has been presented in the supplementary material). The attempt frequency was obtained by solving for the natural frequencies of the system at the saddle and minimum potential energy configurations, $\nu_0 = 1.67 \times 10^{13}$ 1/s. The SHTST predictions shown in the table are based on using the imaginary natural frequency of the saddle configuration, 2.34×10^{11} 1/s, as the attempt frequency. These predictions overestimate the average time by four to five orders of magnitude relative to the direct MD predictions. The reason for such significant discrepancies between HTST predictions and the direct MD simulations is that HTST neglects the anharmonic effect of thermal softening on the entropy barrier. This is discussed in depth in the next subsection.

TIS provides an accurate prediction at T = 300K and T = 333K but its performance deteriorates at higher temperatures. It is known that dislocation motion is in the jerky regime at room temperature while smooth (diffusive) motion is dominant at higher temperatures [138, 91]. TIS has been designed for single event barriers, and not diffusive processes, with the performance of the shooting move deteriorating significantly for diffusive barriers, consistent with our observations. At higher temperatures, most attempts to generate trajectories that belong to the $P(\lambda_{i+1}|\lambda_i)$ ensembles failed because the generated trajectories either did not connect the initial interface to λ_{i+1} or did not cross λ_i.

PPTIS performs better than other methods at higher temperatures but it is outperformed by TIS at T = 300K and T = 333K. This is because PPTIS has been designed for diffusive processes, not single barriers. The fundamental assumption of PPTIS, i.e. loss of memory in a distance less than interface separations, is

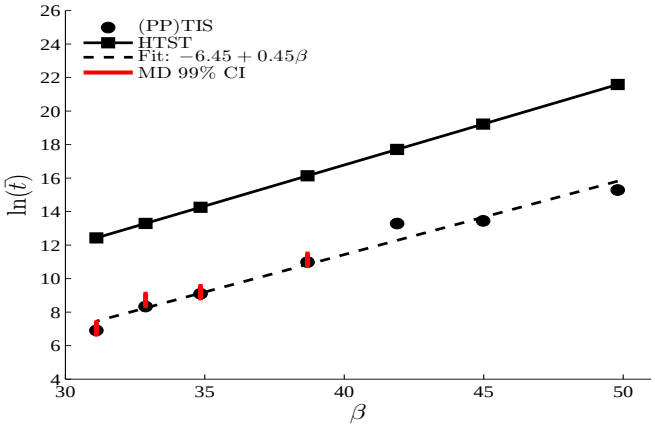

Figure 4.2: The Arrhenius plot at τ = 20MPa. PPTIS was used at temperatures higher than 333K and TIS at all other temperatures. The reason was that PPTIS provided more accurate predictions at temperatures higher than 333K relative to direct MD predictions (Section. 4.5.1). The red lines are the 95% confidence interval on the MD predictions based on the assumption that $\bar{t}$ has an exponential distribution.

not satisfied for single barriers as the system does not spend enough time near intermediate interfaces to lose its memory.

4.5.2 Temperature Effect

Given the importance of the entropy barrier and anharmonic effects in accurate prediction of the rate, this section explores the accuracy of the harmonic approximation and the Meyer-Neldel (MN) rule, as a common model accounting for thermal softening, relative to (PP)TIS. The results are used to propose a new model that can more accurately predict the entropy barrier and reaction rates, avoiding the computational cost associated with (PP)TIS. The corresponding details will be presented in the following paragraphs. First, (PP)TIS is used to compute a benchmark for the entropy barrier to which predictions of other

models are compared. To shed light on the accuracy of HTST, the vibrational entropy barrier is compared to the benchmark value, which suggests that the anharmonic effect of thermal softening cannot be neglected. Next, the MN-rule is examined and it is shown that the prediction is not as accurate as it is for dislocation-precipitate problems [104]. Finally, a simple model addressing a shortcoming of the MN rule is proposed.

First, (PP)TIS is used to compute the entropy barrier. To that end, the Arrhenius plot, i.e. $\ln(\bar{t})$ vs. $\beta = 1/k_B T$, is generated at a constant shear stress of $\tau_{xy} = 20$MPa (Fig. 4.2). The TST rate formula, Eq. 4.2, can then be used to deduce the entropy barrier and the activation energy from the Arrhenius plot. Eq. 4.2 can be rewritten as

$$\ln(\bar{t}) = -\ln[\tilde{\nu}(\tau, T)] - \frac{\Delta S(\tau, T)}{k_B} + \beta \Delta U(\tau, T) \tag{4.19}$$

from which it is clear that the slope of the Arrhenius plot is $\Delta U(\tau, T) = 0.45$ eV $\approx \Delta V$ and the y-intercept is $-(\ln[\tilde{\nu}(\tau, T)] + \frac{\Delta S(\tau,T)}{k_B})$. The entropy barrier can then be computed from Eq. 4.19 because the intercept is known and $\tilde{\nu}(\tau, T)$ can be estimated from direct MD simulations. We found $\tilde{\nu} \approx 8.55 \times 10^{10}\ s^{-1}$ at T = 300K and hence the entropy barrier is $\Delta S(\tau, T) = 8.9 k_B$. It should be noted that the linearity of the Arrhenius plot is in agreement with experimental observations [4]. Furthermore, the linearity implies that $\Delta U(\tau, T)$, $\tilde{\nu}(\tau, T)$ and $\Delta S(\tau, T)$ are likely to be temperature independent over the examined temperature range.

The benchmark entropy barrier is significantly larger than the vibrational entropy barrier, $3.85\, k_B$, which is assumed by HTST. This explains the two orders of magnitude difference between HTST predictions and the benchmarks obtained from MD simulations in the previous section. The breakdown of the harmonic approximation likely stems from the anharmonic effect of thermal softening.

A simple approach to take thermal softening into account is the Meyer-Neldel (MN) rule, $\Delta S(\tau) = \frac{\Delta V(\tau)}{T_m}$, the prediction of which will be examined next.

The MN rule, a.k.a. thermodynamics compensation law, is an empirical relation that accurately describes many thermally activated processes and can be explained from theoretical point of view as follows. Traditional continuum thermoelastic models, e.g. [38], express the activation free energy as a function of the shear modulus, $\mu(T)$, as $\Delta F(\tau, T) = \Delta U(\tau)\frac{\mu(T)}{\mu(0)}$. Based on this expression for ΔF and the assumption that μ linearly decreases with temperature and vanishes at the melting point T_m [103], the activation free energy is expressed as

$$\Delta F(\tau, T) = \Delta U(\tau)(1 - \frac{T}{T_m}) \tag{4.20}$$

Inserting Eq. 4.20 into Eq. 4.5 leads to

$$\Delta S(\tau) = \frac{\Delta U(\tau)}{T_m} \tag{4.21}$$

Assuming the melting point reported for the aluminum potential [42], T_m = 939K, the entropy barrier estimated by Eq. 4.21 is 6.18 k_B. ΔS predicted by Eq. 4.21 is not very sensitive to T_m as long as it is a reasonable choice. For instance, the closest alloy to the cell considered here, Al 5083, has a melting temperature of about 880K that results in $\Delta S(\tau)$ = 6.6 k_B.

The discrepancy between the MN rule prediction and the benchmark value stems from three sources of error. First, Eq. 4.21 only accounts for thermal softening and hence neglects configurational entropy barriers. Second, the temperature dependence of the shear modulus slightly deviates from linear for Al-Mg alloys [112]. The third source of error is that Eq. 4.20 assumes that the critical shear stress, $\hat{\tau}$, is temperature independent. Experimental studies [4] and atomistic simulations [131] have showed that this is not the case for Al-Mg alloy considered here.

To address the third source of error, we propose a simple alternative expression for ΔF that takes the temperature dependence of $\hat{\tau}$ into account and can be simply differentiated with respect to T to give $\Delta S = -\frac{\partial \Delta F}{\partial T}$. To that end, at high stresses/low temperatures, the stress dependence of ΔF is described by Friedel's model [69],

$$\Delta F(\tau, T) = \Delta F_0(T)\left(1 - \frac{\tau}{\hat{\tau}}\right)^{\frac{3}{2}} \tag{4.22}$$

where ΔF_0 is the free energy barrier at zero stress. Assuming $\hat{\tau}$ depends on temperature and using Eq. 4.20, we can express ΔF as a function of τ and T:

$$\Delta F(\tau, T) = \Delta U_0\left[1 - \frac{\tau}{\hat{\tau}(T)}\right]^{\frac{3}{2}}\left[1 - \frac{T}{T_m}\right] \tag{4.23}$$

This form resembles the continuum models suggested in [131, 132]. Furthermore, experimental studies show that $\hat{\tau}(T) = \hat{\tau}(0)(1-\frac{T}{T_m})$, where $\hat{\tau}(0)$ is the Peierls stress [4]. Therefore, Eq. 4.23 can be expressed as

$$\Delta F(\tau, T) = \frac{\Delta U_0}{\tau_0^{\frac{3}{2}}}\left[\tau_0(1 - \frac{T}{T_m}) - \tau\right]^{\frac{3}{2}}\left[1 - \frac{T}{T_m}\right]^{-\frac{1}{2}} \tag{4.24}$$

$\Delta S = -\frac{\partial \Delta F}{\partial T}$ can be computed from this equation at different temperatures and stresses. To that end, the Peierls stress, τ_0, and ΔU_0 can be obtained from atomistic simulations.

The Peierls stress for this problem is $\hat{\tau}(0) = 90$MPa, which was computed by loading the cell in increments of 5MPa and minimizing the cell using the conjugate gradient method after each load increment. In order to obtain ΔU_0, Eq. 4.24 can be fitted to ΔF vs. τ data obtained at a given temperature. To that end, $\bar{t}$ is computed in the stress range of τ =10-60 MPa at T = 300K and then the TST formula, Eq. 4.19, is used to compute ΔF at each τ. Figure. 4.3 shows $\ln(\bar{t})$ and ΔF at different stresses, respectively. The best fit to ΔF data in Fig. 4.3 is obtained for $\Delta U_0 = 0.65$ eV.

At τ =20MPa and T = 300K, the model in Eq. 4.24 results in an entropy barrier of $\Delta S = -\frac{\partial \Delta F}{\partial T} = 8.2\ k_B$, more accurate than the MN rule prediction of 6.6 k_B. Using the MN rule along with the TST rate formula, Eq. 4.19, leads to a rate prediction that is 15 times larger than that obtained based on the benchmark entropy barrier. Whereas, the proposed model leads to a rate prediction that is only three times larger. The model in Eq. 4.24 should be used at temperatures and loads that are in the vicinity of those used to calibrate the model. In this case, the entropy barrier prediction is nearly temperature and load independent in the range of T = 200-400K and $\tau = 10 - 30$MPa. For the temperature range considered here, the entropy barrier predictions are in the range ΔS =8.0-8.2 k_B. The temperature independence of the predictions is consistent with the observation from the Arrhenius plot in Fig. 4.2.

It should be noted that Friedel's model, Eq. 4.22, is valid in the limit of jerky dislocation motion, i.e. high stresses/low temperatures. In the unpinning regime, the stress dependence scales logarithmically [69]: $\Delta F(\tau, T) = 0.51\Delta F_0(T) \ln(\frac{\hat{\tau}(T)}{\tau_0})$. Hence, at low stresses/high temperatures, the model will read:

$$\Delta F(\tau, T) = 0.51\Delta U_0 \ln\left(\frac{\tau_0(1 - \frac{T}{T_m})}{\tau}\right)\left(1 - \frac{T}{T_m}\right) \tag{4.25}$$

The two expressions, Eq. 4.24 and Eq. 4.25, should render a continuous description of the activation free energy and hence should be equal for stresses and temperatures associated with transitions between the two dislocation motion regimes. Given that $\tau = 10$ MPa in Figure 4.3 is one of such points and the rest of the data points are associated with the jerky motion regime, it is enough to fit Eq. 4.24 to the data in Figure 4.3 to compute the entropy barrier. If there were more data points in the jerky motion regime, then Eq. 4.25 should be fitted to those points separately to compute the entropy barrier for the jerky motion.

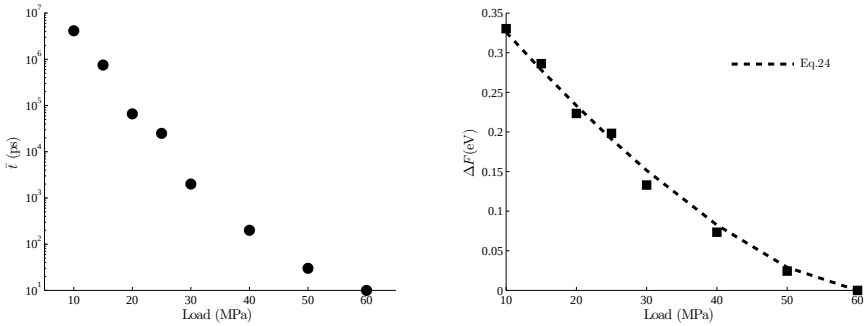

Figure 4.3: Load dependence of $\bar{t}$ (left) and the activation free energy ΔF (right) at 300K. Direct MD simulations were used at the three highest loads. PPTIS was used at 10MPa because the dislocation motion is in the smooth regime at this load and hence TIS was unable to generate enough samples for this case. The rest of the predictions have been obtained by TIS.

Lastly, it should be mentioned that the models in Eq. 4.24 and Eq. 4.25 do not account for the effects of quantization of vibrational modes at low temperatures, as described in [94], which are likely not important in the temperatures and loads considered here.

4.5.3 Load Effect

The dependence of the plastic strain rate, $\dot{\epsilon}_p$, on the applied stress, τ, is characterized by the strain rate sensitivity (SRS) factor, $m = \frac{\partial \ln \tau}{\partial \ln \dot{\epsilon}_p}$, which can be measured by macroscopic experiments. In this section, (PP)TIS is used to predict the SRS factor at experimental strain rates and the predictions are compared to experimental values. To that end, based on $\dot{\epsilon}_p \propto v \propto 1/\bar{t}$, the SRS factor can be expressed as

$$m = -\frac{\partial \ln \tau}{\partial \ln \bar{t}} \tag{4.26}$$

Therefore, m can be computed from the $\bar{t}$ vs. τ predictions in Fig. 4.3. There are two approaches to estimate m based on the data in Fig. 4.3: 1) Direct approach, and 2) TST approach. Both approaches are discussed below.

It should be noted that m can be separated into two components in solute hardened alloys: 1) an instantaneous component, m_i that is always positive, and 2) a transient component, m_t, that is characterized by strain aging [31]. It is assumed here that the time-scale associated with cross core diffusion is significantly larger than $\bar{t}$, i.e. $m = m_i$. Therefore, our predictions will be compared to experimental measurements of m_i.

The direct approach involves fitting a function to the $\ln(\bar{t})$ vs. τ data in Fig. 4.3 and then evaluating Eq. 4.26 analytically. Here, a linear function, $ln(\bar{t}) = a - b\tau$, was fitted to the data with $a = 18.68$ and $b = 0.343$ (Fig. 4.3). Based on this linear fit, the SRS factor can be expressed as $m = 1/(a - \ln(\bar{t}))$ (Fig. 4.4).

A more common approach is to use the TST formula, Eq. 4.19, to relate τ and $\bar{t}$. Eq. 4.23 is inserted into Eq. 4.19 and then τ is solved for:

$$\tau = \hat{\tau}(T)\left[1 - \left[C \ln(\bar{t}\tilde{\nu})\right]^{\frac{2}{3}}\right] \tag{4.27}$$

where $C = \frac{k_B T}{\Delta U_0[1-T/T_m]}$. Based on this equation, $1/m$ can be expressed as

$$\frac{1}{m} = -\frac{\partial \ln \bar{t}}{\partial \ln \tau} = \frac{\partial \ln(\tilde{\nu})}{\partial \ln \tau} + \frac{3\tau}{2C\hat{\tau}(T)}\left[1 - \frac{\tau}{\hat{\tau}(T)}\right]^{\frac{1}{2}} \tag{4.28}$$

The reciprocal SRS factor has two components associated with the two terms in this equation. The first component is due to the stress dependence of $\tilde{\nu}$ and it is usually assumed to be zero in the literature [88]. The predictions of the second term at T = 300K have been shown in Fig. 4.4 in the stress range of 10-60MPa.

The predictions of the two approaches are very close at low stress and begin to deviate from one another at $\tau = 30$MPa. The predictions of the di-

rect approach decrease with stress and plateaus at high stresses, consistent with [138, 91]. The predictions of the TST approach begin to increase with stress at τ = 30MPa. The reason for this has been studied in [138, 91] using line-tension models. The first term in Eq. 4.28 is negligible at low stress and gradually increases in magnitude until it becomes the dominant term at high stresses. This transition is also associated with a change in the nature of dislocation motion from smooth (unpinning) to jerky motion.

The strain rates at the two lowest loads are comparable with typical experimental conditions, i.e. $\dot{\epsilon}_p = 10^{-2} - 10^{-4} s^{-1}$, and hence the SRS predictions at those loads are compared to experimental values. Strain rate can be approximated by the Orowan equation, $\dot{\epsilon}_p = \rho_m |\mathbf{b}| d/\bar{t}$, where ρ_m is the mobile dislocation density, $|\mathbf{b}|$ is the magnitude of the Burgers vector and d is the glide distance. At low strains, ρ_m is assumed to be in the $10^{11} - 10^{12} m^{-2}$ range [66, 88]. Using $\rho_m = 10^{11} m^{-2}$ and given that $|\mathbf{b}|$ = 0.286 nm and d $\approx$ 1 nm, the strain rates at the two lowest loads are 7×10^{-4} and 7×10^{-3}.

The SRS predictions at experimental strain rates are an order of magnitude larger than experimental values of m_i [110, 111, 4, 92]. To the best of our knowledge, this is the first prediction of the SRS factor based solely on atomistic simulations at experimental strain rates. One reason for the discrepancy between the predicted SRS factor and experimental values is that our model neglects the effect of forest dislocations [110, 111]. Another important factor that can contribute to the discrepancy is the artificial boundary effects associated with the small periodic cell considered here [116].

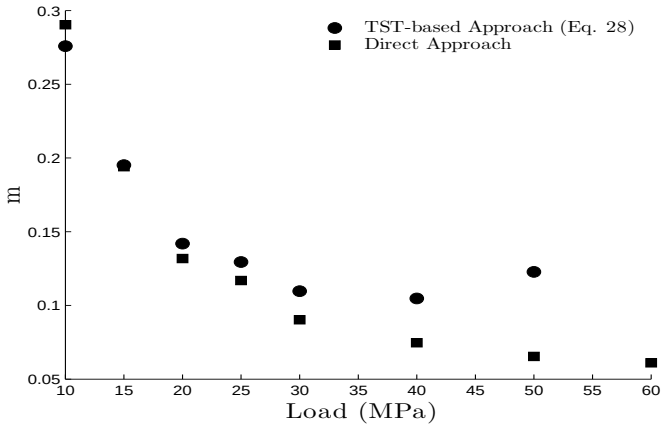

Figure 4.4: Strain rate sensitivity vs load at T = 300K.

4.6 Summary and Conclusions

The rate at which dislocations overcome a field of solutes is studied at different temperatures and loads using atomistic simulations. First, the performance of HTST, as the most common approach in the literature, was examined for a benchmark problem. It was shown that HTST was incapable of providing accurate predictions. The next step was to evaluate the performance of TIS, as the method has been shown to accurately predict the rate of dislocation-precipitate interactions. It was observed that TIS provides accurate predictions at high loads and low temperatures where dislocation motion is in the jerky mode. However, TIS predictions are inaccurate in the regime of smooth dislocation motion where the barrier is of diffusive nature. This spurred the use of PPTIS, a variant of TIS designed for diffusive barriers. It was observed that PPTIS predictions are accurate when the dislocation motion is smooth but the method falls short for jerky dislocation motion.

TIS and PPTIS were then used to compute the entropy barrier and to study

the validity of the harmonic approximation. To that end, the Arrhenius plot generated by the two methods were compared to that of HTST. The two Arrhenius plots were parallel but had different intercepts. This indicates that dislocation-solute interactions have a large entropy barrier that is temperature independent. It was shown that the Meyer-Neldel rule, which is equivalent to linear softening of the shear modulus with temperature, was able to predict the entropy barrier with a reasonable accuracy. This shows that the large entropy barrier is mostly due to the anharmonic effect of thermal softening, which cannot be captured by HTST.

The MN rule prediction, however, was not as accurate as it was for dislocation-precipitate interactions in Al-Cu alloys [104]. The main sources of error are: 1) the temperature dependence of the shear modulus in Al-Mg alloys slightly deviates from linear, 2) the MN rule assumes that the critical shear stress is temperature independent while both experimental and atomistic models suggest the contrary. Based on the second point, an expression for the activation free energy was proposed that can be differentiated with respect to temperature to obtain the entropy barrier. The model provided an accurate prediction of the entropy barrier and hence can be used along with TST to accurately predict the rate.

The load dependence of the rate was studied using (PP)TIS and direct MD simulations. The SRS factor was computed directly based on atomistic predictions of the rate for a range of stresses, including those corresponding to experimental strain rates. It was shown that the SRS factor decreases with increasing load and eventually plateaus, consistent with [91]. To the best of our knowledge, this is the first prediction of the SRS factor at experimental strain rates

based solely on atomistic simulations. Given that our predictions do not take into account strain aging, we compared the predictions with experimental values of the instantaneous component of the SRS factor and found that the predictions are about an order of magnitude larger. One reason for the discrepancy is that our simulations neglect the effect of forest dislocations [110]. Another important factor that shall be considered in future studies is the boundary effects associated with the small periodic cell considered here [116].

The SRS factor was also computed using a common method in the literature, based on TST and Friedel's model. In this approach, the pre-exponential factor of the TST equation is assumed to be stress independent and the dislocation is assumed to overcome one obstacle at a time. It was shown that the approach leads to predictions that are very close to those based on the direct approach at low loads but start to deviate at higher stresses. The reason is that the pre-expoential factor is no longer stress independent at high loads.

Finally, this paper encourages similar studies that evaluate the utility of different methods for different applications. The importance of this point will be more clear if one notes the nuances between the above conclusions and those in an analogous paper on dislocation-precipitate interactions [104] and those in others that study dislocation nucleation. HTST was shown to be inaccurate for all of these problems [86, 104]. TST was found to be accurate for dislocation nucleation [86] but difficult to apply for dislocation-precipitate interactions [104]. TIS was found to be accurate for dislocation-precipitate interactions [104] while it is only accurate for dislocation-solute interactions in the case of jerky dislocation motion. PPTIS, on the other hand, is only accurate in the case of smooth dislocation motion. The MN rule provides a precise prediction for dislocation-

precipitate interactions but it is not as accurate for dislocation-solute interactions. Given these nuances, there is no silver bullet approach and hence a rate theory must be tested against direct MD simulations before being used for an application.

Acknowledgements

The authors acknowledge Dr. Bernard Ross for financially supporting this research through the Cornell Ross-Tetelman Fellowship.

Supplementary Material

The initial and final configurations were determined based on the idea of a one-dimensional energy landscape presented in [88]. A straight edge dislocation is placed at a position, x, along the glide direction and then the simulation box is relaxed at 0K under the applied load, τ_{xy}. This procedure is repeated for many initial positions, x, in 3 increments along the glide direction (Fig. 4.5). There are three energy barriers between the four minima (red triangles). The barrier associated with the transition from the third minimum, $x = 31$ to the fourth, $x = 44$, is the largest barrier with $\Delta V = 0.49$ eV. The associated potential energy profile is shown in Figure. 4.6. Hence, the two configurations associated with the two minima are selected as the initial and final configurations, which are shown in Fig.4.1. The minima for all other shear stresses, τ_{xy}, considered in this work happened to be at the same locations and the largest energy barrier was between the third and the fourth minima in all cases.

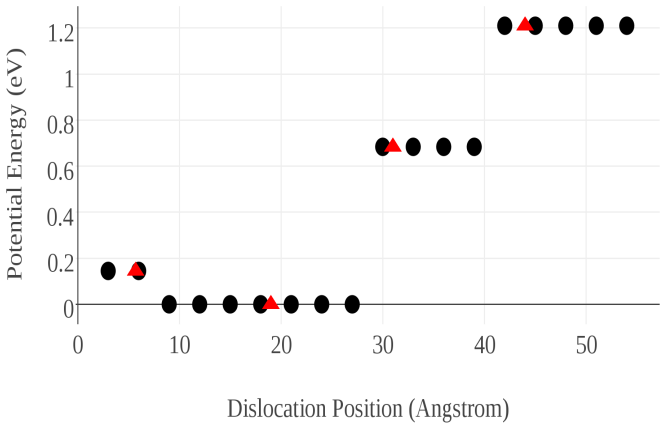

Figure 4.5: The potential energy of the system after relaxation versus the dislocation position at τ_{xy} = 20MPa. The initial positions are shown in black circles and the red triangles indicate the final position of the dislocation.

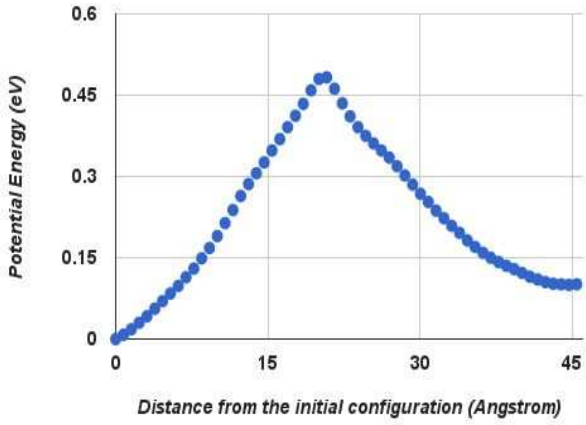

Figure 4.6: The potential energy of the images along the 0K string with respect to the potential energy of the initial image. The distance of each image from the initial image has been measured by the Eucleadian norm.

CHAPTER 5

ATOMISTIC PREDICTION OF DISLOCATION MOTION THROUGH KINK-PAIR NUCLEATION IN BCC METALS

By S. Saroukhani, D. Warner

5.1 Abstract

Accurate prediction of the rate of dislocation motion is the first step in defining dislocation mobility laws in larger scale models of plasticity. In this spirit, the slip rate of a screw dislocation is studied using different variants of the Harmonic Transition State Theory, as the most common approach in the literature, and the modern technique of Transition Interface Sample. The performance of the methods is examined by comparing their predictions to benchmarks obtained by MD simulations. It is shown that different variants of the Harmonic Transition State Theory provide grossly inaccurate predictions, whereas TIS was found to be very effective in predicting the rate. To investigate the accuracy of the harmonic approximation, the temperature dependence of the rate and the entropy barrier are studied. It is shown that the problem has a significant entropy barrier, not capture by common variants of HTST. With that in mind, the performance of the Meyer Neldel (MN) rule, as the most common entropy estimation approach material mechanics, is studied. It is found that the MN rule significantly underestimates the entropy barrier. To investigate this issue, the theoretical justification of the MN rule for dislocation processes, which is often neglected in the literature, is revisited. It is discussed that the method neglects the configurational entropy and is only suitable for problems where temperature dependence stems from that of elastic constants and hence the anhar-

monic vibrational entropy. Having established that, the configurational entropy is studied and it is found that an accurate prediction can be obtained from the simple model of Hirth and Lothe, which can be added to the MN rule prediction to provide a fairly accurate estimate of the entropy barrier. This estimate can be combined with the Transition Sate Theory to provide a simple and accurate rate prediction approach.

5.2 Introduction

Different variants of HTST are commonly used in dislocation mobility laws in meso-scale models such as Crystal Plasticity [24, 85, 71], Kinetic Monte Carlo [113, 25, 22] and Dislocation Dynamics [93, 30]. The HTST rate formula has an Arrhenius form involving the activation potential energy and a pre-exponential factor that encompasses the entropy barrier and the attempt frequency. The original form of HTST approximates the entropy barrier by the harmonic vibrational entropy barrier at 0K and neglects configurational entropy [127]. However, approximating the vibrational entropy involves solving two eigenvalue problems that can be prohibitively expensive for large systems. That is why the frequency of the softest mode of the initial configuration is often used as the pre-exponential factor [54], which is equivalent to assuming that the entropy barrier is zero. Other estimates of the pre-exponential factor such as continuum estimates [140], Debye frequency, the imaginary frequency of the saddle configuration [99] and etc have also been proposed. We will refer to these approaches as Simplified HTST.

The performance of different variants of HTST in predicting the rate of vari-

ous dislocation processes in FCC metals has been studied recently. The authors and their co-workers have shown that the method fails to predict the rate for dislocation-precipitate interactions and dislocation motion through a field of solutes ([104] and Chapter 4). The method has also been shown to be inaccurate for dislocation nucleation problems [86, 102]. In these cases, it has been proposed that the anharmonic effect of thermal softening is the main behind the inaccuracy of HTST.

The Meyer-Neldel (MN) rule is the most common approach for accounting for entropy barriers in the material mechanics community. The method has been shown to be accurate for dislocation nucleation [103] and dislocation-precipiate interactions [104] in FCC metals. However, Saroukhani and Warner (Chapter 4) have shown that the method is not as accurate for the problem of dislocation motion through a field of solute because the method neglects the temperature dependence of the critical shear stress. To address this issue, they propose a modified version that assumes the critical stress linearly decreases with temperature and vanishes at the melting temperature.

The restrictive assumptions in HTST and the lack of clear theoretical background behind the MN rule have spurred the use of more advanced rate theories and accelerate MD techniques. To account for thermal effects, for example, the Transition State Theory has been applied with various free energy calculations techniques [102, 86, 98]. Among accelerated MD techniques, Parallel Replica Dynamics (PRD) [131] and Hyperdynamics [54] have been successfully applied to dislocation nucleation in FCC metals.

However, restrictive assumptions hinder the general applicability of these models, compromise their accuracy in some cases and some of them are dif-

ficult to implement. For instance, an accurate reaction coordinate and a free energy profile is required for a TST prediction, which can be very challenging. Saroukhani et al. [104] have shown that even a powerful technique such as the Finite Temperature String method [120] fails to provide a reasonable free energy profile for dislocation-precipitate interactions. It will be shown in this manuscript that a lot of experience with FTS and intuition about the physics of the problem is needed to compute a reasonable reaction coordinate for kink-pair formation in a screw dislocation. As another example, Hyperdynamics needs an artificial potential that is application specific and the implementation of the method requires significant changes to a regular MD program. PRD [129] is simple to implement and has become available in LAMMPS recently but the method provides a speedup that at most scales with the number of available replicas and hence it is not satiable for problems with small rates.

Path sampling techniques, mostly developed and adopted in the biophysics and chemistry communities, come with a more degree of generality in the sense that they do not require carefully chosen reaction coordinates, prior knowledge about transitions state and free energy profiles [44]. These methods are based on efficient sampling algorithms that allow for actual trajectories of the system as it goes through a transition to be used to extract transition features such rate constants, reaction coordinates, free energy profiles and etc [90, 34, 9, 14, 32]. Given the difficulties involved in sampling low probability regions of the phase space, many modern path sampling techniques such as different variants of Transition Interface Sampling [82, 121, 15, 119, 11, 81], Forward Flux Sampling [1] and milestoning [125, 123, 76] are based on partitioning the phase space using a proper order parameter and then sampling smaller regions of the phase space. Despite their high popularity in the bio-physics and chemistry communities, path

sampling techniques have not drawn much attention in the material mechanics community yet.

To the best of our knowledge, different variants of Transition Interface Sampling are the only Path Sampling techniques that have been adopted in the material mechanics community. The authors [104] adopted the original version of the method [82] as well as the Path Swapping version [118] to accurate predict the rate and entropy barrier of dislocation-precipitate interactions. It was shown later (Chapter 4) that the method is capable of predicting the rate of dislocation motion through a field of solutes in the jerky motion regime, but fails to do so in the smooth motion regime. The Partial Path TIS approach - designed for problems with diffusive barriers - was the adopted for predicting the rate in the smooth motion regime.

Although the performance of TIS, FTS, HTST and the MN rule has been tested against direct MD benchmarks for different dislocation processes in FCC metals, it is not a priori clear whether the results are directly transferable to screw dislocations and BCC metals. In particular, the fact that BCC transition metals such as tungsten have high melting temperatures and stronger bonds may suggest that the harmonic approximation might be more accurate for predicting dislocation properties in them. In fact, some of the prominent models of screw dislocation in BCC transition metals [51, 52, 53, 39, 57] are based on the HTST. The entropy barrier is neglected in most cases by using a SHTST approach but there are cases where the MN rule is used to estimate the entropy barrier [30, 93]. The applicability of TIS and FTS for kink-pair nucleation is not clear either because there are multiple entangled reaction channels for the glide of a screw dislocation due to non-Schmid effects [28, 37]. It is therefore of sig-

nificant interest to examine the utility of TIS, FTS, HTST and the MN rule in predicting the rate of dislocation motion through kink-pair nucleation.

This chapter begins with a brief description of the theoretical background of each method. In Section 5.4, the details of the atomistic simulations are explained. In Section 5.5.1, the applicability of FTS and the details of implementation of the method are discussed. In Section 5.5.2, predictions of TIS and different variants of HTST are compared to those of direct MD simulations for a few benchmark problems. The validity and the assumptions of the harmonic approximation and the MN rule for predicting the entropy barrier is discussed in Section 5.5.3. The performance of the configurational entropy barrier model of Hirth and Lothe is also examined in the same section. In the final section, the conclusions are summarized and potential future directions are discussed.

5.3 Methods

5.3.1 Transition State Theory

Original form

The transition rate, k_{ab}, from a state, a, to another, b, is defined as the number of transitions per unit time spent in a, i.e.

$$k_{ab} = \lim_{\tau \to \infty} \frac{N(\tau)}{\int_0^\tau h_a(r(t))dt} \tag{5.1}$$

where τ is time, r is the coordinates of the system, $N(\tau)$ is the number of transitions during τ, and h_a is the indicator function. To compute the rate based

on this definition, TST, in its oldest form [68, 80], assumes that the phase space can be partitioned into two distinct sets, a and b, parametrized by a continuous function $\lambda(r) : R^n \rightarrow R$ such that

$$\begin{aligned} a &= \{r : \lambda(r) < \lambda^\star\} \\ b &= \{r : \lambda(r) > \lambda^\star\} \end{aligned} \tag{5.2}$$

where $\lambda^\star$ defines the boundary between the sets. This means that a transition from a to b, or vice versa, is characterized by the system crossing the boundary $\lambda^\star$. The function $\lambda(r)$ together with $\lambda^\star$ are usually called a reaction coordinate.

The second major assumption of TST is that the system is ergodic, i.e.

$$< h_a >= \lim_{\tau\rightarrow\infty} \frac{1}{\tau} \int_0^\tau h_a(r(t))dt = \int_a \int_{R^n} p(r, v)dvdr \tag{5.3}$$

where $p(r, v)$ is an equilibrium distribution such as the Gibbs distribution. Based on this assumption, Eq. 5.1 can be expressed as

$$k_{ab} = \frac{\lim_{\tau\rightarrow\infty} \frac{N(\tau)}{\tau}}{< h_a >} = \frac{\nu}{< h_a >} \tag{5.4}$$

where ν is called the mean transition frequency. To compute the rate based on Eq. 5.4, a computable expression for ν is needed. TST assumes that the system is in equilibrium throughout the transition to derive such an expression. A brief summary of the derivations is presented in the following paragraphs.

$\dot{h}_a(r(t))$ is a delta function, $\delta(\cdot)$, at transition points and hence $N(\tau) = \frac{1}{2}\int_0^\tau |\dot{h}_A(r(t))|dt$. Therefore, the mean transition frequency can be written as

$$\begin{aligned} \nu &= \lim_{\tau\rightarrow\infty} \frac{N(\tau)}{\tau} \\ &= \lim_{\tau\rightarrow\infty} \frac{1}{2\tau} \int_0^\tau |\dot{h}_a(r(t))|dt \\ &= \lim_{\tau\rightarrow\infty} \frac{1}{2\tau} \int_0^\tau |\nabla h_a(r) \cdot v|dt \\ &= \frac{1}{2} \int_{R^n\times R^n} p(r, v)|\nabla h_a(r) \cdot v|drdv \end{aligned} \tag{5.5}$$

Using $h_a(r) = \theta(\lambda^\star - \lambda(r))$, where $\theta(\cdot)$ is the Heaviside function, and noting that $\nabla\theta(\lambda^\star - \lambda(r)) = -\delta(\lambda(r) - \lambda^\star)\nabla\lambda$, we can rewrite Eq. 5.5 as

$$\begin{aligned}
\nu &= \frac{1}{2}\int_{R^n\times R^n} p(r,v)\delta(\lambda(r)-\lambda^\star)|\nabla\lambda\cdot v|drdv \\
&= \frac{1}{2}\int_{R^n\times R^n} p(r,v)\delta(\lambda(r)-\lambda^\star)|\dot{\lambda}(r)|drdv \\
&= \frac{1}{2} < \delta(\lambda(r)-\lambda^\star)|\dot{\lambda}(r)| > \\
&=< \delta(\lambda(r)-\lambda^\star)\dot{\lambda}(r)\dot{\theta}(\lambda) >
\end{aligned} \tag{5.6}$$

where the last equality follows from $p(r,v) = p(r,-v)$. Plugging Eq. 5.6 into Eq. 5.4 and using $h_a(r) = \theta(\lambda^\star - \lambda(r))$, the transition rate can be written as

$$k_{ab}^{TST} = \frac{< (\lambda(r)-\lambda^\star)\dot{\lambda}(r)\dot{\theta}(\lambda) >}{< \theta(\lambda^\star - \lambda(r)) >} \tag{5.7}$$

This equation can be divided and multiplied by $< \delta(\lambda(r) - \lambda^\star) >$ to be rewritten as

$$k_{ab}^{TST} = \frac{< (\lambda(r)-\lambda^\star)\dot{\lambda}(r)\dot{\theta}(\lambda) >}{< \delta(\lambda(r)-\lambda^\star) >}\frac{< \delta(\lambda(r)-\lambda^\star) >}{< \theta(\lambda^\star - \lambda(r)) >} \tag{5.8}$$

The first fraction is the flux through $\lambda^\star$ and is equal to $\sqrt{\frac{k_BT}{2\pi m}}$, where T is the temperature and k_B is the Boltzmann constant. The second fraction is often written as $\frac{Z_{\lambda^\star}}{Z_a}$ where Z_Γ is the partition function constrained to a region, Γ, of the phase space. Therefore, Eq. 5.8 can be written in the more familiar form:

$$k_{ab}^{TST} = \sqrt{\frac{k_BT}{2\pi m}}\frac{Z_{\lambda^\star}}{Z_a} \tag{5.9}$$

Often, a surface, λ_0, which does not intersect with $\lambda^\star$ and contains an initial configuration in a, is defined to express Eq. 5.9 in terms of the free energy barrier, ΔF, as

$$k_{ab} = \tilde{\nu}e^{-\frac{\Delta F}{k_BT}} \tag{5.10}$$

where

$$\tilde{\nu} = \sqrt{\frac{K_BT}{2m\pi}}\frac{Z_{\lambda_0}}{Z_a} \tag{5.11}$$

and the free energy barrier is

$$\Delta F = F_{\lambda^\star} - F_{\lambda_0} = -k_B T \ln\left(\frac{Z_{\lambda^\star}}{Z_{\lambda_0}}\right) \tag{5.12}$$

which can also be written as

$$\Delta F(\boldsymbol{\sigma}, T) = \Delta U(\boldsymbol{\sigma}, T) - T\Delta S(\boldsymbol{\sigma}, T) \tag{5.13}$$

with $\Delta U(\sigma, T)$ being the activation internal energy and $\Delta S(\sigma, T)$ the activation entropy.

Bennet-Chandler Version

The TST assumption that the two initial and final states, a and b, partition the phase space is often not the case. A transition is often between two meta-stable states, A and B, that do not have a sharp boundary in the phase space, i.e. $A \subset a$ and $B \subset b$. Therefore, a transition in such cases cannot be characterized by crossing a hypersurface, like it is assumed in TST. In such cases, trajectories of the system might cross the dividing hypersurface, $\lambda^\star$, before committing to B and may not even commit to B at all. This means that the flux through $\lambda^\star$ is an upper bound to the flux associated with the transition from A to B. Hence, the TST rate in Eq. 5.10 is an upper bound to k_{AB}, i.e. $k_{AB} \leq k_{ab}^{TST}$.

Bennett-Chandler (BC) TST proposed a remedy for this challenge [8, 27, 80] whereby the flux through $\lambda^\star$ is modified such that only trajectories that reach the final state are counted and multiple recrossings are counted only once. The latter is done by weighting forward and backward crossings with different signs such that they cancel out. In practice, this amounts to scaling k_{ab}^{TST} by the probability, κ, that each crossing towards B leads to a transition, meaning

$$k_{AB} \approx \kappa k_{ab}^{TST} \tag{5.14}$$

where $\kappa = \lim_{N\to\infty} \frac{2N_B}{N}$, a.k.a. the transmission coefficient, is computed by starting a large number, N, of trajectories from an equilibrium distribution on $\lambda^\star$ and counting the number, N_B, that commit to B in a time $t^* << 1/(k_{AB} + k_{BA})$. For the BC-TST approach to be effective, the dividing surface, $\lambda^\star$, must be chosen such that κ is close to one. In other words, $\lambda^\star$ must be a bottleneck for the transition such that trajectories crossing it have a high probability of committing to B. Otherwise, an infeasible number of trajectories are needed to compute κ accurately. It is worth noting that there are more efficient approaches for defining κ based on the *effective positive flux* formalism [121], which avoids counting positive and negative crossings by only counting the first *positive* crossing for *effective* trajectories [15].

The Harmonic Approximation

Harmonic TST avoids the challenging task of free energy computations by assuming that the potential energy surface is quadratic at the initial and saddle configurations. The latter means that each degree of freedom is assumed to be a harmonic oscillator. There are two consequences for this assumption: 1) material properties are assumed to be temperature independent; 2) the entropy barrier is assumed be stem solely from small vibrations of atoms and anharmonic and configurational contributions are neglected. The method further assumes that the dividing surface corresponds to a potential energy ridge, λ_D^V, between A and B to express the transition rate as

$$k_{AB} \approx \frac{L}{|b|} \left(\frac{\prod_{i=1}^{3N} \nu_i^{\text{initial}}}{\prod_{i=1}^{3N-1} \nu_i^{\text{saddle}}} \right) e^{-\frac{\Delta V}{k_B T}} = \nu_0 e^{-\frac{\Delta V}{k_B T}} \tag{5.15}$$

where ν_i^{initial} and ν_i^{saddle} are respectively the normal frequencies of the system in the initial and saddle configurations. The product over the saddle point frequencies excludes the imaginary frequency in the direction of the reaction coordinate, i.e. normal to λ_D^V, and hence all frequencies are real. N is the number of atoms in the system, L is the dislocation length, $\boldsymbol{b}$ is the Burgers vector and ΔV is the difference in the potential energy between the saddle and initial configurations. The quantity $\frac{L}{|\boldsymbol{b}|}$ is the number of kink-pair nucleation sites.

In practice, however, the two eigenvalue problems involved in computing the rate from Eq. 5.15 are often avoided because they can be very expensive for large systems. Often an estimate, ν_*^{initial}, is used for the attempt frequency:

$$k_{AB} \approx \frac{L}{|\boldsymbol{b}|}\nu_* e^{-\frac{\Delta V}{k_B T}} \tag{5.16}$$

We will refer to such approaches as the Simplified HTST (SHTST). Many alternatives have been proposed. Among the most common are the imaginary frequency of the saddle configuration, the natural frequency of the initial configuration in the direction of the reaction coordinate, Debye frequency and continuum estimates [54, 99, 140, 50].

An attempt frequency estimate that has been used extensively for kink-pair nucleation is the fundamental mode of the Granato-Lucke vibrating string [113, 72]:

$$\nu_* = C_t \pi / l \tag{5.17}$$

where C_t is shear wave velocity and L is a characteristic wave length. C_t is often taken to be $C_t = \sqrt{\mu/\rho}$ wjere μ is the shear modulus and ρ is the mass density. l is taken to be equal to the kink-pair separation, d, plus the lattice constant, a.

Challenges with TST and HTST

The TST rate expression, Eq. 5.8, requires calculation of the free energy as a function of the reaction coordinate $\lambda(r)$. This could be a computationally demanding task; more importantly, it signifies the role of a proper reaction coordinate in the accuracy of TST rate predictions. An inaccurate choice for the reaction coordinate can lead to significant errors in the free energy profile and hence the rate prediction. Moreover, a choice of $\lambda^\star$ that is not sufficiently close to the actual transition state leads to poor convergence of the transmission coefficient κ.

To avoid these complexities, different variants of HTST have been used to describe the rate of dislocation processes for decades. As will be discussed in the rest of this chapter, the method assumes temperature independent material properties, which does not hold true in many cases. Such restrictive assumptions and practical difficulties in TST and HTST have spurred the development of many modern methods based on sampling the transition path ensemble in the chemistry and bio-physics communities [130, 129, 119]. Such methods are usually more general and do not require free energy computations and accurate reaction coordinates. We are going to briefly describe the TIS method, as one of the path sampling techniques previously tested for dislocation processes, in the next section.

5.3.2 Transition Interface Sampling

Unlike TST based approaches, TIS is a direct algorithm to compute the rate in Eq. 5.1 in the sense that it uses short trajectories of the system as it goes through the transition. This is achieved by partitioning the phase space using a set of

$n+1$ non-intersecting interfaces, defined as level sets, λ_i, of an order parameter, $\lambda(\mathbf{x})$, i.e. $\{\mathbf{x}|\lambda(\mathbf{x}) = \lambda_i\}$, $i = 0, ..n$. The order parameter, $\lambda(\mathbf{x})$, does not have to be a properly chosen reaction coordinate; it is sufficient that $\lambda(\mathbf{x})$ characterizes the basins of attraction of A and B [80, 119, 121]. As schematically shown in Fig. 5.2, each interface, λ_i, is closer to A than the next interface, λ_{i+1}, such that $\lambda_0 = \lambda_A$ defines the boundary of the basin of attraction of A and $\lambda_n = \lambda_B$ defines that of B. The transition rate to an interface, k_{λ_i+1}, is then equal to that of the previous interface, k_{λ_i}, times the probability that the system crosses λ_{i+1} after crossing λ_i. This is analogous to the BC-TST concept whereby k_{AB} is equal to the transition rate to the dividing surface, $k_{ab}[\lambda^\star]$, multiplied by the probability, κ, that the system commits to B after crossing $\lambda^\star$.

The transition rate to the first interface, k_{λ_1} can be calculated with direct MD simulations because λ_1 can be close to A. Then, analogous to Eq. 5.14, the transition rate to the second interface is

$$k_{\lambda_2} = k_{\lambda_1} p(\lambda_2|\lambda_1) \tag{5.18}$$

where $p(\lambda_2|\lambda_1)$ is the probability that the system crosses λ_2 after crossing λ_1. Note that there is only one interface, λ_1, between A and λ_2, and Eq. 5.18 is the same as Eq. 5.14 with $\kappa = p(\lambda_2|\lambda_1)$ and $k_{ab}^{TST} = k_{\lambda_1}$. Similarly, k_{λ_3} can be written as

$$k_{\lambda_3} = k_{\lambda_2} p(\lambda_3|\lambda_2) = k_{\lambda_1} p(\lambda_2|\lambda_1) p(\lambda_3|\lambda_2) \tag{5.19}$$

In analogy with Eq. 5.14, we have $\lambda^\star = \lambda_2$ and the final state is λ_3 and $\kappa = p(\lambda_3|\lambda_2)$. From Eqs. 5.18 and 5.19, the rate of transition from A to λ_{i+1} is

$$k_{\lambda_{i+1}} = k_{\lambda_i} p(\lambda_{i+1}|\lambda_i) = k_{\lambda_1} \prod_{j=1}^{j=i} p(\lambda_{j+1}|\lambda_j) \tag{5.20}$$

and hence

$$k_{AB} = k_{\lambda_n} = k_{\lambda_1} p(\lambda_n|\lambda_1) = k_{\lambda_1} \prod_{j=1}^{j=n-1} p(\lambda_{j+1}|\lambda_j) \tag{5.21}$$

where $p(\lambda_{j+1}|\lambda_j)$ is the probability that the system crosses λ_{i+1} after crossing λ_i. To compute $p(\lambda_{j+1}|\lambda_j)$, one samples the ensemble of trajectories of the system that start in A, cross λ_i and then either go back to A or move forward to cross λ_{i+1}. The probability $p(\lambda_{j+1}|\lambda_j)$ is then estimated as

$$p(\lambda_{j+1}|\lambda_j) = \frac{N^{(A\to i\to i+1)}}{N^{(A\to i)}} \tag{5.22}$$

where $N^{(A\to i)}$ is the total number of samples in the ensemble and $N^{(A\to i\to i+1)}$ is the number of samples that connect A to λ_i and then to λ_{i+1}. For instance in Fig. 5.2, $p(\lambda_2|\lambda_1)$ is equal to the number of the blue trajectories, $N^{(A\to 1\to 2)}$, divided by the number of the blue and red trajectories, $N^{(A\to i)}$.

Trajectories needed to compute $p(\lambda_{j+1}|\lambda_j)$ cannot be generated with direct MD simulations as interfaces far from A can be in low probability regions of the phase space. The shooting move algorithm, which is an MCMC algorithm, is often used to generate such trajectories [119]. Like other MCMC techniques, the algorithm starts with tweaking an existing sample to generate a new sample and then evaluating the new sample according to an acceptance rule that is designed to ensure samples are drawn from the desired probability distribution. The details of the algorithm have been extensively discussed in the path sampling literature [119, 80, 15, 121].

Statistical Error in TIS simulations

The statistical error of the estimator in Eq. 5.21 can be measured by the coefficient of variation, $c_v = \sqrt{\frac{\text{Var}[k_{AB}]}{k_{AB}^2}}$, where Var$[\cdot]$ is the variance. With the assumption that λ_1 is sufficiently close to A and hence k_{λ_1} can be computed with high accuracy, Var$[k_{AB}]$ is proportional to Var$[p(\lambda_n|\lambda_1)]$. Therefore, the coefficient of

variation can be written as

$$c_v = \frac{\mathrm{Var}[p(\lambda_n|\lambda_1)]}{p(\lambda_n|\lambda_1)^2} \tag{5.23}$$

Given that $p(\lambda_n|\lambda_1) = \prod_{j=1}^{j=n-1} p(\lambda_{j+1}|\lambda_j)$, the error propagation formula,

$$Var[f(x,y,...)] = (\frac{\partial f}{\partial x})^2 \mathrm{Var}[x] + (\frac{\partial f}{\partial y})^2 \mathrm{Var}[y] + ... \tag{5.24}$$

can be used to express the variance as

$$\begin{aligned} \mathrm{Var}[p(\lambda_n|\lambda_1)] &= \sum_{i=0}^{n-1} (\frac{\partial p(\lambda_n|\lambda_1)}{\partial p(\lambda_{i+1}|\lambda_i)})^2 \mathrm{Var}[p(\lambda_{i+1}|\lambda_i)] \\ &\approx p(\lambda_n|\lambda_1)^2 \sum_{i=0}^{n-1} \frac{\mathrm{Var}[p(\lambda_{i+1}|\lambda_i)]}{p(\lambda_{i+1}|\lambda_i)^2} \end{aligned} \tag{5.25}$$

For a given number of samples, $N^{(A\to i)}$ in the ensemble of $p(\lambda_{i+1}|\lambda_i)$, the variance $\mathrm{Var}[p(\lambda_{i+1}|\lambda_i)]$ can be expressed as

$$\mathrm{Var}[p(\lambda_{i+1}|\lambda_i)] = \frac{\mathrm{Var}[N^{(A\to i\to i+1)}]}{(N^{(A\to i)})^2} \tag{5.26}$$

Assuming that the events being counted in estimating $p(\lambda_{i+1}|\lambda_i)$ are outcomes of $N^{(A\to i)}$ shooting trials that follow the binomial distribution, the variance $\mathrm{Var}[N^{(A\to i\to i+1)}]$ can be written as

$$\mathrm{Var}[N^{(A\to i\to i+1)}] = N^{(A\to i)} p(\lambda_{i+1}|\lambda_i)(1 - p(\lambda_{i+1}|\lambda_i)) \tag{5.27}$$

Therefore, Eq. 5.26 and Eq. 5.27 can be used to express the coefficient of variation for each interface as

$$c_v^i = \sqrt{\frac{(1 - p(\lambda_{i+1}|\lambda_i))}{N^{(A\to i)} p(\lambda_{i+1}|\lambda_i)}} \tag{5.28}$$

Moreover, Eq. 5.26 and Eq. 5.27 can be used to express $\mathrm{Var}[p(\lambda_n|\lambda_1)]$ in Eq. 5.25 as

$$\mathrm{Var}[p(\lambda_n|\lambda_1)] = p(\lambda_n|\lambda_1)^2 \sum_{i=0}^{n-1} \frac{1 - p(\lambda_{i+1}|\lambda_i)}{N^{(A\to i)} p(\lambda_{i+1}|\lambda_i)} \tag{5.29}$$

Therefore, c_v in Eq. 5.23 can be written as

$$\begin{aligned} c_v &= \sqrt{\sum_{i=0}^{n-1} \frac{1 - p(\lambda_{i+1}|\lambda_i)}{N^{(A\to i)} p(\lambda_{i+1}|\lambda_i)}} \\ &= \sqrt{\sum_{i=0}^{n-1} (c_v^i)^2} \end{aligned} \tag{5.30}$$

References [20] and [19] have presented algorithms for finding interfaces that minimize c_v as well as the computational cost of TIS simulations. In this contribution, we have not used those algorithms for determining the interfaces but we have used the above derivations to determine and constrain the statistical errors in our predictions.

5.3.3 Finite Temperature String Method

FTS is a powerful algorithm for computing reaction coordinates and free energy profiles [96, 97, 98, 124, 134]. The method has been used extensively with TST-based approaches for both reaction coordinate (RC) and free energy calculations [87, 86, 98, 95] as well as with TIS [104] and similar methods such as mile-stoning [123, 76] and forward flux sampling [1] for its capability in providing quality order parameters. The algorithm has two main steps: 1) computing a reaction coordinate, 2) computing the free energy profile associated with the reaction coordinate. In the first step, the method utilizes the idea that an ideal reaction coordinate can be defined as high probability regions of iso-committor surfaces, i.e. surfaces where the probability that a trajectory reaches B before A is uniform [96, 97, 98, 124, 134]. It offers an algorithm for finding iso-committer surfaces and the expected configuration on each of them and defines an RC as a curve (string) connecting the expected configurations (images). In the second

step, the global balance equation, as the probabilistic definition of equilibrium, is used to compute the free energy profile.

The input to the first step is an initial set of equally spaced intermediate configurations (images), $\boldsymbol{\psi}_\alpha^0$, $\alpha = 0, ..., N$, such that $\boldsymbol{\psi}_0^0$ is the initial configuration and $\boldsymbol{\psi}_N^0$ is the final configuration. The initial images define a set of Voronoi cells in the configuration space. As will be described below, the algorithm involves constrained sampling within each cell. Therefore, an initial replica of the system, $\boldsymbol{x}_\alpha^0 = \boldsymbol{\psi}_\alpha^0$, is created in each cell. Then, the position of the cell centers (images) is iteratively updated through the following steps [120]:

1. The constrained sampling within each Voronoi cell is performed as follows. At each time step, $n \geq 0$, update the position of the system within each cell, $\boldsymbol{x}_\alpha^n$, through the time-discretized version of the overdamped Lagevin equation:

$$\boldsymbol{x}_\alpha^* = \boldsymbol{x}_\alpha^n - \Delta t \nabla V(\boldsymbol{x}_\alpha^n) + \sqrt{2k_B T \Delta t \boldsymbol{\zeta}_\alpha^n} \tag{5.31}$$

   where Δt is the time-step and $\boldsymbol{\zeta}_\alpha^n$ are independent standard Gaussian random variables. A reflecting boundary condition at the boundary of the Voronoi cell is defined by setting

$$\boldsymbol{x}_\alpha^{n+1} = \begin{cases} \boldsymbol{x}_\alpha^*, & \text{if } \boldsymbol{x}_\alpha^* \in B_\alpha^n \\ \boldsymbol{x}_\alpha^n, & \text{otherwise} \end{cases} \tag{5.32}$$

   where

$$B_\alpha^n = \{ \boldsymbol{x} \mid |\boldsymbol{x} - \boldsymbol{\psi}_\alpha^n| < |\boldsymbol{x} - \boldsymbol{\psi}_{\alpha'}^n|, \forall \alpha' \neq \alpha \} \tag{5.33}$$

2. The time-averaged position of the system is computed:

$$\bar{\boldsymbol{x}}_\alpha^n = \frac{1}{n} \sum_{i=0}^{n} \boldsymbol{x}_\alpha^i \tag{5.34}$$

3. Move each image toward the pertinent time-averaged position while keeping the string smooth by using

$$\boldsymbol{\psi}_\alpha^* = \boldsymbol{\psi}_\alpha^n - \Delta\eta(\boldsymbol{\psi}_\alpha^n - \vec{x}_\alpha^n) + \boldsymbol{r}_\alpha^* \tag{5.35}$$

where $\Delta\eta > 0$ is an adjustable parameter, and

$$\boldsymbol{r}_\alpha^* = \begin{cases} \chi(\boldsymbol{\psi}_{\alpha+1}^* + \boldsymbol{\psi}_{\alpha-1}^* - 2\boldsymbol{\psi}_\alpha^*), & \alpha = 1, ..., N-1 \\ 0, & \alpha = 0 \text{ or } N \end{cases} \tag{5.36}$$

where $\chi > 0$ is an adjustable parameter controlling the smoothing process.

4. Enforce equal distance between the images: interpolate a piecewise linear curve through $\{\boldsymbol{\psi}_\alpha^*\}$ and redistribute the images at equal distances along this curve to obtain $\{\boldsymbol{\psi}_\alpha^n\}$.

5. $$\begin{cases} \text{Back to step 1}, & \boldsymbol{x}_\alpha^{n+1} \in B_\alpha^{n+1} \\ \text{Set } \boldsymbol{x}_\alpha^{n+1} = \boldsymbol{\psi}_\alpha^{n+1}, & \text{Otherwise} \end{cases} \tag{5.37}$$

6. Continue until the convergence of $\{\boldsymbol{\psi}_\alpha^{n+1}\}$.

In plain words, the algorithm of the first step is as follows: constrained sampling at constant temperature is performed within each cell and the time averaged position associated with each cell is computed. Then, the time averaged positions are used to update the string and Voronoi cells, while satisfying a smoothing condition and enforcing equal distance between images. Iterating over this process leads to a converged string and its associated Voronoi cells. The Voronoi cells approximate the iso-committer surfaces and the images approximate the expected configuration within them. The quality of the approximation depends on the discretization error and the sampling error. We refer

the interested reader to Refs. [98, 120] for further details on the theoretical background of the method.

In the free energy calculation step, the algorithm uses the global balance equation,

$$\sum_{\substack{\alpha'=0 \\ \alpha' \neq \alpha}}^{N} \pi_{\alpha'} k_{\alpha'\alpha} = \sum_{\substack{\alpha'=0 \\ \alpha' \neq \alpha}}^{N} \pi_{\alpha} k_{\alpha\alpha'} \tag{5.38}$$

together with

$$\sum_{\alpha=0}^{N} \pi_{\alpha} = 1 \tag{5.39}$$

to find the equilibrium probabilities, π_α, of the cells $\alpha = 0, ..., N$. The transition matrix, $k_{\alpha\alpha'}$, can be computed from the formula

$$k_{\alpha\alpha'} = \frac{N^n_{\alpha\alpha'}}{n\Delta t} \tag{5.40}$$

by initiating a trajectory inside cell α and counting the number of times, $N^n_{\alpha\alpha'}$, the trajectory enters cell α' over n timesteps of Δt. When the trajectory leaves the cell where it was initiated, which is α in this case, it is brought back to the last configuration it had before leaving the cell. The estimate in Eq.5.40 converges as the length of the trajectory goes to infinity, i.e. $n \to \infty$. Further details can be found in [120].

5.4 Simulation Details

The atomistic simulations were conducted using a modified version of the LAMMPS package. As shown in Fig. 5.1, the simulation cell was bounded by $(\bar{1}2\bar{1})$, $(\bar{1}01)$, and (111) faces in the X, Y, and Z directions, respectively. A screw dislocation with the Burgers vector $\mathbf{b} = 1/2[111]$ was created at the center of the box by applying the elastic displacement solution [59] to a perfect BCC tungsten

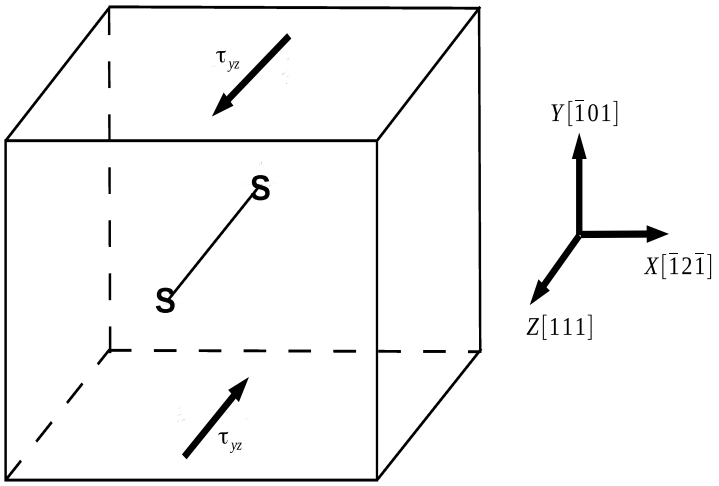

Figure 5.1: Simulation cell with a screw dislocation in the center and shear stresses applied on the top and bottom surfaces.

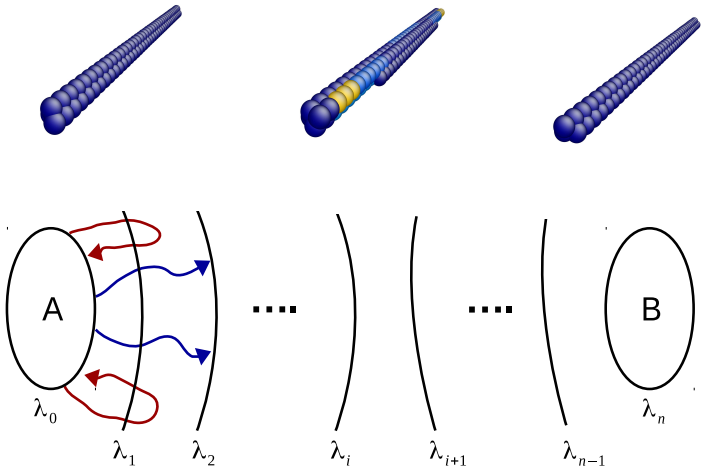

Figure 5.2: Bottom: A schematic picture of the interfaces and trajectories involved in TIS calculations. The interfaces are the boundaries of the cells defined by the FTS method. The blue and red trajectories have been described in Sec. 5.3.2. Top: Snapshots of the system as the dislocation glides on the (-1 0 1) plane at τ_{yz} = 600 MPa and T = 300K. The left image is the initial configuration. The middle image is the center of one of the intermmediate cells where a kink-pair has nucleated. The right image is the final configuration where the kink-pair has fully expanded and the dislocation has glided one Peierls valley. The images have been plotted by AtomEye [70].

lattice. Periodic boundary conditions were applied in the Z direction, while the other two boundary planes were traction free. The system was loaded by applying the shear forces

$$f_{top} = \frac{\tau_{yz} A_{xz}}{N_{top}}, \qquad f_{bottom} = -\frac{\tau_{yz} A_{xz}}{N_{bottom}} \tag{5.41}$$

on the atoms near the top and bottom Y surfaces. Direct MD simulations were conducted with NVT dynamics where a Langevin thermostat with a damping parameter of 1 ps was used.

For the given geometry (Fig. 5.1), there are 12 slip planes of the 110 and 112 types available for the dislocation. However, Stukowski et al. [113] and Cereceda et al. [24] have concluded that, for the potential used in this study, glide on any given plane takes place through sequential glides on 110 planes. For instance, glide on 112 plane is achieved by two glides on alternate 110 planes. They also show that the Peierls stress is significantly smaller on 110 planes with a twinning sense, which is a consequence of the well-understood twinning-antitwinning asymmetry of the BCC lattice [60, 41]. Therefore, for the stress state mentioned above, glide can only happen on two 110 planes: 1) the MRSS plane, $(\bar{1}01)$, and 2) the inclined twinning plane $(01\bar{1})$. In this manuscript, the glide on the MRSS plane is studied as an example for evaluating the performance of the methods discussed in Section. 5.3. The outcome of the study in terms of the utility of different approaches does not depend on the particular slip plane.

The activation potential energy used in the HTST rate predictions was computed with the LAMMPS implementation of the Nudged Elastic Band method [61]. The initial string for the NEB simulation was prepared using the procedure described in [23] and [99, 100]. The potential energy profile at

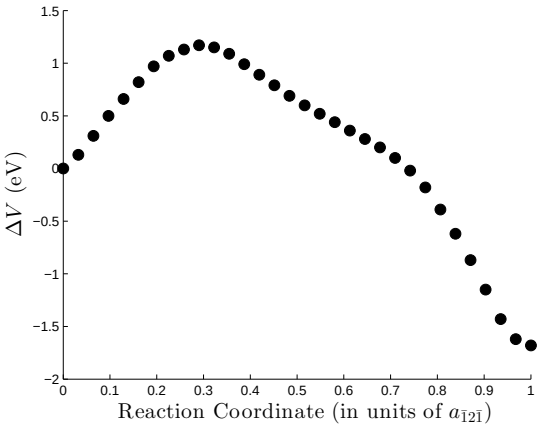

Figure 5.3: The potential energy barrier at τ_{yz} = 600MPa vs. the reaction coordinate in units of atomic spacing along $[\bar{1}2\bar{1}]$.

τ_{yz} = 600 MPa is shown in Fig. 5.3. The potential energy barrier in this case was ΔV = 1.17 eV.

The boundaries of the Voronoi cells defined in the first step of the FTS method were used as the TIS interfaces as well as the initial trajectory needed to initiate the shooting move algorithm. For the first step of the FTS algorithm to converge, changes had to be made to the algorithm, which will be discussed in Section. 5.5.1. The transition flux through the first interface, $\frac{\langle \phi_{\lambda_0,\lambda_1} \rangle}{\langle h_{\mathcal{A}} \rangle}$, was calculated using 50 independent direct MD simulations started with different seeds.

5.4.1 Cell Dimensions

The cell dimensions were $110 \times 55 \times 62$ nm. The dislocation length was selected based on four main considerations: 1) keeping the forces associated with the interaction of a kink with its periodic image small; 2) focusing on the smooth regime of kink-pair nucleation, i.e. kink-pairs nucleation on only one crystal-

lographic plane simultaneously; 3) convergence of kink-pair nucleation energy. As for kink-kink interaction energies, Hirth [75] use linear elasticity arguments to show that kink-kink interactions are negligible when the the kink pair separation is at least two times the kink width. Ventelon et al. [126] confirm this estimate through atomistic simulations on BCC Iron. Given that the kink-pair separation is about 8-14 $|\mathbf{b}|$ for the potential used here [23], the minimum dislocation length that ensures small interactions between a kink and its periodic image is 16-28 $|\mathbf{b}|$ = 43-76 nm. On the other hand, [77] and [48] argue that the dislocation length should be smaller than $L_y = 2w + d + X$ where w is the kink width, d is the kink separation and X is the kink free path. They show that $L_y \approx 80|\mathbf{b}|$ for Iron. Assuming that the same holds for tungsten, the maximum dislocation length that ensures kink-pair nucleation on only one plane is about 218 nm. Therefore, in order to have kink pairs on a single slip system and have a small kink-kink interaction, the dislocation length must be between 40nm and 215 nm. We performed NEB simulations for the dislocation lengths in this range and noticed that the kink-pair nucleation energy under zero stress converges at a dislocation length of about 110 nm and hence we selected that length for the simulations reported in this manuscript.

The other two dimensions were selected based on two main considerations: 1) convergence of the Peierls stress and the kink-pair nucleation energy; 2) computational cost. The Peierls stress was calculated for a dislocation length of 110 nm and a range of values of the other two dimensions by loading the cell in $\Delta\tau_{yz}$ = 50 MPa increments and minimizing the cell using the conjugate gradient method after each increment. The kink-pair nucleation energy was computed using the LAMMPS implementation of the Nudged Elastic Band method.

5.4.2 Empirical Potential

There are many interatomic potentials for tungsten. EAM potentials are the most studied and common potentials for tungsten due to their conceptual simplicity and computational efficiency. Among the EAM potentials, the most notable and studied ones for properties of screw dislocations are those of Marinica et al. [78] and Cereceda et al. [26]. A notable Modified EAM potential, whose performance in predicting properties of dislocations has been compared to other potentials extensively [26], is that of Juslin et al. [63]. There also have been tight-binding based bond order potentials (TB-BOD) [83, 89] that have been comprehensively studied for simulations of screw dislocations in tungsten [26].

Bonny et al. [16] compared the performance of 19 EAM potentials for predicting critical parameters of dislocations such as core structure, stacking fault energy, Peierls stress and potential, glide plane and etc. They concluded that the two EAM potentials called EAM3 and EAM4 in [78] are the most appropriate for modeling line defects as they provide the closest predictions of the mentioned properties to those of DFT. Cereceda et al. [26] compared the performance of EAM3 to that of the MEAM potential of Julstin et al. [63] and the TB-BOP potential of Park et al. [89] and concluded that EAM3 and the MEAM potential provide more accurate predictions of line defect properties compared to those of TB-BOP. They also showed that the performance of EAM3 and the MEAM potential are more or less on part up to 1500K, where EAM3 begins to predict a degenerated core-structure. Given that the temperatures considered in this manuscript are all below 1500K and the advantage of EAM potentials in terms of computational cost, we narrowed down the selection of the interatomic potential to EAM3 or EAM4.

EAM4 predicts the kink-pair nucleation energy, Peierls stress and the Gamma surface more accurately; whereas, EAM3 predicts the Peierls stress and the inter-row potential more accurately. There is also a difference between the glide plan predicted by the two potentials: EAM3 predicts the glide plane to be the MRSS $(\bar{1}01)$ at 0K, while EAM4 predicts the glide to take place on an inclined {110} plane. Although the study in [26] concludes EAM3 maintains a compact core structure under load at temperatures up to 1500K, the potential exhibited a degenerate core structure in some of finite temperature string simulations at room temperature. Therefore, EAM4 was selected for the studies conducted in this manuscript. Some of the developers of two potentials have also selected EAM4 over EAM3 in their extensive studies on dislocation motion in tungsten [23, 24, 93, 113].

5.5 Results and discussion

5.5.1 Finite Temperature String Method

As mentioned in Section. 5.4, the boundaries of the Voronoi cells generated by the first step of the FTS method are used as interfaces in the TIS simulations. Although the method has been successful in computing a reaction coordinate for many other problems including dislocation-obstacle interactions and dislocation nucleation [104, 87, 87], our efforts to generate a reasonable reaction coordinate for the kink-pair nucleation problem were frustrated. This was expected because the FTS algorithm is not ideal for problems with multiple reaction channels. For such problems, the method, in its original form, can at best

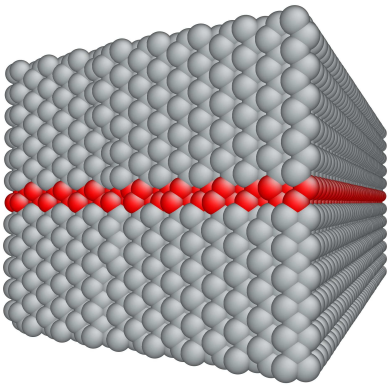

Figure 5.4: The set, Γ, of atoms on the planes immediately above and below the $(\bar{1}01)$ plane are shown in red. The norm $|\cdot|_\Gamma$ in Eq. 5.42 is defined for these atoms.

identify one of the reaction channels. To achieve that, it assumes that the channels are isolated and can be distinguished by the norms in items 1, 4 and 5 in Section. 5.3.3. In other words, the method assumes that all Voronoi cells are defined within one reaction channel and a transition from one channel to another is a rare event that can be detected by the norms that determine whether trajectories of the system are in the Voronoi cells where they were initiated or not. Therefore, the search for a reaction coordinate should be performed within only one reaction channel without being interrupted by sporadic switches to another channel. A trajectory switching to another channel should be quickly labeled as leaving its Voronoi cell and be immediately returned to its pertinent cell. In this problem, however, trajectories started in the Voronoi cells closer to the initial configuration can easily switch reaction channels without that being detected in the simulation. Therefore, the time averaged position of such trajectories may not be in either of the reaction channels, which leads to a string that does not contain the right uncorrelated kink-pair mechanism reported elsewhere in the

literature [23, 85].

This problem can be remedied by incorporating our knowledge about the displacement field of a screw dislocation into the norms defining the Voronoi cells in Eq. 5.33 such that the search for the reaction coordinate is performed in a subspace of the phase space that is the most relevant to the transition. The displacement field of a screw dislocation, $\boldsymbol{u} = [0, 0, \frac{|\boldsymbol{b}| \arctan(y/x)}{2\pi}]$, only affects the atomic coordinates in the z-direction. Further, the evolution of u_z as during the slip varies for different glide planes and this different is most significant for the atoms on the planes immediately above and below the slip plane. Therefore, the z-coordinates of those atoms are the most relevant subspace of the phase space during the transition and can be used to redefine the Voronoi cells of Eq. 5.33 as

$$B_\alpha^n = \{\, \boldsymbol{x} \mid |\boldsymbol{x}_z - \boldsymbol{\psi}_{z,\alpha}^n|_\Gamma < |\boldsymbol{x}_z - \boldsymbol{\psi}_{z,\alpha'}^n|_\Gamma, \forall \alpha' \neq \alpha \,\} \tag{5.42}$$

where $|\cdot|_\Gamma$ is the Euclidean norm applied on the set, Γ, of atoms on the planes immediately above and below the slip plane. The atoms in the set Γ are shown in red in Fig. 5.4. $\boldsymbol{x}_z$ are the z-coordinates in the phase space and $\boldsymbol{\psi}_{z,\alpha}^n$ is the vector of z-coordinates of the center of the cell α at time-step n. The equal arc-length parametrization in item 4 of Section. 5.3.3 is also performed in the subspace associated with the z-coordinates of atoms on Γ, i.e. the distance between images is measured based on $|\cdot|_\Gamma$ when interpolating a piecewise linear curve through $\{\boldsymbol{\psi}_\alpha^*\}$ and redistributing points at equal distance along this curve to obtain $\{\boldsymbol{\psi}_\alpha^{n+1}\}$.

This remedy leads to a reaction coordinate that has the right mechanism and a reasonable potential energy profile. For example, the top middle image in Fig. 5.2 shows the kink-pair observed in a finite temperature string at 300K and $\tau_{yz} = 600$MPa. The PE profile for that string is showin in Fig. 5.5. As expected

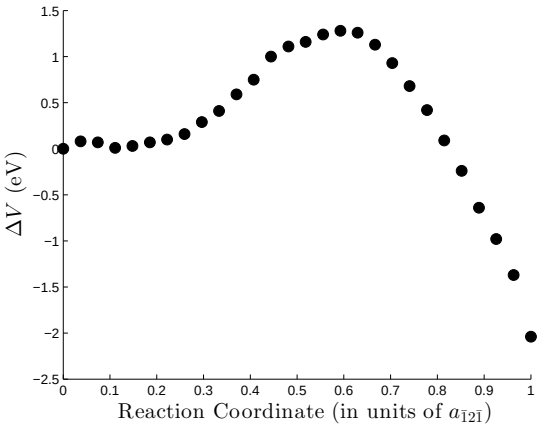

Figure 5.5: The potential energy profile along the finite temperature string at τ_{yz} = 600MPa and T = 300K vs. the reaction coordinate in units of atomic spacing along $[\bar{1}2\bar{1}]$.

the potential energies along the finite temperature string are slightly larger than those on the 0K string because of the stored thermal energy in the system. Also, the images associated with kink-pair nucleation and expansion have a higher potential energy compared to the initial and final configurations.

It should be noted that the string generated by the FTS method does not have to be an accurate reaction coordinate. For TIS simulations, it is sufficient that the string has the right temperature and captures the mechanism reasonably well. This will be discussed in more detail in next subsection.

5.5.2 Comparison of the methods

As mentioned before, the quantity of interest in this paper is the average time for a screw dislocation to glide on the $(\bar{1}01)$ by one atomic spacing, $a_0/\sqrt{2}$, i.e. $\bar{t} = k_{AB}^{-1}$. First, the predictions of the methods discussed in Section 5.3 are compared to benchmarks obtained from direct MD simulations at τ_{yz} = 600MPa and

Method	T = 333K	T = 353K
Direct MD	4.6	1.5
TIS	5.94	0.81
SHTST1	9.3×10^{12}	9.3×10^{11}
SHTST2	1×10^{11}	1×10^{10}

Table 5.1: The predictions of the methods described in Sec. 5.3 for the average time, $\bar{t}$ for a screw dislocation to glide by one atomic distance, $a_0/\sqrt{2}$, on the MRSS plane $(\bar{1}01)$. All the predictions are in nanoseconds and have been obtained at τ_{yz} = 600MPa.

two different temperatures, $T = 353K$ and $T = 333K$. The load is about the one third of the Peierls stress, $\tau_0 = 2000$MPa. The benchmark temperatures have been selected such that direct MD predictions can be obtained with reasonable computational efforts. The MD predictions were obtained as follows. First, 50 statistically independent samples were initiated at the appropriate temperature. The dislocation glides either on the MRSS plane or on the inclined 110 plane. Let us call the former type I samples and the latter type II samples. For type I samples, simulations are stopped as soon as the transition takes place and the waiting time is recorded. For type II samples, the entire time spent in those simulations is counted as waiting time. Therefore, the total waiting time is equal to the time spent in the type I samples before the transition plus the total simulation time in the type II samples. The average waiting time is then obtained by dividing the total waiting time by the number of type I samples. There were 15 and 14 samples of type I at 353K and 333K, respectively. Assuming $\bar{t}$ follows an exponential distribution [129], the 95% confidence intervals for the MD predictions are shown in Figure. 5.6, along with the TIS and MD predictions.

Harmonic Transition State Theory

Two SHTST predictions based on different estimates of the attempt frequency, ν_*, have been computed (Table 5.1). The two predictions overestimate the average time by 10-12 orders of magnitude. As discussed in Section 5.4, the activation potential energy used for the HTST predictions is $\Delta V = 1.17$ eV. SHTST1 is based on $\nu_* = 9.1 \times 10^{11}$ 1/s in Eq. 5.17, which has been computed by Stukowski et al. [113] for the potential used in this work and has been used extensively for predicting the kink-pair nucleation rate for tungsten, e.g. in an atomistically informed Crystal Plasticity model [24], Dislocation Dynamics simulations [93] and other meso-scale models [25]. SHTST2 is based on assuming that ν_* is equal to the Debye frequency of tungsten, 8×10^{13} 1/s. These significant discrepencies between the SHTST predictions and the benchmark MD predictions stem from three sources: 1) HTST neglects anharmonic vibrational entropy barrier, 2) HTST neglects conigurational entropy barrier, and 3) the errors associated with the approximation of the attempt frequency in Eq. 5.15 with the Debye frequency or Eq. 5.17. This will be discussed further in the next subsection.

Transition Interface Sampling

Given that the quantity of interest is the slip rate on the MRSS plane, a challenge with the TIS approach is how the algorithm should detect trajectories wherein the dislocation glides on the MRSS plane. In computing $N^{(A \to i \to i+1)}$ and $N^{(A \to i)}$ for Eq. 5.22, crossing an interface, λ_i, by a trajectory of the system, $\boldsymbol{x}(t)$, is defined as moving from the Voronoi cell B_i to B_{i+1} and $\boldsymbol{x}(t)$ is in a cell B_i when $\psi_i = \arg\min_{0 \le j \le N} |\boldsymbol{x}(t) - \boldsymbol{\psi}_j|$, i.e. $\boldsymbol{x}$ is closest to the cell center $\boldsymbol{\psi}_i$ than to any other cell centers. Our observation was that this norm did not accurately measure the

difference between the morphology and glide plane of the dislocation core in a trajectory to those in the cell centers. Therefore, the norm could not distinguish between trajectories with different slip planes and also could not detect transitions accurately. In many cases, the norm suggested that a kink-pair on the MRSS plane had nucleated while the dislocation in fact had glided on the inclined twinning plane.

To remedy this problem, a similar approach to that proposed for the FTS approach was used: the distance from $\boldsymbol{x}(t)$ to a cell center is measured by $|\boldsymbol{x}_z - \boldsymbol{\psi}_{z,i}|_\Gamma|$, i.e. the norm is only applied to the z-coordinates of the atoms on the planes immediately above and below the slip plane. Given that the evolution of u_z for atoms on Γ is characterized by the slip plane, trajectories that do not have the right mechanism are expected to be neglected during the shooting move algorithm as they are very unlikely fulfill all the conditions required to be accepted for a $p(\lambda_{i+1}|\lambda_i)$ ensemble.

As can be seen in Table 5.1, TIS based on the above norm and interfaces explained in Section 5.5.1 accurately predicts the average time relative to the MD benchmarks and performs significantly better than the two SHTST approaches discussed in Section 5.5.2. The reason is that TIS computes the rate using actual trajectories of the system and does not make any assumptions about material properties and the contributing factors to the entropy barrier. Further, unlike TST-based approaches, the method does not require an accurate reaction coordinate and complex free energy calculations, which can be very hard for problems with multiple reaction channels.

TIS simulations for the two benchmark problems were conducted based on the above norm and interfaces as explained in Section 5.5.1. The statical errors

were monitored both at the interface level, Eq. 5.28, and for the final prediction, Eq. 5.30. For all predictions in this manuscript, the number of samples for all interfaces, $N(A \rightarrow i)$, $i = 1, .., N-1$, was determined such that c_v^i, $i = 1, .., N-1$, were less than 5% and c_v was less than 10%. The probabilities $p(\lambda_{i+1}|\lambda_i)$ increase and levels off at one as the distance between the interfaces and the initial configuration increases, which is a sign that the transition has happened and hence the system commits to the final configuration with 100% probability.

To test the effectiveness of the above norm and the FTS interfaces in distinguishing between the two slip planes, 50 independent MD trajectories were generated at 333K and 353K and whether they would cross the last interface used in TIS simulations or not was monitored. All trajectories with the MRSS glide plane did cross the last interface and committed to the final configuration in less than 5 ps. None of the trajectories with the inclined glide plane crossed reached the last few cells used in the TIS simulations. This shows that such trajectories will not be part of the $p(\lambda_{i+1}|\lambda_i)$ ensembles of the last few cell where the transition happens and hence do not contribute to the flux to the final configuration.

5.5.3 The entropy barrier

There are three main trends in estimating the entropy barrier in studies concerning dislocation mechanics in the literature:

1. Different variants of HTST are commonly used in dislocation mobility laws in meso-scale models such as Crystal Plasticity [24, 85, 71], Kinetic Monte Carlo [113, 25, 22] and Dislocation Dynamics [93, 30]. Depending

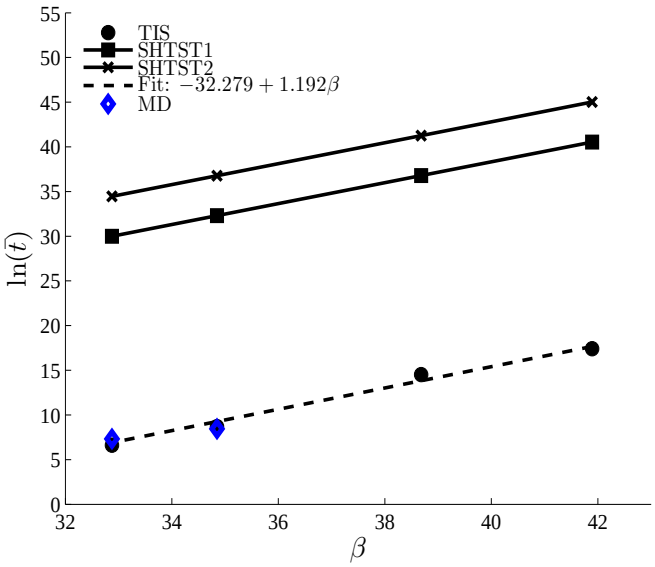

Figure 5.6: SHTS1, SHTST2 and TIS Arrhenius plots at τ_{yz} = 600MPa. The MD predictions at 333K and 353K are also shown. The average time, $\bar{t}$, is in picoseconds.

on the HTST variant used in such studies, the entropy is either approximated with the harmonic vibrational entropy barrier or it is assumed to very small or negligible altogether.

2. In some cases, on the other hand, the Meyer-Neldel (MN) rule is used to estimate the entropy barrier and then the estimate is used in the TST rate formula to describe the dislocation mobility law.

3. In the vast majority of such studies, the configurational entropy is assumed to be negligible.

In this section, the effectiveness of these practices for the problem of kink-pair nucleation in a BCC lattice is studied. The assumptions of these models are revisited and the circumstances in which those assumptions are likely to hold are discussed.

First, TIS is used to compute a benchmark for the entropy barrier to which predictions of the other methods are compared. To that end, the Arrhenius plot,i.e. $\ln(\bar{t})$ vs. $\beta = 1/k_B T$, is generated at a constant shear stress of τ_{yz} = 600MPa (Fig. 5.6). The TST rate formula, Eq. 5.10, can then be used to deduce the entropy barrier and the activation energy from the Arrhenius plot. Eq. 5.10 can be rewritten as

$$\ln(\bar{t}) = -\ln[\tilde{\nu}(\boldsymbol{\sigma}, T)] - \frac{\Delta S(\boldsymbol{\sigma}, T)}{k_B} + \beta \Delta U(\boldsymbol{\sigma}, T) \tag{5.43}$$

from which it is clear that the slope of the Arrhenius plot is $\Delta U(\boldsymbol{\sigma}, T)$ = 1.19 eV $\approx \Delta V$ and the y-intercept is $-(\ln[\tilde{\nu}(\boldsymbol{\sigma}, T)] + \frac{\Delta S(\boldsymbol{\sigma}, T)}{k_B})$. The entropy barrier can then be computed from Eq. 5.43 because the intercept is known and $\tilde{\nu}(\boldsymbol{\sigma}, T)$ can be estimated from direct MD simulations. We found $\tilde{\nu} \approx 1.3 \times 10^{11}\ s^{-1}$ at T = 300K and hence the entropy barrier is $\Delta S(\boldsymbol{\sigma}, T) = 34 k_B$. Our simulations showed that $\tilde{\nu}$ is temperature independent in the temperature range considered here. The linearity of the Arrhenius plot implies that $\Delta U(\boldsymbol{\sigma}, T)$ and the intercept $-(\ln[\tilde{\nu}(\boldsymbol{\sigma}, T)] + \frac{\Delta S(\boldsymbol{\sigma}, T)}{k_B})$ are also temperature independent. Therefore, the entropy barrier is likely to be temperature independent over the examined temperature range.

The Harmonic Approximation

The entropy barrier is significantly larger than the 1-3 k_B range typically assumed or computed for solids [103, 102, 101, 54, 104] and hence explains the inaccuracy in the HTST based approaches. The total entropy barrier can be divided into a vibrational component, ΔS_v, and a configurational component, ΔS_c:

$$\Delta S = \Delta S_v + \Delta S_c \tag{5.44}$$

HTST neglects the configurational entropy barrier and computes ΔS_v based on the theory of small vibrations, which neglects temperature effects on vibrational modes and frequencies. SHTST based on the natural frequency along the reaction coordinate neglects both ΔS_v and ΔS_c. Other estimates of ν_* also either neglect ΔS_v or lead to small values for the vibrational entropy. That is why HTST based approaches are not suitable for problems with large anharmonic effects such as thermal softening [104, 87, 86, 102] or problems with large configurational entropy barriers.

The MN rule

The MN rule, a.k.a. the thermodynamics compensation law, is likely the most common approach for estimating the entropy barrier in the material mechanics community [104, 102, 30, 93] and it is also used with various names in other fields. The MN rule expresses ΔS as $\Delta S = \Delta U/T_m$, where T_m is the melting temperature. The method is an empirical relation and its interpretation is subject to a lot debate in other fields [17, 6]. However, it is used in dislocation mechanics with the justification discussed in the following paragraphs.

The energy, ΔU, associated with many dislocation concepts, such line energy, obstacle bypassing and etc, scales with the shear modulus, μ [3], i.e. $\Delta U(\boldsymbol{\sigma}) = f(\boldsymbol{\sigma})\mu$ where f is a function of stress. Configurational entropies of most dislocation processes are assumed to be negligible [3, 29]. However, thermal softening of $\mu(T)$ is a manifestation of S_v because $\mu(T)$ is inversely related to thermal expansion and the quasi-harmonic lattice dynamics theory shows that thermal expansion leads to lower phonon frequencies and hence higher vibrational entropy [3, 47, 40]. Therefore, many continuum thermoelastic models,

e.g. [38], take the vibrational entropy into account by assuming that the temperature dependence of the free energy stems from that of the shear modulus, i.e. $\Delta F(\boldsymbol{\sigma}, T) = f(\boldsymbol{\sigma})\mu(T)$. The (vibrational) entropy is then computed from

$$\begin{aligned}\Delta S(\boldsymbol{\sigma}, T) &= -\frac{\partial \Delta F(\boldsymbol{\sigma}, T)}{\partial T} \\ &= -f(\boldsymbol{\sigma})\frac{\partial \mu(T)}{\partial T} \\ &= -f(\boldsymbol{\sigma})\frac{\mu(0)}{\mu(0)}\frac{\partial \mu(T)}{\partial T} \\ &= -\Delta U(\boldsymbol{\sigma})\frac{\partial \ln \mu(T)}{\partial T}\end{aligned} \tag{5.45}$$

From the lattice vibration theory [3, 114], it can be shown that $\frac{\partial \ln \mu(T)}{\partial T}$ vanishes at 0K and decreases with temperature until it plateaus around the Debye Temperature, T_D. This means that the shear modulus linearly decreases with temperature at $T \geq T_D$, which is also supported by experimental evidence for various metals and alloys. It is common to assume that μ vanishes at the melting point, ΔS in Eq. 5.45 can be expressed as

$$\Delta S(\boldsymbol{\sigma}) = \frac{\Delta U(\boldsymbol{\sigma})}{T_m} \tag{5.46}$$

which is the entropy barrier expression proposed by the MN rule. It should be noted that the shear modulus of most metals and alloys does not vanish at temperatures slightly below the melting temperature [55, 43]. At those temperatures, the shear modulus typically decreases by 50% with respect to its value at 0K. Yet, the MN rule has been shown to be accurate for different dislocation processes, likely because the activation energy for those processes happens to approach to zero near the melting temperature.

Given the assumptions behind the theoretical justification of the MN rule, the method is most suitable for problems where the entropy barrier is known to be of vibrational nature and stem from anharmonic effects of thermal expansion. Atomistic simulations have shown that the MN rule has been particularly

successful for dislocation processes such as dislocation nucleation [103, 131] and obstacle bypassing by cutting/shearing [104]. The assumptions of the MN rule are justified for those problems because the configurational entropy is expected to be small [29, 3] and the shear modulus is known to linearly decrease with temperature for many FCC metals.

Taking the melting point reported for the tungsten potential [93], T_m = 3695K, the entropy barrier estimated by Eq. 5.46 is 3.7 k_B, which is significantly smaller than the benchmark value of $34k_B$. The large discrepancy between the MN rule prediction and the benchmark value stems from two sources of error. First, Eq. 5.46 only accounts for thermal softening and hence neglects configurational entropy barriers, which, as will be discussed in the next subsection, are relevant in this problem. Second, the MN rule assumes that the critical shear stress, $\hat{\tau}$, is temperature independent. Experimental studies [4] and atomistic simulations [131] have showed that this is not the case for other metals and alloys. It should be noted that the two sources of error can be related as the configurational entropy barrier decreases the activation free energy and hence CSS with temperature. A model that addresses the second source of error has been proposed in the previous Chapter.

Configurational Entropy Barrier

The configurational entropy of mildly curved dislocations is known to be negligible [29, 3]. However, it is also known that the equilibrium configuration of a dislocation at finite temperatures is not straight because kink-pairs and other irregularities such as jogs decrease the free energy by increasing the configurational entropy. Hirth and Lothe [57] have expressed the equilibrium concentra-

tion of kink-pairs per unit length of a dislocation as

$$c = \frac{1}{|\boldsymbol{b}|^2} e^{-\frac{\Delta H_{kp}}{k_B T}} \tag{5.47}$$

by expressing the configurational entropy barrier as

$$\Delta S_c = -2Lk_B \sqrt{c}(\ln(\sqrt{c}|\boldsymbol{b}|) - 1) \tag{5.48}$$

and then minimizing the free energy with respect to c. L is the dislocation segment length and ΔH_{kp} is the formation enthalpy energy of a kink-pair.

Argon has proposed the following model for ΔH_{kp} in Sections 4.5-4.6.2 of [3]:

$$\Delta H_{kp} = \frac{T}{T_0} \frac{\pi}{4} \sqrt{\hat{\tau}\mu |\boldsymbol{b}|^3 h^3} \tag{5.49}$$

where T_0 is the temperature at which lattice resistance vanishes, $\hat{\tau}$ is the effective athermal resistance and h is the kink height, i.e. one atomic distance along $[\bar{1}2\bar{1}]$. The model holds at both low and high stress regimes of kink-pair nucleation. At low stresses, the activation free energy is derived based on the assumption that the kink-kink interaction is just counteracted by the applied stress. At high stresses, on the other hand, the activation free energy is derived based on assuming a parabolic lattice resistance potential. Having a free energy expression, Argon expresses the activation enthalpy via the Van't Hoff's equation for temperature jump experiments, i.e. $\Delta H_{kp} = k_B T^2 \left(\frac{\partial \ln \dot{\gamma}}{\partial T} - \frac{\partial \ln \dot{\gamma}_0}{\partial T} \right)$. Interestingly, the expression for the activation enthalpy happens to be the same for both regimes but $\hat{\tau}$ and h are different for the two regimes. We refer the interested reader to Sections 4.5-4.6.2 of [3] for further details.

T_0 can be taken to be the melting temperature. Our MD simulations showed a value of 1100MPa for $\hat{\tau}$ at 300K which leads to $\Delta S_c \approx 36 k_B$. Note that although this estimate of the configurational entropy is for a dislocation in equilibrium,

it is still relevant for the problem examined in this study. That is because the dislocation is straight in the initial configuration used for both TIS and MD predictions. In other words, the rate measured in this study is for the glide of a straight dislocation through kink-pair nucleation and this process is helped by the tendency of the initial configuration to increase the configurational entropy through kink-pair nucleation.

Discussion

The sum of the vibrational entropy estimated by the MN rule, Eq. 5.46, and the configurational entropy from Eq. 5.48 is about $40k_B$, which is a good estimate of the benchmark $\Delta S = 34\ k_B$. While the MN rule has been very successful in estimating the entropy barrier for dislocation processes in FCC metals, it fails to provide an accurate prediction for this case. The main reason is that the entropy barrier of kink-pair nucleation has a large configurational component, which is neglected by the MN rule. Moreover, the relatively stronger bonds of tungsten lead to lower temperature dependence of the vibrational frequencies and hence a lower vibrational entropy compared to FCC metals. That is why the MN rule prediction of the entropy barrier is quite close to the range of harmonic vibrational entropies typically observed for solids.

Variants of HTST fail to provide accurate predictions of the rate. The reason is that the harmonic approximation neglects both major components of the entropy barrier in this problem: 1) thermal softening, 2) configurational entropy. In fact, most HTST variants neglect the entropy barrier altogether. However, the error in such approaches can be easily corrected by approximating the entropy barrier by the sum of Eq. 5.46 and Eq. 5.48.

While a free energy profile along the reaction coordinate is required to clearly demonstrate these concepts, computing the free energy profile is a daunting task for problems such as this, and to the best of our knowledge has not been done before. Even a powerful a tool such as FTS will typically fail to provide an accurate free energy profile for problems with simpler energy landscapes such as dislocation-precipitate interactions because some of the method's assumptions are not fulfilled. We refer the interested reader to [104] for more detail. Avoiding such complexities in free energy calculations is one of the key features of direct rate theories, such as TIS, because they can compute the rate using actual trajectories of the system, without requiring a free energy profile or an accurate reaction coordinate.

5.6 Summary and Conclusions

The glide rate of a screw dislocation through kink-pair nucleation was studied using atomistic simulations and rate theories. The performance of different variants of HTST, as the most common rate theory in the literature, and TIS, as a modern rate theory, was examined for a benchmark problem. It was observed that TIS accurately predicts the rate for the benchmark problems, while the HTST models provided grossly inaccurate predictions. To shed light on the accuracy of the harmonic approximation as well as the temperature dependence of the rate, the entropy barrier of the problem was studied. To that end, first, TIS was used to compute a benchmark estimate of the entropy barrier. The benchmark estimate was significantly larger than the range typically observed for harmonic vibrational entropy barriers observed for solids, which showed the inaccuracy of the HTST models stemmed from neglecting anharmonic effects.

Next, the performance of the MN rule, as the most common entropy prediction approach in the material mechanics community, was examined. It was shown that the prediction of the MN rule was significantly smaller than the benchmark entropy barrier. To shed light on this issue, the theoretical justification of the MN rule for dislocation problems and the associated assumptions were revisited. It was discussed that the MN rule is based on the assumption that the temperature dependence of the free energy stems from that of the shear modulus. Given that the temperature dependence of the shear modulus is associated with the softening of bonds and the vibrational modes, the MN rule only accounts for the vibrational entropy and neglects the configurational component. This led us to study the configurational component of the entropy barrier for this problem.

To study the configurational entropy, the simple model of Hirth and Lothe for the equilibrium concentration of kink-pairs was revisited. The model is based on the idea that straight dislocations have a tendency to nucleate kink-pairs to reduce their free energy as a result of increasing the configurational entropy. It was shown that the sum of the vibrational entropy barrier predicted by the MN rule and the configurational entropy barrier predicted by the Hirth and Lothe model is fairly close to the benchmark entropy. Therefore, the combination of the Hirth and Lothe model, the MN rule and the TST rate expression provide a simple and accurate rate theory that can be used in dislocation mobility laws of meso-scale models.

Finally, this paper encourages similar studies that evaluate the utility of different methods for different applications. The importance of this point will be more clear if one notes the nuances between the above conclusions and those

for the other two problems studied in this thesis and others studies on dislocation nucleation. HTST was shown to be inaccurate for all of these problems ([86, 104] and Chapter 5). TST was found to be accurate for dislocation nucleation [86] but difficult to apply for dislocation-obstacle interactions [104] and kink-pair nucleation. TIS was found to be accurate for dislocation-precipitate interactions [104] but it had to be modified for the kink-pair nucleation problem and it was only accurate for dislocation-solute interactions in the case of jerky dislocation motion. PPTIS, on the other hand, has been designed for problems with diffusive barrier and hence was only accurate in the case of smooth dislocation motion through a field of solutes. FTS can provide a reaction coordinate for all these cases except for the kink-pair nucleation problem, for which it had to be modified. The MN rule provides a precise prediction for dislocation-precipitate interactions but it has to be complemented with more accurate models for dislocation-solute interactions and kink-pair nucleation. Given these nuances, there is no silver bullet approach and hence a rate theory must be tested against direct MD simulations before being used for an application.

Acknowledgements

The authors acknowledge Dr. Bernard Ross for financially supporting this research through the Cornell Ross-Tetelman Fellowship.

BIBLIOGRAPHY

[1] Rosalind J Allen, Chantal Valeriani, and Pieter Rein ten Wolde. Forward flux sampling for rare event simulations. *Journal of Physics: Condensed Matter*, 21(46):463102, 2009.

[2] F Apostol and Y Mishin. Interatomic potential for the al-cu system. *Physical Review B*, 83(5):054116, 2011.

[3] Ali S Argon. *Strengthening mechanisms in crystal plasticity*. Number 4. Oxford University Press Oxford, 2008.

[4] Hiroshi Asada, Ryo Horiuchi, Hideo Yoshinaga, and Seishi Nakamoto. Flow stress in al–mg alloy single crystals. *Transactions of the Japan Institute of Metals*, 8(3):159–166, 1967.

[5] KL Baker and DH Warner. Extended timescale atomistic modeling of crack tip behavior in aluminum. *Modelling and Simulation in Materials Science and Engineering*, 20(6):065005, 2012.

[6] BEC Banks, V Damjanovic, and CA Vernon. The so-called thermodynamic compensation law and thermal death. 1972.

[7] Jodi E Basner and Steven D Schwartz. How enzyme dynamics helps catalyze a reaction in atomic detail: a transition path sampling study. *Journal of the American Chemical Society*, 127(40):13822–13831, 2005.

[8] CH Bennett. Algorithms for chemical computations. In *ACS symposium Series*, volume 46, page 63, 1977.

[9] Luca Bertini and Markus Reiher. *Atomistic approaches in modern biology: from quantum chemistry to molecular simulations*, volume 268. Springer, 2007.

[10] Robert B Best. Atomistic molecular simulations of protein folding. *Current opinion in structural biology*, 22(1):52–61, 2012.

[11] P. G. Bolhuis. Rare events via multiple reaction channels sampled by path replica exchange. *Journal of Chemical Physics*, 129:114108, May 2008.

[12] Peter G Bolhuis. Transition-path sampling of β-hairpin folding. *Proceedings of the National Academy of Sciences*, 100(21):12129–12134, 2003.

[13] Peter G. Bolhuis, David Chandler, Christoph Dellago, and Phillip L. Geissler. Transition path sampling: Throwing ropes over rough mountain passes, in the dark. *Annual Review of Physical Chemistry*, 53(1):291–318, 2002. PMID: 11972010.

[14] Peter G Bolhuis, C Dellago, B Dünweg, G Gompper, T Ihle, DM Kroll, AJC Ladd, and RG Winkler. Advanced computer simulation approaches for soft matter sciences iii. *Self*, 221, 2009.

[15] Peter G Bolhuis and Christoph Dellago. 3 trajectory-based rare event simulations. *Reviews in Computational Chemistry*, 27:111, 2011.

[16] Giovanni Bonny, Dmitry Terentyev, Alexander Bakaev, Petr Grigorev, and Dimitri Van Neck. Many-body central force potentials for tungsten. *Modelling and Simulation in Materials Science and Engineering*, 22(5):053001, 2014.

[17] MR Boon. Thermodynamic compensation rule. 1973.

[18] Ernesto E Borrero and Fernando A Escobedo. Folding kinetics of a lattice protein via a forward flux sampling approach. *The Journal of chemical physics*, 125(16):164904, 2006.

[19] Ernesto E Borrero and Fernando A Escobedo. Optimizing the sampling and staging for simulations of rare events via forward flux sampling schemes. *The Journal of chemical physics*, 129(2):024115, 2008.

[20] Ernesto E Borrero, Marcus Weinwurm, and Christoph Dellago. Optimizing transition interface sampling simulations. *The Journal of chemical physics*, 134(24):244118, 2011.

[21] JG Byrne, ME Fine, and A Kelly. Precipitate hardening in an aluminium-copper alloy. *Philosophical Magazine*, 6(69):1119–1145, 1961.

[22] Wei Cai, Vasily V Bulatov, Sidney Yip, and Ali S Argon. Kinetic monte carlo modeling of dislocation motion in bcc metals. *Materials Science and Engineering: A*, 309:270–273, 2001.

[23] D Cereceda and J Marian. Nudged elastic band simulations of kink pairs in tungsten. Technical report, Lawrence Livermore National Laboratory (LLNL), Livermore, CA (United States), 2015.

[24] David Cereceda, Martin Diehl, Franz Roters, Dierk Raabe, J Manuel Perlado, and Jaime Marian. Unraveling the temperature dependence of the yield strength in single-crystal tungsten using atomistically-informed crystal plasticity calculations. *International Journal of Plasticity*, 78:242–265, 2016.

[25] David Cereceda, Martin Diehl, Franz Roters, Pratheek Shanthraj, Dierk Raabe, José Manuel Perlado, and Jaime Marian. Linking atomistic, kinetic monte carlo and crystal plasticity simulations of single-crystal tungsten strength. *GAMM-Mitteilungen*, 38(2):213–227, 2015.

[26] David Cereceda, Alexander Stukowski, MR Gilbert, Sylvain Queyreau, Lisa Ventelon, Mihai-Cosmin Marinica, JM Perlado, and Jaime Marian. Assessment of interatomic potentials for atomistic analysis of static and dynamic properties of screw dislocations in w. *Journal of Physics: Condensed Matter*, 25(8):085702, 2013.

[27] David Chandler. Statistical mechanics of isomerization dynamics in liquids and the transition state approximation. *The Journal of Chemical Physics*, 68(6):2959–2970, 1978.

[28] Julien Chaussidon, Marc Fivel, and David Rodney. The glide of screw dislocations in bcc fe: atomistic static and dynamic simulations. *Acta materialia*, 54(13):3407–3416, 2006.

[29] AH Cottrell and DL Dexter. Dislocations and plastic flow in crystals. *American Journal of Physics*, 22(4):242–243, 1954.

[30] Yinan Cui, Giacomo Po, and Nasr Ghoniem. Temperature insensitivity of the flow stress in body-centered cubic micropillar crystals. *Acta Materialia*, 108:128–137, 2016.

[31] William A Curtin, David L Olmsted, and Louis G Hector. A predictive mechanism for dynamic strain ageing in aluminium–magnesium alloys. *Nature materials*, 5(11):875–880, 2006.

[32] Christoph Dellago and Peter G Bolhuis. Transition path sampling and other advanced simulation techniques for rare events. In *Advanced computer simulation approaches for soft matter sciences III*, pages 167–233. Springer, 2009.

[33] Christoph Dellago, Peter G Bolhuis, and David Chandler. Efficient transi-

tion path sampling: Application to lennard-jones cluster rearrangements. *The Journal of chemical physics*, 108(22):9236–9245, 1998.

[34] Christoph Dellago, Peter G Bolhuis, and David Chandler. On the calculation of reaction rate constants in the transition path ensemble. *The Journal of chemical physics*, 110(14):6617–6625, 1999.

[35] Christoph Dellago, Peter G Bolhuis, Félix S Csajka, and David Chandler. Transition path sampling and the calculation of rate constants. *The Journal of chemical physics*, 108(5):1964–1977, 1998.

[36] TJ Delph, P Cao, HS Park, and JA Zimmerman. A harmonic transition state theory model for defect initiation in crystals. *Modelling and Simulation in Materials Science and Engineering*, 21(2):025010, 2013.

[37] Lucile Dezerald, David Rodney, Emmanuel Clouet, Lisa Ventelon, and François Willaime. Plastic anisotropy and dislocation trajectory in bcc metals. *Nature communications*, 7, 2016.

[38] RJ DiMelfi, WD Nix, DM Barnett, JH Holbrook, and GM Pound. An analysis of the entropy of thermally activated dislocation motion based on the theory of thermoelasticity. *physica status solidi (b)*, 75(2):573–582, 1976.

[39] John E Dorn and Stanley Rajnak. Nucleation of kink pairs and the peierls mechanism of plastic deformation. *Trans. Aime*, 230(8):1052–1064, 1964.

[40] Martin T Dove. *Introduction to lattice dynamics*, volume 4. Cambridge university press, 1993.

[41] M and-S Duesbery and V Vitek. Plastic anisotropy in bcc transition metals. *Acta Materialia*, 46(5):1481–1492, 1998.

[42] Furio Ercolessi and James B Adams. Interatomic potentials from first-principles calculations. In *MRS Proceedings*, volume 291, page 31. Cambridge Univ Press, 1992.

[43] Lassner Erik and Schubert Wolf-Dieter. Tungsten: properties, chemistry, technology of the element, alloys, and chemical compounds, 1999.

[44] Fernando A Escobedo, Ernesto E Borrero, and Juan C Araque. Transition path sampling and forward flux sampling. applications to biological systems. *Journal of Physics: Condensed Matter*, 21(33):333101, 2009.

[45] Henry Eyring. The activated complex in chemical reactions. *The Journal of Chemical Physics*, 3(2):107–115, 1935.

[46] Daan Frenkel and Berend Smit. *Understanding molecular simulation: from algorithms to applications*, volume 1. Academic press, 2001.

[47] Brent Fultz. Vibrational thermodynamics of materials. *Progress in Materials Science*, 55(4):247–352, 2010.

[48] MR Gilbert, S Queyreau, and J Marian. Stress and temperature dependence of screw dislocation mobility in α-fe by molecular dynamics. *Physical Review B*, 84(17):174103, 2011.

[49] Samuel Glasstone, Keith James Laidler, and Henry Eyring. *The theory of rate processes: the kinetics of chemical reactions, viscosity, diffusion and electrochemical phenomena*. McGraw-Hill Book Company, Incorporated, 1941.

[50] Peter A Gordon, T Neeraj, and Michael J Luton. Atomistic simulation of dislocation nucleation barriers from cracktips in α-fe. *Modelling and Simulation in Materials Science and Engineering*, 16(4):045006, 2008.

[51] R Gröger, AG Bailey, and V Vitek. Multiscale modeling of plastic deformation of molybdenum and tungsten: I. atomistic studies of the core structure and glide of 1/2¡ 111¿ screw dislocations at 0k. *Acta Materialia*, 56(19):5401–5411, 2008.

[52] R Gröger, V Racherla, JL Bassani, and V Vitek. Multiscale modeling of plastic deformation of molybdenum and tungsten: Ii. yield criterion for single crystals based on atomistic studies of glide of 1/2¡ 111¿ screw dislocations. *Acta Materialia*, 56(19):5412–5425, 2008.

[53] R Gröger and V Vitek. Multiscale modeling of plastic deformation of molybdenum and tungsten. iii. effects of temperature and plastic strain rate. *Acta Materialia*, 56(19):5426–5439, 2008.

[54] Shotaro Hara and Ju Li. Adaptive strain-boost hyperdynamics simulations of stress-driven atomic processes. *Physical Review B*, 82(18):184114, 2010.

[55] RFS Hearmon. Temperature dependence of the elastic constants of aluminium. *Solid State Communications*, 37(11):915–918, 1981.

[56] P. Hirel, J. Godet, S. Brochard, L. Pizzagalli, and P. Beauchamp. Determination of activation parameters for dislocation formation from a surface in fcc metals by atomistic simulations. *Phys. Rev. B*, 78:064109, Aug 2008.

[57] John P Hirth and Jens Lothe. Theory of dislocations. 1982.

[58] Juro Horiuti. On the statistical mechanical treatment of the absolute rate of chemical reaction. *Bulletin of the Chemical Society of Japan*, 13(1):210–216, 1938.

[59] Derek Hull and David J Bacon. *Introduction to dislocations*. Butterworth-Heinemann, 2001.

[60] K Ito and V Vitek. Atomistic study of non-schmid effects in the plastic yielding of bcc metals. *Philosophical Magazine A*, 81(5):1387–1407, 2001.

[61] Hannes Jonsson, Greg Mills, and Karsten W Jacobsen. Nudged elastic band method for finding minimum energy paths of transitions. 1998.

[62] Jarek Juraszek, Jocelyne Vreede, and Peter G Bolhuis. Transition path sampling of protein conformational changes. *Chemical Physics*, 396:30–44, 2012.

[63] N Juslin, P Erhart, P Träskelin, J Nord, Krister OE Henriksson, K Nordlund, E Salonen, and K Albe. Analytical interatomic potential for modeling nonequilibrium processes in the w–c–h system. *Journal of applied physics*, 98(12):123520, 2005.

[64] Woo Kyun Kim and Ellad B Tadmor. Entropically stabilized dislocations. *Physical review letters*, 112(10):105501, 2014.

[65] WF Kocks. Thermodynamics and kinetics of slip. *Progr. Mater. Sci.*, 19:291, 1975.

[66] LP Kubin and Yu Estrin. Evolution of dislocation densities and the critical conditions for the portevin-le chatelier effect. *Acta metallurgica et materialia*, 38(5):697–708, 1990.

[67] Rea Labusch. A statistical theory of solid solution hardening. *physica status solidi (b)*, 41(2):659–669, 1970.

[68] Keith J. Laidler and M. Christine King. Development of transition-state theory. *The Journal of Physical Chemistry*, 87(15):2657–2664, 1983.

[69] GPM Leyson and WA Curtin. Thermally-activated flow in nominally binary al–mg alloys. *Scripta Materialia*, 111:85–88, 2016.

[70] Ju Li. Atomeye: an efficient atomistic configuration viewer. *Modelling and Simulation in Materials Science and Engineering*, 11(2):173, 2003.

[71] Hojun Lim, Corbett C Battaile, Jay D Carroll, Brad L Boyce, and Christopher R Weinberger. A physically based model of temperature and strain rate dependent yield in bcc metals: Implementation into crystal plasticity. *Journal of the Mechanics and Physics of Solids*, 74:80–96, 2015.

[72] Karin Lin and DC Chrzan. Kinetic monte carlo simulation of dislocation dynamics. *Physical Review B*, 60(6):3799, 1999.

[73] Xiang-Yang Liu, James B Adams, Furio Ercolessi, and John A Moriarty. Eam potential for magnesium from quantum mechanical forces. *Modelling and Simulation in Materials Science and Engineering*, 4(3):293, 1996.

[74] Xiang-Yang Liu, PP Ohotnicky, JB Adams, C Lane Rohrer, and RW Hyland. Anisotropic surface segregation in al- mg alloys. *Surface science*, 373(2):357–370, 1997.

[75] J Lothe and JP Hirth. Dislocation dynamics at low temperatures. *Physical Review*, 115(3):543, 1959.

[76] Luca Maragliano, Eric Vanden-Eijnden, and Benoît Roux. Free energy and kinetics of conformational transitions from voronoi tessellated milestoning with restraining potentials. *Journal of chemical theory and computation*, 5(10):2589–2594, 2009.

[77] Jaime Marian, Wei Cai, and Vasily V Bulatov. Dynamic transitions from smooth to rough to twinning in dislocation motion. *Nature Materials*, 3(3):158–163, 2004.

[78] Mihai-Cosmin Marinica, Lisa Ventelon, MR Gilbert, L Proville, SL Dudarev, J Marian, G Bencteux, and F Willaime. Interatomic potentials for modelling radiation defects and dislocations in tungsten. *Journal of Physics: Condensed Matter*, 25(39):395502, 2013.

[79] Glyn Meyrick and Gordon W Powell. Phase transformations in metals and alloys. *Annual Review of Materials Science*, 3(1):327–362, 1973.

[80] Daniele Moroni. *Efficient sampling of rare event pathways*. PhD thesis, Ph. D. thesis, Universiteit van Amsterdam, 2005.

[81] Daniele Moroni, Peter G Bolhuis, and Titus S van Erp. Rate constants for diffusive processes by partial path sampling. *The Journal of chemical physics*, 120(9):4055–4065, 2004.

[82] Daniele Moroni, Titus S van Erp, and Peter G Bolhuis. Investigating rare events by transition interface sampling. *Physica A: Statistical Mechanics and its Applications*, 340(1):395–401, 2004.

[83] Matous Mrovec, Roman Gröger, Aimee Gotway Bailey, Duc Nguyen-Manh, Christian Elsässer, and Vaclav Vitek. Bond-order potential for simulations of extended defects in tungsten. *Physical Review B*, 75(10):104119, 2007.

[84] Shinji Muraishi, Nobutaka Niwa, Atsushi Maekawa, Shinji Kumai, and Akikazu Sato. Strengthening of al-cu single crystals by stress-oriented guinier-preston zones. *Philosophical Magazine A*, 82(14):2755–2771, 2002.

[85] Sankar Narayanan, David L McDowell, and Ting Zhu. Crystal plasticity model for bcc iron atomistically informed by kinetics of correlated kinkpair nucleation on screw dislocation. *Journal of the Mechanics and Physics of Solids*, 65:54–68, 2014.

[86] LD Nguyen, KL Baker, and DH Warner. Atomistic predictions of dislocation nucleation with transition state theory. *Physical Review B*, 84(2):024118, 2011.

[87] LD Nguyen and DH Warner. Improbability of void growth in aluminum via dislocation nucleation under typical laboratory conditions. *Physical review letters*, 108(3):035501, 2012.

[88] David L Olmsted, Louis G Hector, and WA Curtin. Molecular dynamics study of solute strengthening in al/mg alloys. *Journal of the Mechanics and Physics of Solids*, 54(8):1763–1788, 2006.

[89] Hyoungki Park, Michael R Fellinger, Thomas J Lenosky, William W Tipton, Dallas R Trinkle, Sven P Rudin, Christopher Woodward, John W

Wilkins, and Richard G Hennig. Ab initio based empirical potential used to study the mechanical properties of molybdenum. *Physical Review B*, 85(21):214121, 2012.

[90] Baron Peters and Bernhardt L Trout. Obtaining reaction coordinates by likelihood maximization. *The Journal of chemical physics*, 125(5):054108, 2006.

[91] R.C. Picu, Renge Li, and Zhijie Xu. Strain rate sensitivity of thermally activated dislocation motion across fields of obstacles of different kind. *Materials Science and Engineering: A*, 502(12):164 – 171, 2009.

[92] RC Picu, G Vincze, F Ozturk, JJ Gracio, F Barlat, and AM Maniatty. Strain rate sensitivity of the commercial aluminum alloy aa5182-o. *Materials Science and Engineering: A*, 390(1):334–343, 2005.

[93] Giacomo Po, Yinan Cui, David Rivera, David Cereceda, Tom D Swinburne, Jaime Marian, and Nasr Ghoniem. A phenomenological dislocation mobility law for bcc metals. *Acta Materialia*, 119:123–135, 2016.

[94] Laurent Proville, David Rodney, and Mihai-Cosmin Marinica. Quantum effect on thermally activated glide of dislocations. *Nature materials*, 11(10):845–849, 2012.

[95] Tiezheng Qian, Weiqing Ren, and Ping Sheng. Current dissipation in thin superconducting wires: A numerical evaluation using the string method. *Physical Review B*, 72(1):014512, 2005.

[96] Weiqing Ren and Eric Vanden-Eijnden. Finite temperature string method for the study of rare events. *The Journal of Physical Chemistry B*, 109(14):6688–6693, 2005.

[97] Weiqing Ren, Eric Vanden-Eijnden, et al. Transition pathways in complex systems: Reaction coordinates, isocommittor surfaces, and transition tubes. *Chemical Physics Letters*, 413(1):242–247, 2005.

[98] Weiqing Ren, Eric Vanden-Eijnden, Paul Maragakis, E Weinan, et al. Transition pathways in complex systems: Application of the finite-temperature string method to the alanine dipeptide. *The Journal of chemical physics*, 123(13):134109, 2005.

[99] David Rodney. Activation enthalpy for kink-pair nucleation on disloca-

tions: Comparison between static and dynamic atomic-scale simulations. *Phys. Rev. B*, 76:144108, Oct 2007.

[100] David Rodney and Laurent Proville. Stress-dependent peierls potential: Influence on kink-pair activation. *Physical Review B*, 79(9):094108, 2009.

[101] Seunghwa Ryu. *The Validity of Classical Nucleation Theory and Its Application to Dislocation Nucleation*. Stanford University, 2011.

[102] Seunghwa Ryu, Keonwook Kang, and Wei Cai. Entropic effect on the rate of dislocation nucleation. *Proceedings of the National Academy of Sciences*, 108(13):5174–5178, 2011.

[103] Seunghwa Ryu, Keonwook Kang, and Wei Cai. Predicting the dislocation nucleation rate as a function of temperature and stress. *Journal of Materials Research*, 26(18):2335–2354, 2011.

[104] S Saroukhani, LD Nguyen, KWK Leung, CV Singh, and DH Warner. Harnessing atomistic simulations to predict the rate at which dislocations overcome obstacles. *Journal of the Mechanics and Physics of Solids*, 90:203–214, 2016.

[105] G Schoeck. The activation energy of dislocation movement. *physica status solidi (b)*, 8(2):499–507, 1965.

[106] Steven D Schwartz and Vern L Schramm. Enzymatic transition states and dynamic motion in barrier crossing. *Nature chemical biology*, 5(8):551–558, 2009.

[107] Chandra Veer Singh and Derek H Warner. An atomistic-based hierarchical multiscale examination of age hardening in an al-cu alloy. *Metallurgical and Materials Transactions A*, 44(6):2625–2644, 2013.

[108] CV Singh, AJ Mateos, and DH Warner. Atomistic simulations of dislocation–precipitate interactions emphasize importance of cross-slip. *Scripta Materialia*, 64(5):398–401, 2011.

[109] CV Singh and DH Warner. Mechanisms of guinier–preston zone hardening in the athermal limit. *Acta Materialia*, 58(17):5797–5805, 2010.

[110] MA Soare and WA Curtin. Single-mechanism rate theory for dynamic strain aging in fcc metals. *Acta Materialia*, 56(15):4091–4101, 2008.

[111] MA Soare and WA Curtin. Solute strengthening of both mobile and forest dislocations: The origin of dynamic strain aging in fcc metals. *Acta Materialia*, 56(15):4046–4061, 2008.

[112] BRITISH STANDARD. Eurocode 9design of aluminium structures. 2007.

[113] Alexander Stukowski, David Cereceda, Thomas D Swinburne, and Jaime Marian. Thermally-activated non-schmid glide of screw dislocations in w using atomistically-informed kinetic monte carlo simulations. *International Journal of Plasticity*, 65:108–130, 2015.

[114] Honghong Su, Xufei Fang, Xue Feng, and Bo Yan. Temperature-dependent modulus of metals based on lattice vibration theory. *Journal of Applied Mechanics*, 81(4):041017, 2014.

[115] T Surek, MJ Luton, and JJ Jonas. Dislocation glide controlled by linear elastic obstacles: a thermodynamic analysis. *Philosophical Magazine*, 27(2):425–440, 1973.

[116] BA Szajewski and WA Curtin. Analysis of spurious image forces in atomistic simulations of dislocations. *Modelling and Simulation in Materials Science and Engineering*, 23(2):025008, 2015.

[117] Donald G Truhlar and Bruce C Garrett. Variational transition-state theory. *Accounts of Chemical Research*, 13(12):440–448, 1980.

[118] T. S. van Erp. Reaction rate calculation by parallel path swapping. *Phys. Rev. Lett.*, 98:268301, May 2007.

[119] T. S. van Erp, D. Moroni, and P. G. Bolhuis. A novel path sampling method for the calculation of rate constants. *The Journal of Physical Chemistry*, 118:7762–7774, May 2003.

[120] T. S. van Erp and M. Venturoli. Revisiting the finite temeperature string method for the calculation of reaction tubes and free energies. *The Journal of Chemical Physics*, 130:194103, May 2009.

[121] Titus S Van Erp and Peter G Bolhuis. Elaborating transition interface sampling methods. *Journal of computational Physics*, 205(1):157–181, 2005.

[122] Eric Vanden-Eijnden and Fabio A Tal. Transition state theory: Variational

formulation, dynamical corrections, and error estimates. *The Journal of chemical physics*, 123(18):184103, 2005.

[123] Eric Vanden-Eijnden and Maddalena Venturoli. Markovian milestoning with voronoi tessellations. *The Journal of chemical physics*, 130(19):194101, 2009.

[124] Eric Vanden-Eijnden and Maddalena Venturoli. Revisiting the finite temperature string method for the calculation of reaction tubes and free energies. *The Journal of chemical physics*, 130(19):194103, 2009.

[125] Eric Vanden-Eijnden, Maddalena Venturoli, Giovanni Ciccotti, and Ron Elber. On the assumptions underlying milestoning. *The Journal of chemical physics*, 129(17):174102, 2008.

[126] Lisa Ventelon, F Willaime, and P Leyronnas. Atomistic simulation of single kinks of screw dislocations in α-fe. *Journal of Nuclear Materials*, 386:26–29, 2009.

[127] George H Vineyard. Frequency factors and isotope effects in solid state rate processes. *Journal of Physics and Chemistry of Solids*, 3(1):121–127, 1957.

[128] Arthur Voter. Hyperdynamics: Accelerated molecular dynamics of infrequent events. *Phys. Rev. Lett.*, 78:3908–3911, May 1997.

[129] Arthur Voter. Parallel replica method for dynamics of infrequent events. *Phys. Rev. B*, 57:R13985–R13988, Jun 1998.

[130] Arthur F Voter. A method for accelerating the molecular dynamics simulation of infrequent events. *The Journal of chemical physics*, 106(11):4665–4677, 1997.

[131] DH Warner and WA Curtin. Origins and implications of temperature-dependent activation energy barriers for dislocation nucleation in face-centered cubic metals. *Acta Materialia*, 57(14):4267–4277, 2009.

[132] DH Warner, WA Curtin, and S Qu. Rate dependence of crack-tip processes predicts twinning trends in fcc metals. *Nature materials*, 6(11):876–881, 2007.

[133] E Weinan, Weiqing Ren, and Eric Vanden-Eijnden. String method for the study of rare events. *Physical Review B*, 66(5):052301, 2002.

[134] E Weinan, Weiqing Ren, and Eric Vanden-Eijnden. Simplified and improved string method for computing the minimum energy paths in barrier-crossing events. *The Journal of Chemical Physics*, 126(16):164103, 2007.

[135] Jérôme Weiss and David Marsan. Three-dimensional mapping of dislocation avalanches: clustering and space/time coupling. *Science*, 299(5603):89–92, 2003.

[136] Jérôme Weiss, Thiebaud Richeton, François Louchet, Frantisek Chmelik, Patrick Dobron, Denis Entemeyer, Mikhail Lebyodkin, Tatiana Lebedkina, Claude Fressengeas, and Russell J McDonald. Evidence for universal intermittent crystal plasticity from acoustic emission and high-resolution extensometry experiments. *Physical Review B*, 76(22):224110, 2007.

[137] E Wigner. The transition state method. *Trans. Faraday Soc.*, 34:29–41, 1938.

[138] Zhijie Xu and R. Picu. Thermally activated motion of dislocations in fields of obstacles: The effect of obstacle distribution. *Phys. Rev. B*, 76:094112, Sep 2007.

[139] VI Yamakov, DH Warner, RJ Zamora, E Saether, WA Curtin, and EH Glaessgen. Investigation of crack tip dislocation emission in aluminum using multiscale molecular dynamics simulation and continuum modeling. *Journal of the Mechanics and Physics of Solids*, 65:35–53, 2014.

[140] Ting Zhu, Ju Li, and Sidney Yip. Atomistic study of dislocation loop emission from a crack tip. *Phys. Rev. Lett.*, 93:025503, Jul 2004.